

# FINAL REPORT

## Environmentally Benign Repair of Composites Using High Temperature Cyanate Ester Nanocomposites

SERDP Project Wp-1580

OCTOBER 2010

Michael R. Kessler, Ph.D.  
Mufit Akinc, Ph.D.  
**Ames Laboratory**

*This document has been cleared for public release*



REPORT DOCUMENTATION PAGE				Form Approved OMB No. 0704-0188	
Public reporting burden for this collection of information is estimated to average 1 hour per response, including the time for reviewing instructions, searching existing data sources, gathering and maintaining the data needed, and completing and reviewing this collection of information. Send comments regarding this burden estimate or any other aspect of this collection of information, including suggestions for reducing this burden to Department of Defense, Washington Headquarters Services, Directorate for Information Operations and Reports (0704-0188), 1215 Jefferson Davis Highway, Suite 1204, Arlington, VA 22202-4302. Respondents should be aware that notwithstanding any other provision of law, no person shall be subject to any penalty for failing to comply with a collection of information if it does not display a currently valid OMB control number. <b>PLEASE DO NOT RETURN YOUR FORM TO THE ABOVE ADDRESS.</b>					
1. REPORT DATE (DD-MM-YYYY) 01-10-2010		2. REPORT TYPE Final Report		3. DATES COVERED (From - To) Feb. 2007 to Sept. 2010	
4. TITLE AND SUBTITLE  Environmentally Benign Repair of Composites Using High Temperature Cyanate Ester Nanocomposites				5a. CONTRACT NUMBER	
				5b. GRANT NUMBER	
				5c. PROGRAM ELEMENT NUMBER	
6. AUTHOR(S)  Michael R. Kessler & Mufit Akinç				5d. PROJECT NUMBER WP-1580	
				5e. TASK NUMBER	
				5f. WORK UNIT NUMBER	
7. PERFORMING ORGANIZATION NAME(S) AND ADDRESS(ES)  AmesLaboratory, Iowa State University 2220 Hoover Hall, Materials Science and Engineering Ames, IA 50011-2300				8. PERFORMING ORGANIZATION REPORT NUMBER  IS-5196	
9. SPONSORING / MONITORING AGENCY NAME(S) AND ADDRESS(ES)  Strateic Environmental Research and Development Program, SERDP 901 North Stuart Street, Suite 303 Arlington, VA 22203				10. SPONSOR/MONITOR'S ACRONYM(S)  SERDP	
				11. SPONSOR/MONITOR'S REPORT NUMBER(S)	
12. DISTRIBUTION / AVAILABILITY STATEMENT					
13. SUPPLEMENTARY NOTES					
14. ABSTRACT  Interlaminar fracture, or delamination, is a common failure mode which often occurs in composites as a result of low energy impact or manufacturing defects. In this project, we have designed and evaluated a new class of environmentally benign, low viscosity cyanate ester resins reinforced with nanosize reinforcement for the repair of advanced composites. The use temperature limit for this repair technology is high because of the polymer's high glass transition temperature of greater than 500°F (260°C) and onset of decomposition above 750°F (400°C). The prepolymer also has near infinite room temperature stability, facilitating reduced wastes due to spoilage compared to traditional thermosets. In demonstrations of the technology on bismaleimide (BMI)/carbon composite panels, the strength of damaged composites that were repaired with the technology through a resin injection process exceeded the strength of the virgin undamaged composite material. This technology will reduce the environmental hazards associated with current composite repairs and open up new repair opportunities specifically for high temperature composites, such as BMI matrix composites.					
15. SUBJECT TERMS Composite Materials, Damage Repair, Bismaelimide, Cyanate Ester					
16. SECURITY CLASSIFICATION OF:			17. LIMITATION OF ABSTRACT  UU	18. NUMBER OF PAGES  85	19a. NAME OF RESPONSIBLE PERSON Michael R. Kessler
a. REPORT	b. ABSTRACT	c. THIS PAGE			19b. TELEPHONE NUMBER (include area code) 515-294-3101

# Table of Contents

Table of Contents .....	i
List of Figures .....	iii
List of Tables .....	vi
List of Acronyms and Symbols.....	vii
Acknowledgements .....	ix
Abstract .....	1
Objectives .....	1
Background .....	1
Composite Repair.....	1
High-temperature Resins .....	3
Nanocomposites for Rheological and Adhesive Enhancement .....	4
Materials and Methods.....	6
Cure Kinetics (neat BECy)-Experimental .....	6
Comparison to Benchmark Materials-Experimental .....	7
Cure Kinetics (nanoparticle filled BECy)-Experimental.....	9
Functionalization of alumina nanoparticles-Experimental .....	9
Rheology of nanoparticle/cyanate ester suspensions-Experimental .....	10
Thermal-mechanical properties of cured nanocomposites -Experimental.....	12
Adhesive strength and repair system evaluation –Experimental .....	13
Results and Discussion .....	18
Cure Kinetic Modeling-Results .....	18
Comparison to Benchmark Materials –Results.....	28
Adhesive strength and repair system evaluation-Results.....	29
Cure Kinetics (nanoparticle filled BECy)- Results.....	48
Functionalization of alumina nanoparticles- Results.....	50
Rheology of nanoparticle/cyanate ester suspensions-Results.....	53
Thermal-mechanical properties of cured nanocomposites -Results .....	60
Repair system evaluation with nano filled BECy .....	70
Conclusions and Implications for Future Research/Implementation.....	71
Literature Cited .....	74
Appendix A: List of Technical Publications.....	78
Peer Reviewed Journals .....	78

Conference/Symposium Proceedings/ Published Technical Abstracts.....	78
--	----

## List of Figures

Figure 1. Scarf repair method [7].....	2
Figure 2. Resin-injection repair method [7].....	2
Figure 3. Cured $T_g$ vs. 0.15 Pa.s Temp. ....	3
Figure 4. Cyanate ester chemical structures and cyclotrimerization reaction scheme. ....	4
Figure 5. Example of thixotropy caused by the incorporation of nanosized particles: viscosity is low when shear force is applied (front), and higher when at rest (rear) (Photo courtesy of Cabot Corp.) .....	5
Figure 6. Chemical structures of matrix resins used in the benchmark systems. ....	7
Figure 7. Viscosity of EPON/BGE solution versus weight percent BGE added.....	8
Figure 8. Viscosity of CA/BGE solution versus weight percent BGE added.....	8
Figure 9. Chemical structure of silanes and functionalization reaction scheme.....	10
Figure 10. TEM micrographs of fumed silica aggregates, a) 12 nm, b) 40 nm. ....	11
Figure 11. Experimental setup for DCB testing a) Fracture specimen loaded in crack opening mode to grow delamination b) Close-up image of the crack tip during propagation used to determine crack length. ....	15
Figure 12. The apparatus used for the injection repair process. (1) is the composite sample after delamination (2) The well from where the vacuum was pulled and the resin injected (3) quad-ring (4) Polycarbonate base (5) Silicon rubber (6) Kapton tape (7) vacuum sealant tape.....	16
Figure 13. Hole plate shear method by which delaminations were introduced into composite plates. ....	17
Figure 14. The TGA curves (at 20 °C/min) of catalyzed BECy under nitrogen and air. ....	18
Figure 15. Typical DSC curves for partially cured BECy samples that were cured at 180 °C for various times. ....	19
Figure 16. Residual reaction heat $\Delta H_r$ and $T_g$ of BECy samples isothermally cured at 180 °C for various times. ....	19
Figure 17. Plot of conversion vs. time for isothermal cures of BECy at different curing temperature. ....	20
Figure 18. Autocatalytic modeling of isothermal cure data.....	21
Figure 19. Arrhenius plot obtained by autocatalytic model.....	22
Figure 20. $T_g$ vs. conversion plot with DiBenedetto equation fitting. ....	23
Figure 21. Dynamic scanning method: experimental DSC curves of uncured BECy(symbols) and model fittings (solid lines). ....	24
Figure 22. Plots based on Kissinger's approaches. ....	25
Figure 23. Isoconversional analysis: Ozawa approach. ....	26
Figure 24. Isoconversional analysis: Friedman plot. ....	27
Figure 25. Results of lap shear experiments on an aluminum substrate at room temperature and elevated temperature. ....	30
Figure 26. Results of lap shear experiments on a BMI/carbon fiber substrate at room temperature and elevated temperature. ....	30
Figure 27. TGA of post-cured BMI illustrating the moisture desorption of 2 wt.-% at 250 °C... 31	
Figure 28. Microscopic images of fracture surface of BMI-cf lap shear specimens demonstrating the various modes of failure under different testing conditions for a) BECy-undried and b) BECy-dry c) BECy-200 d) Epoxy-RT e) Epoxy-200.....	32

Figure 29. SBSB stress of BECy and Epoxy repaired specimens tested both at room temperature and 200 °C. (a) Stress-strain behavior of BMI-cf SBSB specimen (b) Average SBSB strength of investigated specimens.....	33
Figure 30. (a) Typical load-displacement curve of a DCB specimen for BMI pristine sample. (b) DCB load-displacement curve for pristine specimen compared with the DCB specimens repaired with BECy and Epoxy. ....	35
Figure 31. R-curves for composites repaired with BECy and Epoxy resins tested at room temperature and 200 °C.....	37
Figure 32. SEM images of DCB fracture surfaces a) Pristine sample, b) Wet repaired sample, c) Dry repaired sample d) Epoxy repaired sample at 200 °C.....	38
Figure 33. Influence of temperature on the contact angle of BECy on BMI-cf substrate. ....	39
Figure 34. C-scan images of BMI-cf HPS specimens repaired at room temperature and 120 °C	40
Figure 35. C-scan images of specimens used for florescent dye Penetration (FDP) Test. ....	41
Figure 36. Microscopic images of the transverse cross section view of BMI-cf specimens with traces of florescent dye Penetration (FDP) taken under ultraviolet. ....	41
Figure 37. Microscopic images of the transverse cross section view of BMI-cf specimens with traces of cracks on the left side and the skeleton of the crack lengths on the right side.....	42
Figure 38. Total crack length measured from the cross section surface of pristine, delaminated and repaired specimens. ....	43
Figure 39. HPS testing on pristine, delaminated and repaired specimen.....	44
Figure 40. Maximum peak load of pristine, delaminated and repaired specimens in HPS testing. ....	44
Figure 41. Experimental setup for CAI test with double-edge-notch (DENT) specimen. ....	45
Figure 42. CAI stress of pristine, delaminated and repaired specimens. ....	46
Figure 43. C-scan images of 10 in x 10 in BMI-cf PMC panel, a) Pristine, b) Delaminated, c) Repaired .....	47
Figure 44. HPS test on the 254 x 254 mm BMI-cf PMC panel.....	47
Figure 45. Dynamic scanning of BECy contained nanoparticles: (a) dynamic scanning curves of BECy/alumina nanoparticles, 10wt.% sample; (b) Comparison of BECy/alumina nanoparticles sample with different loadings at 1°C/min; (c) the effects of alumina and silica nanoparticles on the cure of BECy, at same loading; (d) at same heating rate. ....	49
Figure 46. TG results of functionalized alulmina nanoparticles.....	51
Figure 47. FT-IR spectrum of APS functionalized alumina nanoparticles.....	51
Figure 48. Dispersion test in methylene chloride, THF, methanol. ....	52
Figure 49. Viscosity vs. shear rate for 12 nm fumed silica suspensions (0.1 to 100 s <sup>-1</sup> ). ....	53
Figure 50 Viscosity vs. shear rate for 40 nm fumed silica suspensions (0.1 to 100 s <sup>-1</sup> ). ....	53
Figure 51. Viscosity vs. shear rate for 12 nm suspensions (log-normal, < 10 s <sup>-1</sup> ). ....	54
Figure 52. Viscosity vs. shear rate for 40 nm suspensions (log-normal, < 10 s <sup>-1</sup> ). ....	54
Figure 53. Fumed silica (5 phr, 2.58 vol%) in polymerized BECy matrix, a) 12 nm silica, b) 40 nm silica. ....	56
Figure 54. Thixotropy recovery as a function of time (0.1 Pa, data taken at 2 min intervals). ....	57
Figure 55. Rheological properties of 12 nm fumed silica nanocomposites during cure at 130 °C. ....	58
Figure 56. Rheological properties of 40 nm fumed silica nanocomposites during cure at 130 °C. ....	59

Figure 57. Rheokinetics comparison for 2 phr (1.05 vol%) 12 and 40 nm fumed silica nanocomposites.....	59
Figure 58. Storage modulus ( $E'$ ) versus temperature for 12 nm fumed silica nanocomposites....	60
Figure 59. Storage modulus ( $E'$ ) versus temperature for 40 nm fumed silica nanocomposites....	61
Figure 60. Storage modulus at 30 °C vs. volume fraction of fumed silica.....	62
Figure 61. Rubbery storage modulus (@ $T_g + 30$ °C) vs. volume fraction.....	64
Figure 62. TEM micrographs of nanocomposites at a loading of 2.6 vol%, a) 12 nm silica, b) 40 nm silica.....	65
Figure 63. Tan delta (damping) as a function of temperature near the glass transition (12 nm silica).....	65
Figure 64. Tan delta (damping) as a function of temperature near the glass transition (40 nm silica).....	66
Figure 65. $T_g$ versus volume fraction of fumed silica, with horizontal lines indicating the glass transition temperature of the neat BECy resin. Error bars are on same order as symbol size. ....	68
Figure 66. $T_g$ versus volume fraction of fumed silica, with horizontal lines indicating the glass transition temperature of the neat BECy resin (Samples prepared in humid conditions were eliminated from this graph).....	68
Figure 67. $T_g$ vs. post-cure temperature for 1 phr samples.....	69
Figure 68. Lap shear testing of nano resins on BMI-cf PMC and Aluminum substrate.....	70
Figure 69. HPS testing of nano resin repaired specimens in comparison with pristine and BECy repair specimens.....	71

## List of Tables

Table 1. Kinetic parameters at different isothermal cure temperature.	22
Table 2. Parameters for the DiBenedetto equation relating $T_g$ and conversion.	23
Table 3. Cure kinetic parameters calculated from Kissinger and Flynn-Wall-Ozawa approach.	28
Table 4 Comparison of Volatile Content from TGA.	29
Table 5 Details of samples loading.	48
Table 6 Activation energy estimated from the separated peaks	49
Table 7. Interphase thickness estimation from damping behavior for 12 and 40 nm silica nanocomposites.	67



## List of Acronyms and Symbols

APS	(3-Aminopropyl) triethoxysilane
ASTM	American Society for Testing and Materials
BECy	Bisphenol-E cyanate ester
BMI	Bismaleimide
CAI	Compression after impact test
C <sub>f</sub>	Carbon fiber
C <sub>p</sub>	Heat capacity
DCB	Double cantilever beam
DSC	Differential scanning calorimetry
da/dt	Conversion rate
E <sub>a</sub>	Activation energy
E <sub>f</sub>	Modulus of filler
E <sub>m</sub>	Modulus of matrix
FDP	Florescence dye penetration
FT-IR	Fourier transform infrared spectroscopy
G'	Storage shear modulus
G''	Loss shear modulus
G <sub>IC</sub>	Strain energy release rate
G <sub>PS</sub>	(3-Glycidyloxypropyl)trimethoxysilane
HAP	Hazardous air pollutant
HPS	Hole plate shear
hrs	Hours
Hz	Hertz
K	Temperature dependent reaction rate
LN2	Liquid nitrogen
min	Minutes
MWNT	Multu walled carbon nanotube
NDT	Non-distractive testing
Pa	Pascal
PMC	Polymer matrix composites
PPh	Parts per hundred
R	Real gas constant
RH	Relative humidity
RT	Room temperature
SEM	Scanning electron microscopy
S <sub>TI</sub>	Shear thinning index
T	Temperature
T <sub>c</sub>	Cure temperature
TEM	Transmission electron microscopy
T <sub>g</sub>	Glass transition
TGA	Thermogravimetric analysis
UV	Ultraviolet
VOC	Volatile organic compound
Vol %	volume percent

WLF	Williams-Landel-Ferry
Wt %	weight percent
$\alpha$	Chemical conversion
$\delta$	Crack opening displacement
$\Delta H_r$	residual reaction heat
$\Delta H_t$	Total reaction heat
$\eta$	Viscosity
$\lambda$	Structure dependent constant
$\tau$	Shear stress in 3 point bend test
$\varphi_f$	Volume fraction of filler
$\varphi_m$	Volume fraction of matrix
$\psi$	Interactions between polymer and matrix

## **Acknowledgements**

We specially thank our co-workers Dr. Mahendra Thunga, Dr. Xia Sheng, Dr. Will Goertzen, Wilber Lio, Jonathan Henson, Katherine Ament, Kelsey Larson and Thilina Weerasekera for their sincere research efforts in pursuing our proposed goals and successful completion of the project.

We would like to thank Dr. Vinay Dayal from the Department of Aerospace Engineering, Iowa State University for his help with compression after impact (CAI) tests, Dan Barnard from the Center for Nondestructive Evaluation, Iowa State University for his guidance in ultrasonic C-Scan imaging and providing access to their laboratory facilities and Warren Straszheim of the Materials Analysis and Research Laboratory, at Iowa State University for helping with SEM investigations.

We gratefully acknowledge the financial support from the Strategic Environmental Research and Development Program (SERDP), Project Number WP-1580.

## Abstract

Interlaminar fracture, or delamination, is a common failure mode which often occurs in composites as a result of low energy impact or manufacturing defects. In this project, we have designed and evaluated a new class of environmentally benign, low viscosity cyanate ester resins reinforced with nanosize reinforcement for the repair of advanced composites. The use temperature limit for this repair technology is high because of the polymer's high glass transition temperature of greater than 500°F (260°C) and onset of decomposition above 750°F (400°C). The prepolymer also has near infinite room temperature stability, facilitating reduced wastes due to spoilage compared to traditional thermosets. In demonstrations of the technology on bismaleimide (BMI)/carbon composite panels, the strength of damaged composites that were repaired with the technology through a resin injection process exceeded the strength of the virgin undamaged composite material. This technology will reduce the environmental hazards associated with current composite repairs and open up new repair opportunities specifically for high temperature composites, such as BMI matrix composites.

## Objectives

*The objective of this project was to design and evaluate a new class of environmentally benign, low viscosity resins reinforced with nanosize alumina and silica particles for the repair of advanced composites.* These repair systems were rheologically engineered for optimum crack filling and stability for repairment to withstand high loadings, environmental extremes and wide service temperatures. The repair resins and associated repair techniques developed through this research program were designed to meet the following technical objectives:

- Repair system will have a low viscosity to completely fill the damage zone
- No or minimal volatile organic compounds, hazardous air pollutants, and hazardous waste will be generated by the repair process
- A high cured glass transition temperature will be obtained (over 260°C) in the adhesive to allow the repair of composites for extreme temperature environments
- Repair system will be mechanically superior to current repair processes.

## Background

### ***Composite Repair***

Polymer matrix composites (PMCs) are especially susceptible to matrix microcracking when subjected to repeated thermomechanical loading. Often these matrix microcracks coalesce and lead to other damage modes including fiber/matrix debonding and ply delamination [1 - 5]. Long term degradation of material properties results and much effort is directed towards reliable damage prediction and property degradation models. Low velocity impact from events such as a tool drop or a glancing bird strike on an aircraft is another common cause of delamination damage in fiber reinforced PMCs. In many cases, this damage is difficult to detect and even more difficult to repair because it often forms deep within the structure. Once this damage has developed, the integrity of the structure is greatly compromised.

Currently composite parts that have been damaged in service are first inspected manually to determine the extent of damage. For critical parts this inspection may include such

nondestructive testing (NDT) techniques as ultrasonics, infrared thermography, X-ray tomography, and computerized vibro thermography [6]. If the damage is too severe the structural component is replaced entirely. For less extensive damage, repairs are attempted.

If localized delamination has occurred, one common repair method is the use of a reinforcing patch bonded or bolted to the composite structure. However, such repairs are not aerodynamically smooth and may cause design problems by locally changing the stiffness and weight of the structure. In

some cases, “taper sanded” or “scarfed” repairs are performed by carefully removing material from the laminate at a shallow angle with a high-speed grinder followed by filling the removed area with repair plies (as shown in Figure 1). While these aerodynamic repairs are very effective at achieving the similar stiffness and weight of the undamaged part, the recovery of strength for these common “scarfed” repairs are often significantly lower than the virgin laminate because of the inherent destruction of the outer plies during the grinding process. There are also several environmental and safety concerns with “scarfed” repairs due to the machining and/or grinding of the composite components which results in hazardous fiber dust. Likewise, these repairs require extensive solvent cleaning prior to bonding (to clean in and around the ground area and to remove paint around the damage zone), resulting in significant VOCs and hazardous waste material. Numerous studies regarding these and other composite repair methods have been published [7 - 15].

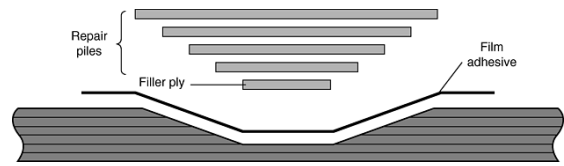


**Figure 1. Scarf repair method [7]**

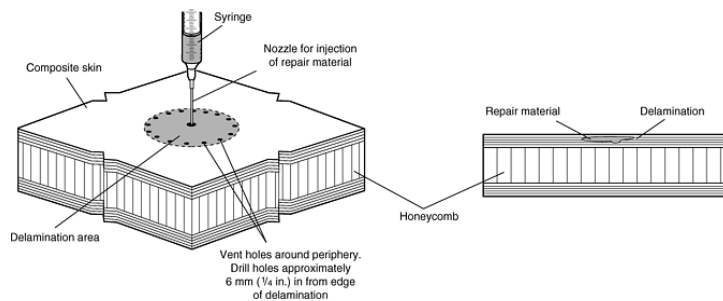


**Figure 2. Resin-injection repair method [7]**

Alternately, the delamination may be repaired by injecting resin via an access hole into the failed area (as shown in Figure 2). This eliminates the need to remove the outer, undamaged plies and can result in higher repair strengths than the “scarfed” repair if the adhesive strength of the injected resin is adequately high. However, the viscosity of the injected resin is an issue

and, in some cases, has to be diluted with volatile organic solvents to achieve the required low viscosity. Once the resin solution is infiltrated, the resin is cured (typically at elevated temperatures). Additionally, these low viscosity resins usually have lower glass transition temperatures than the matrices in many military grade composites, limiting their application for elevated temperature service. Finally, the resins and adhesives used for repair often have short shelf lives and can generate hazardous air pollutants and hazardous waste during the repair process.

There are several requirements for an ideal resin system for the resin-injection repair method:

- *Low viscosity.* Once injected into the damage zone the repair resin must be drawn into the furthest reaches of the crack. Often, the larger, multi-level delaminations are separated by matrix microcracks that only a very low viscosity resin can infiltrate.
- *Stability in the Damage Zone.* Once in the crack plane, the repair system should react to bond the crack surfaces closed. The resin system should not evaporate or diffuse away from the cracks. Thus a shear thinning fluid is ideal, so that it will act as a low viscosity

liquid at high shear, and a stable, more viscous liquid at very low shear to remain in the damage zone until polymerization is complete.

- *Compatible adhesive.* The polymerized repair resin must be a strong adhesive to the matrix and reinforcement.
- *Long shelf-life.* The repair resin should be stored as a dormant liquid until it is needed for repair applications. If the storage life is not very long, then the unused, expired material will generate unnecessary expense and hazardous waste.
- *High Temperature Stability.* Many military composites require stability at elevated temperatures up to 500°F (260°C) for aircraft exhaust, engine cowlings, etc. In order to repair these composites, the polymerized resin should have a glass transition temperature ( $T_g$ ) above the maximum temperature that the composite will experience in service.
- *Environmentally Benign.* Increasing environmental and safety concerns and regulations dictate that the repair process not generate significant volatile organic compounds (VOCs) or hazardous air pollutants (HAPs).

## High-temperature Resins

High-temperature organic polymers are loosely classified as polymers that maintain their useful properties after thousands of hours in air at 200°C [16,17]. High-temperature thermosetting polymer matrices include cyanate esters (polycyanurates), polyimides, and bismaleimides (BMIs). Of these, polyimides have the highest  $T_g$ 's [18], and the  $T_g$ 's of polycyanurates are usually lower than BMI's [19]. The suitability of a high-temperature polymer for a resin injection repair is significantly dependent on the state of the monomer at low or room temperature. In order for resin infusion to be possible, the pre-polymer (monomer) should be a liquid with a relatively low viscosity that allows complete infusion of the damage zone delamination and surrounding microcracks. The solvent diluted low-temperature epoxies currently used for resin infusion repairs meet this requirement, but most high-temperature pre-polymers are either solids or highly viscous liquids at room temperature. In general, polymers with higher  $T_g$ 's in the cured state tend to have higher viscosities at room temperature. Figure 3 shows the correlation between the cured state  $T_g$  and the temperature at which the uncured thermoset monomer has a viscosity of 0.15 Pa.s [20]. Polyimides are not shown in Figure 3 because their lowest melt viscosities are higher than 0.15 Pa.s [21].

From Figure 3, the one exception to the trend that a higher  $T_g$  corresponds to a higher viscosity is a unique type of cyanate ester monomer called the bis(4-cyanatophenyl)-1,1-ethane monomer (or bisphenol E cyanate ester) [20-22]. A standard bisphenol A cyanate ester has a melting point of 82°C, but the bisphenol E dicyanate has excellent processing capabilities even at low temperatures with an extremely low viscosity of 0.090 to 0.120 Pa.s at room temperature [20-22]. These processing characteristics make the bisphenol E cyanate ester (BECY) an excellent candidate for the resin infusion repairs of high-temperature polymer matrix composites.

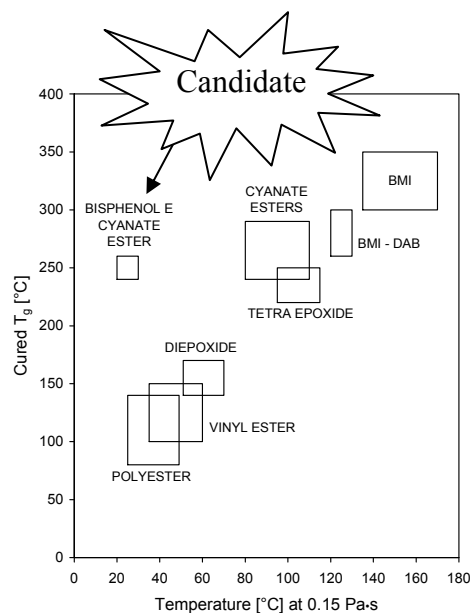
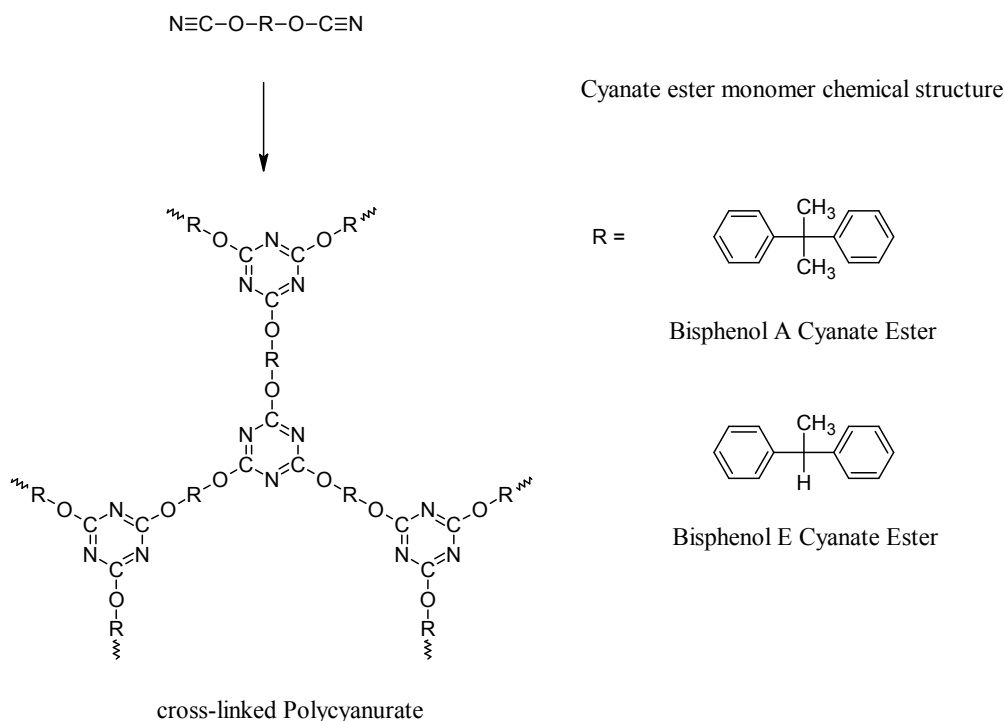


Figure 3. Cured  $T_g$  vs. 0.15 Pa.s Temp.

In general, cyanate esters, correctly named polycyanurates in the polymer form, are characterized by monomers containing reactive ring-forming cyanate ( $-O-C\equiv N$ ) functional groups [18,19,23]. Cyanate esters are a relatively new class of thermosetting polymers that have become a popular replacement for other thermosets in the aerospace and microelectronics sectors because they possess a good combination of high temperature stability and excellent mechanical properties [24]. While cyanate esters are not capable of withstanding as high of temperatures as bismaleimides, they are capable of withstanding extreme temperature variations, which is a significant improvement over epoxies. In addition, cyanate esters have excellent adhesive properties and are more resistant to moisture absorption than other thermosets [25].

Cyanate ester monomers are generally polymerized via cyclotrimerization to polycyanurates (Figure 4). The formation of substituted triazine rings via the cyclic addition of three aryl cyanates involves a series of step-growth reactions. Cyanate esters have extremely low toxicity, which makes them much less hazardous than polyimides and bismaleimides [20,26]. Curing of cyanate esters is catalyzed by heat or a combination of heat and a catalyst, which is most commonly a transition metal [18]. The prepolymer also has near infinite room temperature stability, facilitating reduced wastes due to spoilage compared to traditional thermosets.



**Figure 4. Cyanate ester chemical structures and cyclotrimerization reaction scheme.**

### ***Nanocomposites for Rheological and Adhesive Enhancement***

Conventionally, as is well known, the rheological properties (e.g., flow properties) of liquids are characterized by their viscosity,  $\eta$ , its resistance to flow under stress. For Newtonian liquids the shear rate is proportional to the shear stress and hence the ratio is constant, i.e. constant viscosity. However, for many suspensions there is no such linear relation between the rate of shear and the shearing stress, and the rheological behavior is said to be non-Newtonian. Dispersions containing particles exhibit *plastic flow (Bingham flow)* which require a minimum

shear stress before flow commences (yield stress) and represents a large body of suspensions such as paints, printing inks, clay pastes and industrial slurries.

Other dispersions exhibit *pseudoplastic flow* in which there is no initial yield value and with increasing rate of shear an apparent decrease in viscosity occurs, the shear stress against rate of shear curve being convex to the shear stress axis.

Thus, the flow properties of dispersions is rather complex and at the present, no universal theory exists for the interpretation of flow behaviors and their relationship to parameters (e.g., particle size, volume fraction, and interparticle interaction) of the media and suspended phase.

Generally, the viscosity of colloidal suspensions is affected by the following factors [27]: (i) medium of the suspension; (ii) shape, density, size and size distribution of the particles; (iii) volume actually occupied by the particles in suspension; (iv) thermodynamic conditions of the system (T, P); (v) presence and concentration of electric charges in the system; (vi) shear rate.

For a given suspension system the viscosity can be expressed as

$$\eta = f(\phi, \psi) \quad (1)$$

$\phi$ —volume fraction of suspended particles;  $\psi$ —the term of interactions between particles and particle with medium.

Due to the extremely low viscosity and good wetting characteristics of some cyanate ester monomers, such as bisphenol E cyanate ester (BECY), along with their high degree of adhesion and cross-linking, it is proposed that these resins would make excellent candidates for the incorporation of nano-reinforcement. In many systems, the nanocomposite has been shown to benefit from increased thermal stability ( $T_g$ ) and mechanical performance (strength, stiffness, and dimensional stability). Recent results also indicate that the incorporation of nanoparticles into thermosetting adhesives increases the adhesive strength by as much as 45% [28], further optimizing the nanocomposite systems for repair applications. In addition, numerical simulations using molecular dynamics suggest that the inclusion of nanoparticles into a prepolymer mixture results in an increased volume fraction of nanoparticles near the crack tip due to depletion attraction effects. This results in a subsequent significant reduction in the stress concentration at the crack tip due to the presence of these nanoparticles [29].

Very little experimental data exists in the literature for the viscoelastic behavior of nanosize particle/polymer matrix composites. The behavior of nanoparticle suspended in low viscosity monomer can be approximated to that of nanosize particles suspended in aqueous solution provided that the particle surface is appropriately functionalized.

The vast majority of the literature on the role of particle size on rheology deals with particles in the micron or sub-micron range [30 -34]. The flow characteristics of several alumina aqueous suspensions with particle sizes ranging from the sub-micron to several microns all exhibited shear thinning behavior approaching a constant value at high shear rates. The limiting viscosity values were reached at different shear rates; such that the smaller the particle size the higher the shear rate at which limiting viscosity is reached. It was claimed that as the shear rate



**Figure 5. Example of thixotropy caused by the incorporation of nanosized particles: viscosity is low when shear force is applied (front), and higher when at rest (rear) (Photo courtesy of Cabot Corp.)**



increases the floc network is broken and the “entrapped” fluid is released. If the entrapment of fluid by flocs is responsible for the high viscosity, the effect should be much more pronounced as particle size decreases. Indeed, several experiments [35,36] confirm this trend. Extrapolation of this model to nanometric particle suspensions implies that the viscosity and yield strength of nano-particle suspensions should be higher resulting in gel at zero shear and low viscosity liquid at high shear rates.

Rand and Fries [37] reported one of the few studies on nanometric particle (10.7 nm) suspensions. The solids loading was limited to 5 to 15 vol% because of fine particle size. They too observed that as the particle size decreases the thixotropic behavior is much more pronounced due to increased interaction of the fluid with the particle surface. This behavior can be extremely attractive for the proposed work as not only addition of particles to the monomer allows us to adjust the viscosity of the system but also shear thinning will allow easy injection to the damaged region and will provide sufficient integrity to the suspension until the monomer is cured in the repair area (an analogous behavior for silica suspension is shown in Figure 5).

## Materials and Methods

### ***Cure Kinetics (neat BECy)-Experimental***

BECy monomer is obtained from BRYTE technologies, Inc. as EX1510 cyanate ester. BECy is mixed with catalyst (BRYTE technologies, Inc., supplied with EX1510 cyanate ester) in a weight ratio of 100:3 at room temperature by magnetic stirring.

Thermogravimetric analysis (TG) measurements were performed on a TG model Q50 (TA Instruments, Inc.) to determine the decomposition temperature of polymerized BECy and volatile contents during the polymerization. About 20 mg uncured resin was placed in platinum pans and heated from 25 °C to 800 °C at a rate of 20 °C/min under nitrogen or air purge at 60 mL/min.

Differential scanning calorimetry (DSC) measurements were made on a model Q2000 DSC (TA instruments, Inc.) for isothermal and dynamic cure experiments. A helium flow of 25 mL/min was used as purge gas for all the DSC experiments. Fully or partially cured solid BECy samples were sealed into standard aluminum DSC pans. The liquid samples, uncured mixture of BECy monomer and catalyst, were transferred into hermetic aluminum pans using a pipette and sealed with lids.

Uncured samples were tested first by DSC in the dynamic scan mode from –80 °C to 350 °C at 10 °C/min heating rate. This temperature scan range allowed for observation of the glass transition of BECy monomer and was below the decomposition temperature of the polymerized BECy. Integration of the exothermal peak gives the value of the total reaction heat  $\Delta H_T$ . A fully cured sample was also performed under these dynamic scan conditions to determine the  $T_g$  of the fully cured BECy.

Two different methods were used to evaluate conversion versus time of BECy under isothermal cure conditions. In method I, partially cured samples were prepared by pouring catalyzed BECy into silicon rubber molds followed by isothermal cure in an oven at a preset temperature ( $T_c$  = 180, 200 °C). After various curing times, ranging from 1 min to 6 hrs, samples were removed from the oven and quenched to room temperature with liquid nitrogen. A small piece (~10mg) was cut from the sample for subsequent dynamic DSC evaluation from –80 °C to

350 °C at 10 °C/min. From these experiments both the residual reaction heat  $\Delta H_r$  and  $T_g$  of partially cured samples were obtained simultaneously.

To perform the isothermal curing method II, uncured BECy samples (~8 mg) were sealed in a hermetic pan with a lid and loaded into the DSC cell. The DSC cell is heated up to cure temperature ( $T_c$ =160, 170, 180, 200 °C) at a heating rate of 100 °C/min, and then isothermally soaked from 1 to 6 hours depending on the cure temperature used. After the first scan is finished, the DSC cell is cooled down to 25 °C, and a second scan with the same temperature profile as the first is performed to obtain the baseline for analysis. Finally, the same sample is evaluated in dynamic mode from room temperature to 350 °C at 10 °C/min. The residual reaction heat  $\Delta H_r$  is used to calculate the final conversion of the sample at the various isothermal cure temperatures. The cure kinetics of uncured BECy samples are also evaluated from dynamic scanning experiments at multiple heating rates of 2, 5, 10, 15 and 20 °C/min.

### Comparison to Benchmark Materials-Experimental

**Benchmark Materials**—Two benchmark resin systems were selected to which to compare the BECy based composite adhesive. A bisphenol-A type epoxy resin EPON-828 (Miller-Stephenson Chemical, USA) and the room-temperature amine curing agent DETA (Miller-Stephenson Chemical, USA) was chosen as one of the benchmark matrix systems. In addition, a high temperature cycloaliphatic epoxy resin (CA, 3,4-epoxycyclohexylmethyl 3,4-epoxycyclohexanecarboxylate, Sigma-Aldrich, USA) mixed with an anhydride curing agent (HHPA, hexahydro-4-methylphthalic anhydride, Sigma-Aldrich, USA) in the presence of initiator (EG, Ethylene glycol, Sigma-Aldrich, USA) and catalyst (DBA, *N,N*-Dimethylbenzylamine, Sigma-Aldrich, USA) was chosen as a second benchmark matrix system.

The diluent chosen for our experiments was butyl glycidyl ether. Literature reports the viscosity of BGE in the range of 0.02 to 0.03 Pa.s. BECy has a viscosity of approximately 0.70 to 0.75 P and approximately 1 P before and after the addition of catalyst, respectively, and therefore a viscosity of roughly 1 P was the target viscosity for the two benchmarks. Chemical structures of the thermosetting matrix resins and diluent are represented in Figure 6 below.

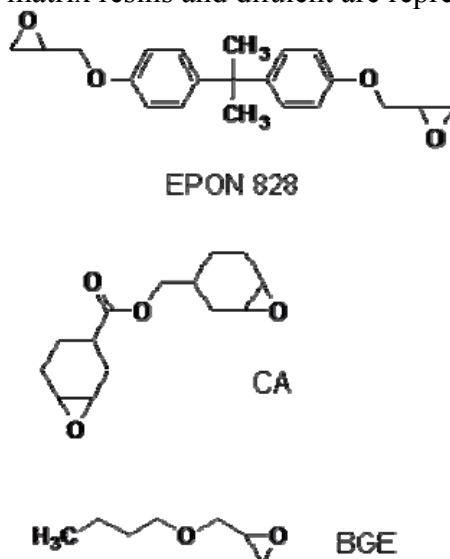
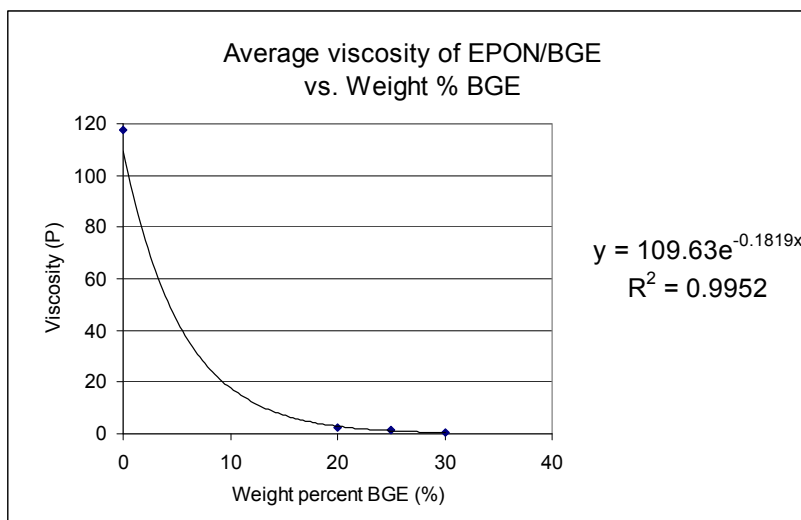
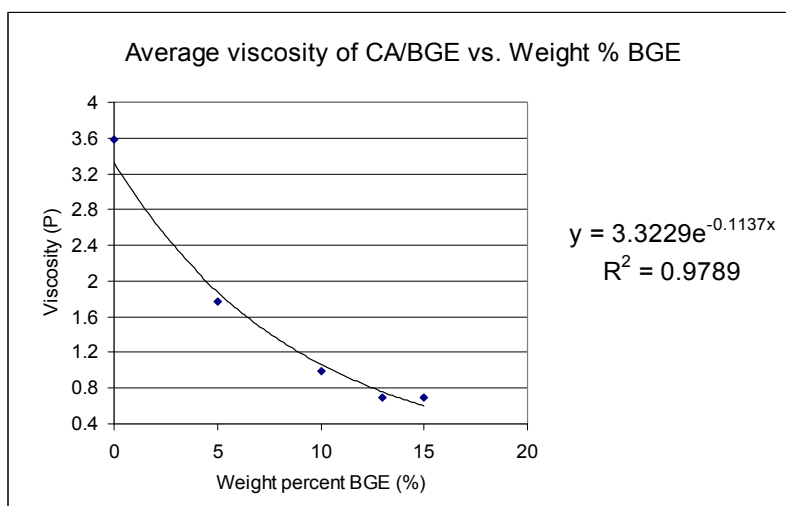


Figure 6. Chemical structures of matrix resins used in the benchmark systems.

A Brookfield Cap 2000+ viscometer was used to determine the viscosities of two benchmark adhesives: EPON 828 (EPON) and a cycloaliphatic epoxy (CA), and our bisphenol E cyanate ester (BECy). It is reasoned that because the viscosities of the two benchmark adhesives are significantly higher than the BECy resin, diluents must be utilized in order to process the two in a similar manner, and so viscosity experiments were used to determine the amount of diluent that must be added to the benchmarks to attain a viscosity similar to BECy.



**Figure 7. Viscosity of EPON/BGE solution versus weight percent BGE added.**



**Figure 8. Viscosity of CA/BGE solution versus weight percent BGE added.**

Different weight percents of BGE were added to uncured EPON and CA and then tested on the viscometer. It was noted that the viscosity of the resin/BGE solutions showed an increase in viscosity over time, which was attributed to the evaporation of diluent due to the open nature of the viscometer as well as the high shear rates used during testing. Evaporation was confirmed

through the weight loss of the solutions over time. Of several runs, the average viscosity for each resin/BGE solution was plotted against weight percent BGE added (Figure 7 and Figure 8). From these experiments, it was determined that approximately 25 wt% and 10 wt% BGE would be used for the EPON and CA systems, respectively.

*Lap Shear Testing*—The adhesive strengths of the BECy adhesive (without nanofillers) and the baseline epoxy systems (EPON and CA systems) were evaluated using lap shear adhesive testing at both room temperature and elevated temperature. These tests were conducted on aluminum substrates according to ASTM Standard D1002-05.

*Volatile Organic Content*—We have evaluated the volatile content of the various components of the three adhesive systems according to ASTM standard 1259-85. These experiments were also compared with thermogravimetric analysis (TGA) in both dynamic heating and isothermal conditions. The ASTM standard called for the heating of a 1 g, 3" diameter film of a sample on aluminum foil at 105 C for ½ hour for non-heat-reactive systems, and 2 hours for heat-reactive systems. For all results shown, samples were heated only for a ½ hour. TGA experiments under the same isothermal conditions were also performed as a concomitant measurement of the volatile content. In addition, dynamic (constant heating rate) TGA experiments were performed to further quantify volatility.

### ***Cure Kinetics (nanoparticle filled BECy)-Experimental***

Alumina and Silica nanoparticles were used to prepare nanoparticle filled BECy. The effects of nanoparticles on the cure kinetics of BECy were investigated. Alumina nanoparticles were obtained from Nanophase technologies, Inc. as NanoTek Aluminum oxide, which is  $\gamma$ -phase alumina with an average particle size (diameter) of 40 nm. Silica nanoparticles were obtained from Degussa, Inc. as Aerosil-OX50 fumed silica with average particles size of 40 nm. Before use, the nanoparticles were dried in the vacuum oven at 120°C for 24 hours.

The dried nanoparticles were weighted in the vial first. Then, BECy monomer was added according to the desired nanoparticles loadings. The total weight of mixture was around 3 g. The vial containing the mixture of BECy and nanoparticles was sealed with lid, and placed into an ultrasonic water bath. After two hours of bath ultrasonication treatment, a high power tip-ultrasonication was applied for 30 seconds, yielding a well-dispersed suspension of BECy/nanoparticles ready for further experiments.

Compared to the catalyst supplied with BECy monomer, the catalytic effect of nanoparticles is small and over-shadowed by the influence of the catalyst. To evaluate the effect of nanoparticles on the cure of BECy, the uncatalyzed samples were tested with dynamic DSC scans at heating rates of 1, 2, 4 and 6°C/min.

### ***Functionalization of alumina nanoparticles-Experimental***

Introducing the functional groups on the surface of nanoparticles makes the nanoparticles easier to disperse and forms stronger interfacial bonds between the nanoparticles and the polymer matrix.

Three different silanes (Figure 9) were used to functionalize the alumina nanoparticles: (3-Glycidyloxypropyl)trimethoxysilane (GPS), (3-Aminopropyl)triethoxysilane (APS) and Chloro(dimethyl)octadecylsilane (OS). GPS and APS contain epoxy or amino groups, which can

react with BECy and result in covalent bond formation between nanoparticles and the polymer matrix.

The functionalization reaction scheme is shown in Figure 9. Dry THF is prepared by distillation of as-received THF over metal sodium. The dry alumina nanoparticles (4g) were dispersed in the fresh distilled dry THF (150 mL) by ultrasonic bath for 4 hrs. A solution of silane in THF was injected into the suspension via a syringe. The required amount of silane was calculated based on a graft density of 0.5 molecules per square nanometer. An excess 10 time equivalent is used to prepare the solution. The mixture was stirred at 70°C under nitrogen atmosphere for 48 hrs. The nanoparticles were isolated by centrifugation, re-dispersed in THF, and centrifuged again. This washing process was repeated three times, followed by drying with a stream of air. Finally, the functionalized nanoparticles were dried in the vacuum oven at 120°C for 24 hr.

The dried nanoparticles were characterized with thermogravimetric analysis (TG) and Fourier transform infrared spectroscopy (FT-IR). For the TG, about 20 mg of sample was placed in platinum pans and heated from 25 °C to 800 °C at a rate of 20 °C/min under air purge at 60 mL/min. The samples for FT-IR are prepared by grinding functionalized nanoparticles with KBr and pressing to form thin pellet.

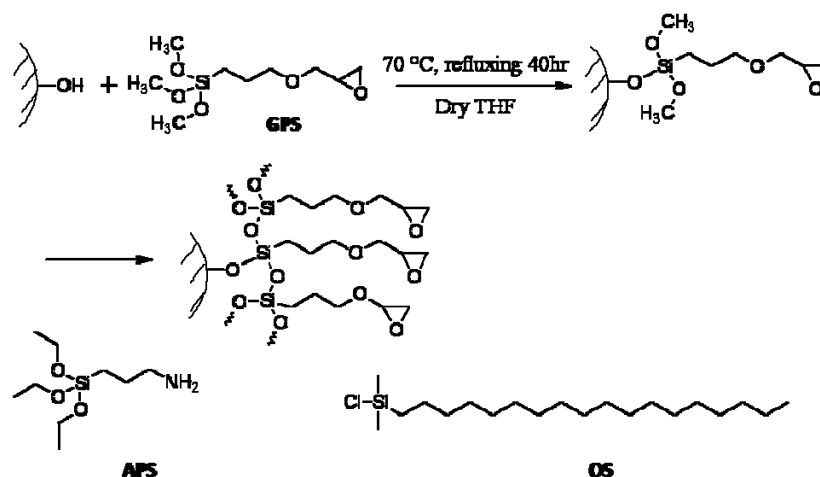
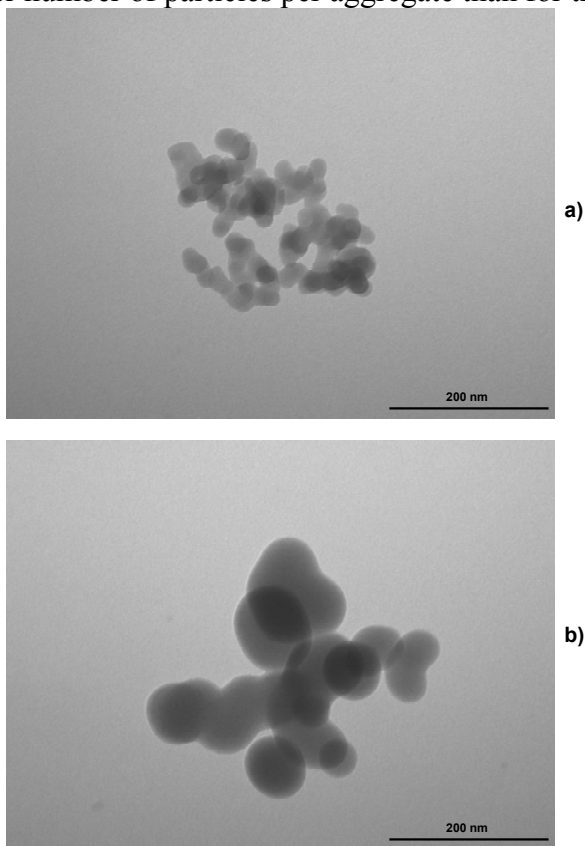


Figure 9. Chemical structure of silanes and functionalization reaction scheme.

### ***Rheology of nanoparticle/cyanate ester suspensions-Experimental***

Hydrophilic fumed silica was supplied by Degussa (Frankfurt, Germany) under the trade names of AEROSIL® 200 and AEROSIL® OX 50 (CAS No.: 112945-52-5, synthetic amorphous, pyrogenic silica, purity  $\geq 99.8\%$ , true density of 2.2 g/cm<sup>3</sup>). AEROSIL® 200 has an average primary particle diameter of 12 nm and a specific surface area of 200 m<sup>2</sup>/g [38]. AEROSIL® OX 50 has an average primary particle diameter of 40 nm and a specific surface area of 50 m<sup>2</sup>/g. The process used to make fumed silica (vapor phase flame hydrolysis of silicon tetrachloride) yields mostly aggregates (primary particles sintered together) that are about 0.2 to 0.3  $\mu$ m in diameter [39].

Figure 10 a) and Figure 10 b) show TEM micrographs of the 12 and 40 nm fumed silica aggregates, respectively. The 40 nm fumed silica has a wider particle size distribution and forms aggregates with a smaller number of particles per aggregate than for the 12 nm fumed silica.



**Figure 10. TEM micrographs of fumed silica aggregates, a) 12 nm, b) 40 nm.**

BECy monomer/fumed silica suspensions were prepared by adding the fumed silica during mixing of the monomer with a 25 mm diameter high-shear blade at 1000 rpm. For the 12 nm particles, compositions of 1, 2, 5, and 6.72 phr (parts per hundred resin) were made, with 6.72 phr (3.4 vol%) representing the maximum loading achieved with ease of processing. For the 40 nm particles, the compositions included 2, 5, 10, 20, 30, 35, and 49.2 phr (max loading), representing volume fractions of up to 20.7 vol%. Prior to mixing, the fumed silica was dried under vacuum and the BECy monomer was preheated to 60 °C. The partially dispersed suspension was processed using a Sonic Dismembrator (Model 100, Fisher Scientific, Hanover Park, IL) with 3.2 mm diameter probe tip for 30 seconds at a frequency of 23 kHz. The power output ranged between 16 and 18 Watts during sonication. After sonication, the suspension was again mixed for 2 minutes at 2000 rpm, followed by an additional 30 seconds of sonication. The temperature of the suspension was maintained between 50 and 65 °C throughout the entire process. Before catalyst addition, a portion of the dispersed suspensions was set aside for rheological evaluation. For the remaining material, catalyst was added to the suspension at a level of 3 phr and mixed at 2000 rpm for 2 minutes, followed by 15 seconds of sonication at the same power level. Finally, the suspensions were poured into high-temperature silicone rubber molds ( $27 \times 48 \times 8 \text{ mm}^3$ ) and degassed at 60 °C for 1 hour under vacuum at 23.4 mmHg. The

catalyzed suspensions were immediately moved to a freezer at -13 °C and stored in sealed containers for subsequent rheokinetic testing and differential scanning calorimetry. Neat BECy control samples without silica were also prepared in the same manner as above.

Uncatalyzed BECy/silica suspensions were tested for rheological properties using a TA Instruments (New Castle, Delaware, USA) AR2000ex stress-controlled rheometer with a forced gas environmental test chamber, utilizing a parallel plate geometry (25 mm diameter disposable aluminum). A gap of 0.5 mm was used, and the temperature was maintained at 22.5 °C  $\pm$  0.3 °C. A sample volume of 0.25 mL was transferred to the parallel plates using a 1 mL syringe. A stepped steady state flow test was conducted for each sample from 0.1 to 100 s<sup>-1</sup> (5 points per decade), allowing for equilibrium to be reached at each shear rate.

Additional oscillatory experiments were used to monitor changes in viscosity with time. In these thixotropy recovery experiments, a pre-conditioning shear of 100 s<sup>-1</sup> was initially applied, followed by short oscillatory stress iterations at 0.1 Pa (0.1 Hz) in two-minute intervals, allowing for the sample to rest in between. The environmental chamber was purged with air and maintained at a temperature of 30 °C.

Catalyzed BECy/fumed silica suspensions were tested at an isotherm of 130 °C using the AR2000ex rheometer in stress control at an amplitude of 1000 Pa and 1 Hz, with the 25 mm diameter disposable parallel plates and 0.5 mm gap. The suspensions were applied to the geometry in the same manner as above, and a one-minute equilibrium period was allowed for each sample to reach the test temperature before collecting data.

### ***Thermal-mechanical properties of cured nanocomposites -Experimental***

In this work, the dynamic mechanical properties of fumed silica/cyanate ester nanocomposites are investigated using hydrophilic fumed silica with two primary particle diameters: 12 nm and 40 nm, with specific surface areas of 200 m<sup>2</sup>/g and 50 m<sup>2</sup>/g, respectively. Here we report the effect of both particle size and volume fraction on storage modulus, damping behavior, and glass transition temperature. We compare the composites' storage modulus data to applicable theory for particulate-reinforced composite materials, comparing the increase in storage modulus in both the glassy and rubbery regions. While the elastic modulus may not be significantly affected by interfacial adhesion, damping behavior is very sensitive to the polymer-particle interaction state [40-42]. We attempt to estimate the polymer-particle interaction by analysis of the decrease in damping realized through the addition of varying volume fractions of filler. It is suggested that the hydroxyl functionality of the fumed silica is responsible for a strong interaction with the polymer matrix through the formation of covalent bonds.

The BECy monomer used is a commercially available resin and catalyst from Bryte Technologies (Morgan Hill, CA) called EX-1510. The liquid phase organometallic-based polymerization catalyst (Bryte Technologies, EX-1510-B) was supplied with the resin and was used at the manufacturer's suggested loading of 3 phr. Hydrophilic fumed silica was supplied by Degussa (Frankfurt, Germany) under the trade names of AEROSIL® 200 and AEROSIL® OX 50 (CAS No.: 112945-52-5, synthetic amorphous, pyrogenic silica, purity  $\geq$  99.8%, true density = 2.2 g/cm<sup>3</sup>). AEROSIL® 200 has an average primary particle diameter of 12 nm and a specific surface area of 200 m<sup>2</sup>/g [43]. AEROSIL® OX 50 has an average primary particle diameter of 40 nm and a specific surface area of 50 m<sup>2</sup>/g [43]. The flame hydrolysis process used to make fumed silica yields mostly aggregates (primary particles sintered together) that are about 0.2 to 0.3  $\mu$ m in diameter [44].

BECy monomer/fumed silica suspensions were prepared by adding the fumed silica during mixing of the monomer with a 25 mm diameter high-shear blade at 1000 rpm. For the 12 nm particles, compositions of 0.5, 1, 2, 5, and 6.72 phr were made, with 6.72 phr (3.4 vol%) representing the maximum loading achieved with ease of processing. For the 40 nm particles, the compositions included 0.5, 1, 2, 5, 10, 20, 35, and 49.2 phr (max loading), representing volume fractions of up to 20.7 vol%. Prior to mixing, the fumed silica was dried under vacuum and the BECy monomer was preheated to 60 °C. The partially dispersed suspension was processed using a Fisher Model 100 Sonic Dismembrator with 3.2 mm diameter probe tip for 30 seconds at a frequency of 23 kHz. The power output ranged between 16 and 18 Watts during sonication. After sonication, the suspension was again mixed for 2 minutes at 2000 rpm, followed by an additional 30 seconds of sonication. The temperature of the suspension was maintained between 50 and 65 °C throughout the entire process. A predetermined amount of catalyst was added to the dispersed suspension, corresponding to 3 phr, and mixed at 2000 rpm for 2 minutes, followed by 15 seconds of sonication at the same power level. Finally, the suspensions were poured into high-temperature silicone rubber molds ( $27 \times 48 \times 8 \text{ mm}^3$ ) and degassed at 60 °C for 1 hour under vacuum at 23.4 mmHg, and then placed in a convection oven (preheated to 60 °C) for the final curing process (heat to 180 °C at 1 °C/min, hold for 2 hours, heat to 250 °C at 1 °C/min, hold for 2 hours and cool to ambient at 5 °C/min). Samples were machined from the solid block of material using a diamond blade saw (TechCut 5™ Precision Sectioning Machine with Diamond Wafering Blade, Low-Concentration Diamond Metal Bonded, 6"  $\times$  .020"  $\times$  1/2", Allied High Tech Products, Inc.). Specimens for dynamic mechanical analysis (DMA) were machined to  $23 \times 6 \times 1.6 \text{ mm}^3$ , such that the thickness of each specimen varied by less than 15  $\mu\text{m}$  over its length. Samples for a post-cure study were prepared at 1 phr in the same manner, except the final cure stage at 250 °C was eliminated, such that the initial cure cycle was: heat to 180 °C at 1 °C/min, hold for 2 hours, and cool to ambient at 5 °C/min. After machining the specimens, free-standing post-cures were conducted at temperatures of 180, 210, 240, and 270 °C for 2 hours. Neat BECy control samples without fumed silica were prepared in the same manner as above. All samples were dried at 120 °C under vacuum for 6 hours and kept in a dry environment prior to testing.

Samples were tested using a TA Instruments (New Castle, Delaware, USA) DMA (Dynamic Mechanical Analyzer) Q800 with LN<sub>2</sub> GCA (Gas Cooling Accessory) from 30 °C to 330 °C at a heating rate of 3 °C/min. Constant amplitude of 30  $\mu\text{m}$  at 1 Hz was applied throughout the test, with a static load tracking at 175% of the dynamic force. A low-friction three-point bending fixture with a length of 20 mm was utilized for each test. For each condition, multiple samples were tested (from 2 to 6) and the data was averaged. For measurements where the standard deviation was more than the size of the symbol used in plots, error bars representing one standard deviation were included.

### ***Adhesive strength and repair system evaluation –Experimental***

The strength of adhesive resin bisphenol E cyanate ester (BECy) in repairing high temperature PMC was evaluated by comparing with the benchmark epoxy resin (EPON 828). Butyl glycidyl ether (BGE) was used as a reactive diluent to lower the viscosity of the benchmark resin. The room temperature viscosity of the EPON 828/BGE blend was rheologically tuned to match the room temperature viscosity of BECy.

Bismaleimide-carbon fiber (BMI-cf) prepreg used for manufacturing the PMC substrate specimens was supplied as HTM 512 prepreg by Advanced Composites Group, Inc. (Tulsa, OK).



The composite panels were manufactured at different dimensions depending on the specimen requirement. The hand laid prepreg plies were cured in a hot press at 190 °C under 0.6 MPa (90 psi) pressure for 6 hours followed by a free-standing post-cure for 8 hours at 240 °C based on a schedule suggested by the supplier.

Samples for lap shear tests were machined from a 250 mm × 250 mm plate made from 7 plies of BMI-cf prepreg. Coupons for lap shear tests were machined into 4×1 in according to ASTM 5868-01 standard [45]. The lap shear tests were performed using an Instron 5569 tensile testing machine (Norwood, MA). Lap shear samples were pulled at an extension rate of 0.5 mm/min until failure. High-temperature tests (conducted at 200 °C) were performed using an Instron SFL Heatwave temperature controlled chamber. Samples were allowed to equilibrate for 10 minutes at 200 °C prior to starting the test.

Samples for short beam shear bending (SBSB) tests were machined from a 250 mm × 250 mm plate made from 9 plies of BMI-cf prepreg. Specimens were machined according to the ASTM D-2344 standard [46] with a span length of 30 mm. The SBSB tests were performed with the same Instron tensile testing machine using a 3-point bending fixture at a loading rate of 0.5 mm/min.

For the double cantilever beam (DCB) test specimens, BMI-cf composite panels, 280 mm × 280 mm, were processed following the same cure schedule described above. A 13 µm thick Teflon film (Dupont) was placed at the mid-plane of the panel during the lay-up process to create an interlaminar pre-crack in the DCB specimens. The composite panels were composed of 8 plies with 4 plies on each side of the insert film obtaining a final thickness of 5 mm. These large panels were machined to 130 mm × 25 mm specimens with the Teflon insert creating an initial pre-crack of 62 mm. Finally a pair of loading hinges was adhered to the ends of the DCB specimens for the purpose of providing loading tabs during experimentation. BECy was used as the adhesive between the loading hinges and the DCB specimens, and provided a strong bond between the hinges and substrate even at 200 °C, with failure never occurring at the hinge/specimen interface during the testing.

Experimental setup for DCB test: The specimens were tested using the Instron tensile testing machine at an extension rate of 5 mm/min following the test procedure of ASTM standard D 5528-94a [47]. One edge of the specimen was coated with a thin layer of white correction fluid to aid in measuring the crack length by improving the contrast between the growing crack-tip and the edge of the specimen. The white layer on the edge of each DCB specimen was marked by thin vertical lines separated by a distance of 1 mm to provide a reference for the crack length measurement. Figure 11 shows the test setup of the DCB specimen under extension. A traveling optical microscope along with a CCD camera was used to measure the crack extension with high precision. In order to inject the desired resin (BECy or Epoxy) into the interlaminar fractured area, a previously developed procedure was used [48,49]. The pristine BMI-cf DCB specimens were loaded at room temperature until the crack had extended to a length of 40-50 mm. While testing the pristine sample, the load and displacement was recorded through software along with the optical images of the crack extension at regular intervals. At this point, the load point displacement was held constant and the temperature of the specimen was slightly increased (to 120 °C) using the Instron SFL Heatwave temperature controlled chamber to improve the wettability of the resin on the fractured surface (measurements with a temperature controlled goniometer showed that the contact angle of the BECy resin on the BMI-cf surface decreased at higher temperatures). Then the desired repair resin was injected into the crack tip of the freshly opened fracture zone using a syringe. After

injecting the resin, the specimens were unloaded, clamped closed, and cured in a convection oven with the cure schedule of the adhesive (BECy or Epoxy). After curing the resin, the specimens were reloaded

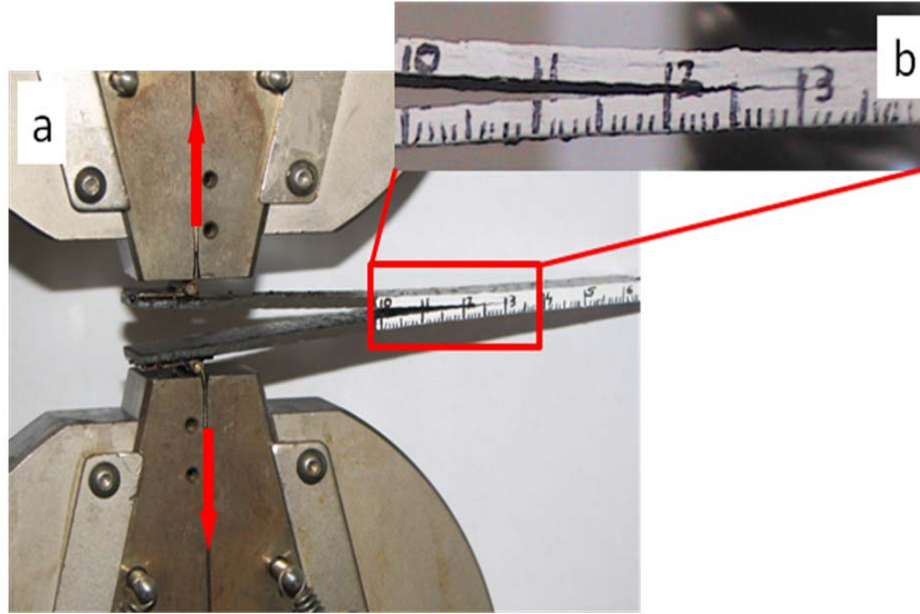


**Figure 11. Experimental setup for DCB testing a) Fracture specimen loaded in crack opening mode to grow delamination b) Close-up image of the crack tip during propagation used to determine crack length.**

to a crack length of 40-50 mm. The load, displacement and crack length were again recorded during the test. In order to study the influence of temperature on the fracture toughness of the adhesive, the DCB tests were conducted at both room temperature and 200 °C with BECy and Epoxy resins.

Based on linear elastic fracture mechanics and beam mechanics, the expression for the mode I strain energy release rate ( $G_I$ ) can be represented mathematically by the following equation.

$$G_I = \frac{3P\delta}{2ba^*} \quad (2)$$

Where  $P$  is the load,  $\delta$  is the crack opening displacement,  $b$  is the width of the specimen and  $a^*$  is the effective crack length. The effective crack length,  $a^*$ , accounts for contributions from shear deformation and rotation that could occur at the delamination front and is determined by adding a correction factor,  $\Delta$ , to the measured crack length, where  $\Delta$  is defined as the  $x$ -intercept in a plot of the cubed root of the specimen's compliance  $(\delta/P)^{1/3}$  versus crack length [50].

Thermogravimetric analysis (TGA) of the neat post cured BMI resin was conducted with a TA Instruments Q50 thermogravimetric analyzer. Samples were heated from room temperature (RT) to 400 °C at 10 °C/min in air.

The fracture surface from the DCB specimens were investigated by scanning electron microscopy (SEM) using a Hitachi S-2460N variable pressure SEM (VP-SEM). The SEM images were collected at different magnifications at specific regions of interest for correlating the fracture morphologies with the mechanical properties of the sample.

The contact angle of BECy resin was measured on a composite substrate to determine the temperature with the best wettability for greatest infiltration of BECy into the composite for repair. One drop of BECy was placed on a composite slide in the contact angle machine. The substrate began at a temperature of 30 °C and the contact angle was measured every min for 10 min. The temperature was then increased to 40 °C. Waited for 10 min for the BECy drop to reach equilibrium, then contact angle measurements were taken every min for 10 min. This procedure was repeated in 10 °C increments up to 150 °C.

A resin-injection repair apparatus was designed such that evacuation of air from within the delaminations and injection of repair resin could be done through the same access hole to avoid the need to drill additional vent holes. The apparatus consisted of a clamping fixture and a series of tubing and connectors through which a vacuum was pulled and resin injected. To repair the delaminations, the plate was sealed within the clamping fixture and a vacuum was pulled through an assembly of tubing, connectors, and valves (not depicted) that were attached to the port on the top of the fixture (Figure 12, Component 2).

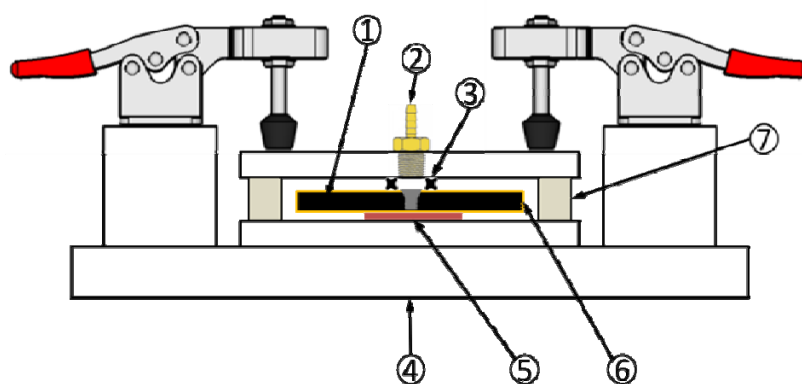


**Figure 12. The apparatus used for the injection repair process. (1) is the composite sample after delamination (2) The well from where the vacuum was pulled and the resin injected (3) quad-ring (4) Polycarbonate base (5) Silicon rubber (6) Kapton tape (7) vacuum sealant tape**

The repair resin was then manually injected via a syringe that attached to a Luer-activated connector that remained sealed to maintain the vacuum until the syringe was attached. After injection, the tubing assembly connected to the port was disconnected, the port re-sealed, and both the fixture and the plate within placed in a convection oven to begin curing the resin. The plate was removed from the fixture and replaced in the oven to fully cure the resin at 180 °C for 2 h, followed by a post-cure at 250 °C for 2 h, at a heating rate of 1 °C/min. Before further testing, resin-filled holes were re-drilled.

The ultra-sonic (C-Scan) machine using 120 kHz focused probes was used to create C-scan images of samples. This was used to illustrate the effectiveness of the BECy repair system. The 4 x 4 in. HPS samples were loaded into a foam mold and the countersunk holes were filled with putty to reduce air gaps, which cause noise or scattering in the images collected. The scan was repeated for the pristine, delaminated, and repaired samples to exemplify the infiltration of the BECy resin.

For further verification of the infiltration and effectiveness of the BECy resin a Florescent Dye Penetration (FDP) Test was performed. Pristine, delaminated and repaired plates were sectioned diagonally to produce a cross section examined via optical microscopy. An electron microscope was used to take pictures of the samples. The Zyglo 150 Penetrant was applied to the cross-section of each sample from the countersink hole to 31 mm away and left for

5 min to soak into the cracks and air gaps within the samples. The samples were lightly rinsed and placed into a convection oven at 65 ° C until fully dried. Photos were then taken with the same electron microscope under UV light at 5x magnification causing the florescent dye to glow and clearly display the delaminations within the samples. This test visually showed the effectiveness of the infiltration of the BECy resin.

The FDP images were used to quantify the effectiveness of the BECy repair. The delaminations and air gaps in the pristine, delaminated and repaired samples were traced using Adobe Photoshop CS4 creating a skeleton of the delaminations. These skeletons were measured manually using a caliper. The total crack propagation per sample was determined, analyzed and compared between sample groups.

To create delaminations for testing the repair capability of the BECy resin the HPS method was used. Nine layers of the prepreg were used for HPS, square plates (101.6 mm x 101.6 mm) were machined from the laminates and a 6.35 mm diameter hole with a 82 degree countersink one third of the way through the was drilled in each plate. The sample was secured between two (steel) plates with a 50.8 mm diameter circular hole in the center to act as a clamp, and centered under the load cell. A steel ball bearing was placed on the countersink hole where the load was applied (see Figure 13). The samples each experienced an initial static load of 250N, then the compressive load was applied at a rate of 1mm/min until a 2 mm extension was reached. This same procedure was followed for HPS samples repaired with BECy mixed with 2.5 wt% and 10 wt% Alumina nano-particles to determine the effect of the nano-particles on composite strength.

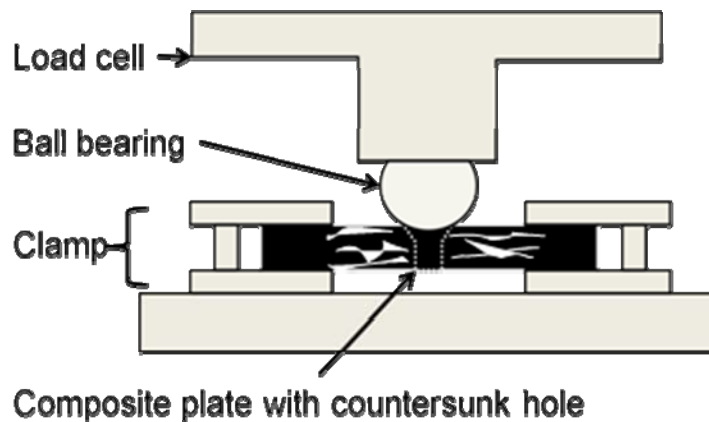


**Figure 13. Hole plate shear method by which delaminations were introduced into composite plates.**

To evaluate the repair efficiency, compression-after-impact (CAI) tests were conducted on undamaged, delaminated, and repaired plates. A standard (ASTM Standard D 7137) CAI test fixture was modified to accommodate smaller-than-standard-sized plates. The fixture and specimen were loaded onto a 250 kN MTS load frame at a compressive extension rate of 1 mm/min (0.04 in/min) until there was a sudden drop in the load with a 5.08 mm in compressive extension limit to protect the fixture from damage. Data from specimens that did not fail within the bulk (e.g. via end-crushing) were not included in calculations.

## Results and Discussion

### Cure Kinetic Modeling-Results

**Thermogravimetric analysis**—The decomposition temperature and volatile content of uncured bisphenol E cyanate ester was measured by TG (Figure 14). The minimal mass loss below 200 °C is mainly volatile content in the BECy monomer and catalyst, such as water and residual volatile solvents. At this temperature range, BECy shows very low (less than 1%) volatile content before curing. Above 400 °C, the cured BECy decomposes, with 5% mass loss occurring at 438 °C and 437 °C in nitrogen and air respectively. In nitrogen, the decomposition rate reaches the highest value at 446 °C and showed a large mass loss to about 46% of the initial sample mass by 800 °C. When the sample was tested under air, it exhibits a similar sudden drop in mass but at slightly lower temperature of 441°C. Under the air atmosphere, oxidation is involved and the entire sample is burned off by the end of the experiment. TG results confirm that the BECy does not generate significant volatile organic compounds (VOCs) and has a very high decomposition temperature, which is desirable for high temperature resin repair applications. It also indicates that the upper temperature limit for subsequent DSC experiments should be below 400 °C to prevent sample decomposition in the cell.

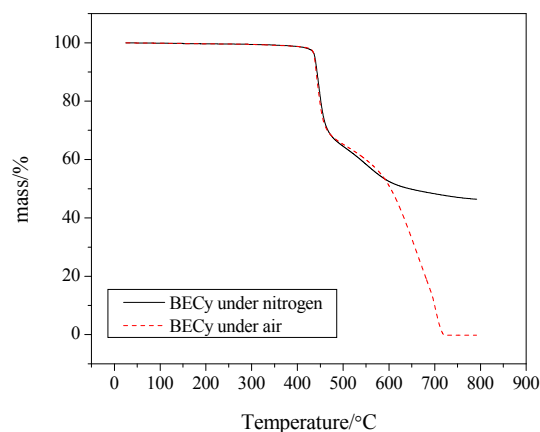


**Figure 14. The TGA curves (at 20 °C/min) of catalyzed BECy under nitrogen and air.**

**Isothermal curing method**—The isothermal curing method I allows for the calculation of residual reaction heat and determination of glass transition temperature from a single DSC scan. Typical dynamic DSC scans of BECy samples, which had first been partially cured isothermally in the oven at 180 °C, are shown in Figure 15. The  $T_g$  (pointed out by arrows) of partially cured BECy increases with increasing isothermal cure time at 180 °C. The exothermal peak area, which occurs after the  $T_g$ , represents the residual reaction heat  $\Delta H_r$ , and decreases with increasing isothermal cure time. The increase of  $T_g$  and decrease of  $\Delta H_r$  indicates how the reaction progresses with the cure time. The conversion of BECy monomer is calculated by

$$\alpha = \frac{\Delta H_T - \Delta H_r}{\Delta H_T} \quad (3)$$

where the total reaction heat  $\Delta H_T$  is determined as 720 J/g by scanning of uncured sample in the DSC cell at a heating rate of 10 °C/min. After first scanning partially cured samples to determine  $T_g$  and  $\Delta H_r$ , a second scan was performed to measure the  $T_g$  of fully cured BECy. The  $T_g$  and

$\Delta H_r$  of partially cured samples and their subsequent  $T_g$  from the second experiment are plotted versus isothermal cure time in Figure 16.

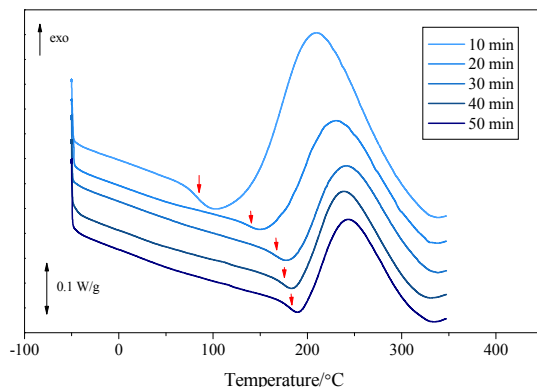


**Figure 15. Typical DSC curves for partially cured BECy samples that were cured at 180 °C for various times.**

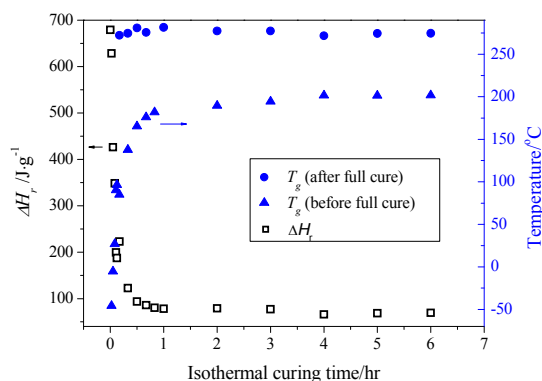


**Figure 16. Residual reaction heat  $\Delta H_r$  and  $T_g$  of BECy samples isothermally cured at 180 °C for various times.**

For short isothermal curing times, it is clear that the residual reaction heats,  $\Delta H_r$ , decrease as the preceding isothermal cure time increases. After curing for one hour at 180 °C, the residual reaction heat,  $\Delta H_r$ , reaches a plateau. Based on these isothermal cure experiments, the highest conversion at a cure temperature of 180 °C is 91%. Therefore, a post-cure process is needed to reach the fully cured state. In Figure 15, the exothermal peak areas, which are proportional to the residual reaction heats, have peak temperatures above the isothermal cure temperature. Additionally, the samples which cured longer than 1 hr at 180 °C all show peak temperatures closed to 250 °C, indicating that a post-cure process should be carried out above 250 °C for the samples to reach the fully cured state.

Isothermal curing method II was performed at four cure temperatures: 160, 170, 180, and 200°C, respectively. As mentioned previously, three individual scans are required to get enough information to plot conversion vs. time for the isothermal curing method II: (1) a first isothermal measurement of uncured BECy sample at the cure temperature for an extended period of time, (2) a second isothermal scan following the same temperature profile to obtain the baseline for data analysis, and (3) a third dynamic scan at 10 °C/min, to measure  $T_g$  and  $\Delta H_r$  (to determine



the value of final conversion). The highest possible conversions without subsequent post-cure processes were found to be 87%, 89%, 91% and 94% at cure temperatures of 160, 170, 180 and 200 °C, respectively. The analyzed isothermal cure plot of conversion vs. time at different curing temperatures is showed in Figure 17 (only the data at the beginning stage of the isothermal cure are shown). The experimental data of conversion vs. time obtained from isothermal cure method I (the residual heat method) is also shown in Figure 17, which matches very closely with the data obtained from isothermal cure method II at the same isothermal cure temperature of 180 °C.

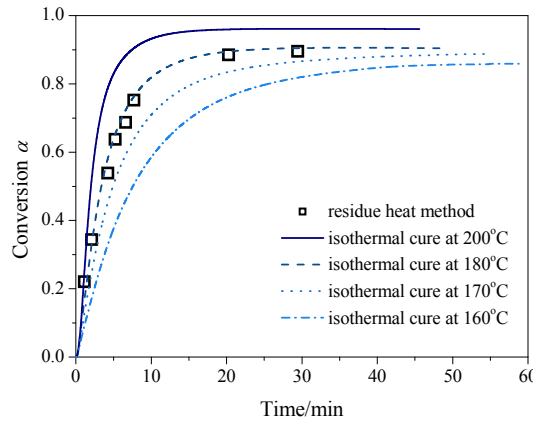


**Figure 17. Plot of conversion vs. time for isothermal cures of BECy at different curing temperature.**

The conversion rate can be defined as follows:

$$\frac{d\alpha}{dt} = \frac{dH/dt}{\Delta H_T} \quad (4)$$

where,  $dH/dt$  is the heat flow rate and can be measured directly by DSC. Modeling equations for the cure kinetics of thermosetting polymers generally have two categories:  $n$ th order and autocatalytic. If more than one chemical reaction occurs during cure, the kinetic model may represent an overall process when these chemical reactions occur simultaneously [51].

For the cure of thermosetting polymers that follow  $n$ th order kinetics, the rate of conversion is proportional to the concentration of unreacted materials:

$$\frac{d\alpha}{dt} = k(1 - \alpha)^n \quad (5)$$

where  $n$  is the reaction order, and  $k$  is the temperature dependent reaction rate constant given by the Arrhenius relationship:

$$k(T) = A \exp\left(-\frac{E_a}{RT}\right) \quad (6)$$

$E_a$  is the activation energy,  $R$  the gas constant,  $T$  the absolute temperature, and  $A$  the pre-exponential or frequency factor. Equation 5 indicates that the maximum conversion rate occurs at  $\alpha = 0$ . The conversion rate is dependent only on the amount of unreacted materials and assumes that the reaction products are not involved in the reaction.

If the reaction products are involved in the reaction, the autocatalytic model will apply:

$$\frac{d\alpha}{dt} = k'(1 - \alpha)^n \alpha^m \quad (7)$$

where, similarly, reaction rate constant  $k'$  follows the Arrhenius relationship,  $m$  the reaction order. According to equation 7, the conversion rate is zero at the beginning of the reaction and reaches a maximum value at an intermediate conversion.

To determine which models will apply to describe the cure kinetics of BECy, a plot of the conversion rate ( $d\alpha/dt$ ) vs. the conversion ( $\alpha$ ) is made and shown in Figure 18. As shown in Figure 17, the conversion rate is equal to zero at the beginning of the cure and has a maximum value around  $10\% \leq \alpha \leq 20\%$  dependent on the isothermal cure temperature ( $T_c$ ). These characteristics indicate that the isothermal cure of BECy is following an autocatalytic model. The fitting results by autocatalytic model are also shown in Figure 18 as solid lines. The autocatalytic model has a good agreement to the experimental data, with the degree of fit  $R^2 > 0.98$ . The kinetic parameters  $k$ ,  $n$  and  $m$  obtained by least squares regression are listed in Table 1. Obviously, the reaction rate constant increases with cure temperature. The isothermal cure of BECy has a total reaction order of 2.4. Based on the logarithmic form of Arrhenius relationship, the plot of  $\ln k$  vs.  $1/T$  (Figure 19) gives the activation energy  $E_a$  as 60.3 kJ/mol and  $\ln A$  as 11.2.

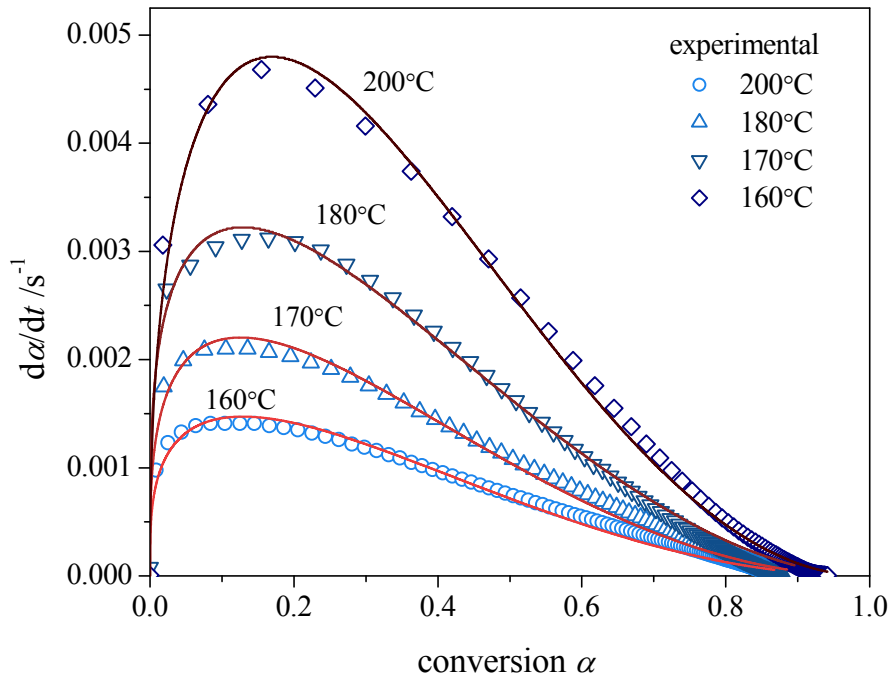


**Figure 18. Autocatalytic modeling of isothermal cure data.**



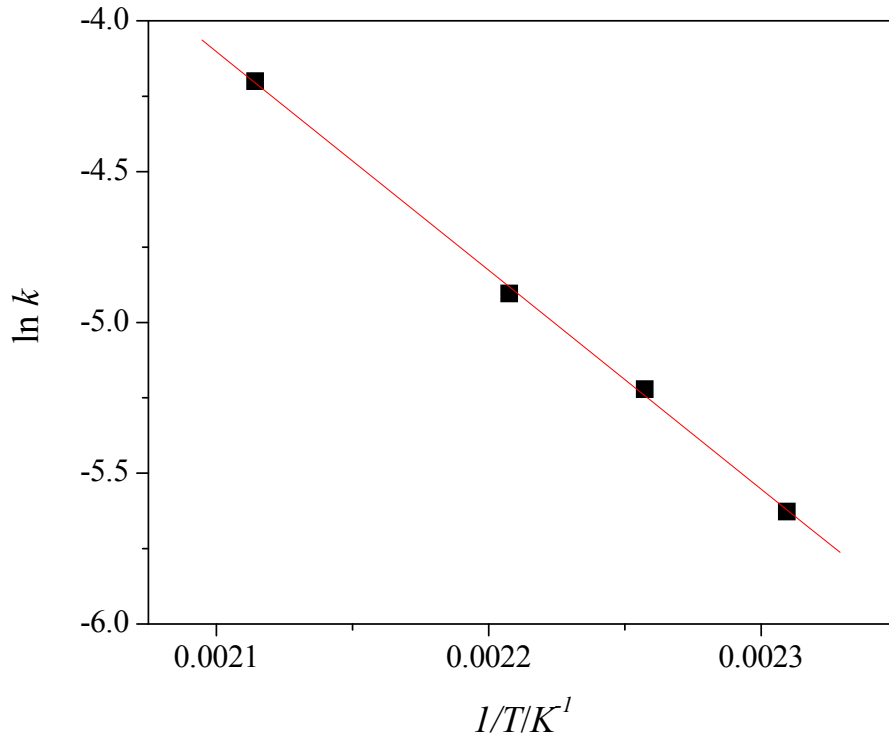


Figure 19. Arrhenius plot obtained by autocatalytic model.

Table 1. Kinetic parameters at different isothermal cure temperature.

Cure temperature (°C)	$k \times 10^{-4}$ (s <sup>-1</sup> )	$n$	$m$	$n+m$
160	36	2.0	0.3	2.3
170	54	2.1	0.3	2.4
180	74	2.1	0.3	2.4
200	150	2.1	0.4	2.5

While the residual reaction heat,  $\Delta H_r$ , is difficult to measure when the reaction reaches a high degree of conversion ( $\alpha > 95\%$ ), the  $T_g$  measurably increases with cure state and serves as a more sensitive measure of conversion than residual reaction heat at the latter stages of cure. There is a one-to-one non-linear relationship between  $T_g$  and conversion  $\alpha$ , independent of cure temperature for this high  $T_g$  BECy system. Therefore,  $T_g$  can be used as a primary variable to transform  $T_g$  to conversion and vice versa, via the one-to-one relationship obtained from a theoretical or empirical fit of the experimental data.

To evaluate the relationship between  $T_g$  and conversion, samples were prepared following the isothermal cure method I procedure: the uncured samples were isothermally cured at 180 and 200 °C, respectively, for various periods of time; and then dynamic DSC scans were performed

to measure the partially cured sample  $T_g$  and conversion  $\alpha$ . A plot of  $T_g$  vs. conversion  $\alpha$  is shown in Figure 20 with the  $T_g$  increasing monotonically with conversion.

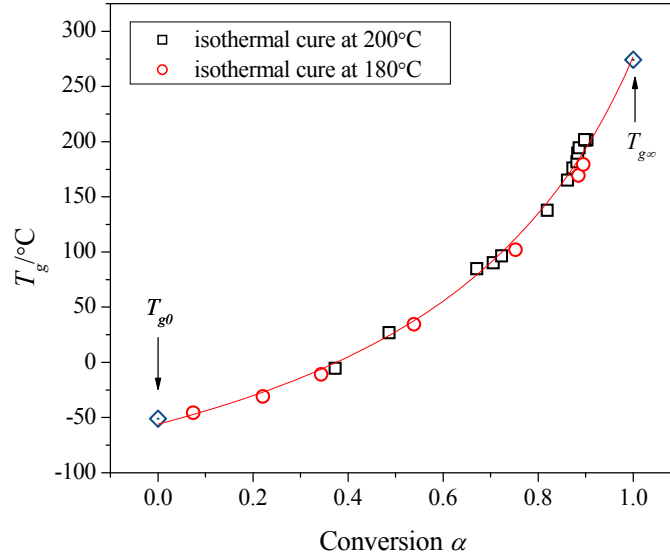


**Figure 20.  $T_g$  vs. conversion plot with DiBenedetto equation fitting.**

In equation 8, the empirical DiBenedetto equation, which is often used to fit  $T_g$  vs. conversion data [52], is rewritten by assuming the partially cured system as a mixture of fully cured polymer and monomer:

$$\frac{T_g - T_{g0}}{T_{g\infty} - T_{g0}} = \frac{\lambda \alpha}{1 - (1 - \lambda)\alpha} \quad (8)$$

where,  $T_{g0}$  is the  $T_g$  of the uncured monomer,  $T_{g\infty}$  is the maximum  $T_g$  for the fully cured sample. The parameter  $\lambda$  is a structure dependent constant, theoretically equal to  $\Delta C_{p\infty}/\Delta C_{p0}$ , where  $\Delta C_{p\infty}$  and  $\Delta C_{p0}$  are the differences in heat capacity between the glassy and rubbery states at  $T_g$  for fully cured sample and uncured sample, respectively.

Taking the  $T_g$  and  $\alpha$  values experimentally,  $T_{g0}$ ,  $T_{g\infty}$  and  $\lambda$  were determined by least squares regression as  $-56^\circ\text{C}$ ,  $277^\circ\text{C}$  and 0.32 respectively. The values of  $T_{g0}$  and  $T_{g\infty}$  listed in Table 2 are very close to the experimentally measured values.  $T_{g\infty}$  obtained by fitting experimental data with the DiBenedetto equation is the  $T_g$  for an ideal fully cured system, which is expected to be slightly higher than the  $T_g$  obtained experimentally from fully cured samples. The parameter  $\lambda$  is difficult to measure accurately with traditional DSC techniques because of the large measurement uncertainties in  $\Delta C_{p\infty}$  and  $\Delta C_{p0}$ ; however, modulated DSC may be pursued in further experiments to experimentally measure the value of  $\lambda$  and compare it with the value obtained through the model fit.

**Table 2. Parameters for the DiBenedetto equation relating  $T_g$  and conversion.**

	$\lambda$	$T_{g0}$ ( $^\circ\text{C}$ )	$T_{g\infty}$ ( $^\circ\text{C}$ )
Calculated value	$0.34 \pm 0.2$	$-55.9 \pm 4.1$	$276.5 \pm 5.6$
Measured value		-51.1	274.3

*Dynamic scanning method*—While the isothermal measurements have the advantage of a complete separation between the variables of time and temperature, dynamic scanning experiments allow for improved investigation of the kinetics at the start and end of the reaction, and the kinetic parameters can more easily be interpreted by a comparison of measurements at different heating rates [53]. Multiple dynamic DSC experiments were performed at heating rates of 2, 5, 10, 15 and 20 °C/min, respectively, to test uncured BECy samples. Figure 21 shows the DSC scans for all of the experimental multi-heating-rate runs for the BECy samples.

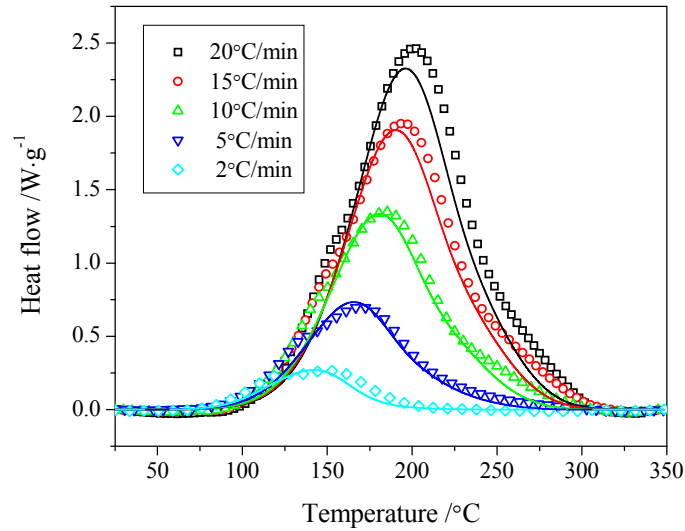


**Figure 21. Dynamic scanning method: experimental DSC curves of uncured BECy (symbols) and model fittings (solid lines).**

The isothermal experiments results indicate that the cure of BECy follows an autocatalytic model. From equation (4), (6) and (7), the heat flow can be expressed as:

$$\frac{dH}{dt} = \Delta H_r A \exp\left(-\frac{E_a}{RT}\right) (1 - \alpha)^n \alpha^m \quad (9)$$

Since the analysis of isothermal experiments gives the values of  $E_a$ ,  $\ln A$  and reaction order  $n$ ,  $m$ , the DSC curves can be modeled by equation 9 which is show as solid lines in Figure 21. The modeling DSC curves fit the experimental ones well, except at in the high temperature regions. The deviation from experimental curves suggest that cure of BECy may not be dominated by autocatalytic model through the whole curing process at dynamic scan conditions and a more complex mechanism is involved.

An isoconversional method, which assumes the conversion is constantly changing with time ( $\alpha = ct$ ), and independent of the heating rate  $\beta$ , can be used to analyze the multi-heating-rate scan data [54,55]. This makes it equally effective for analyzing both  $n$ th-order and autocatalytic reactions.

In the analysis of experimental data from multi-heating-rate dynamic scans, there are two approaches often used to determine curing kinetic parameters: Kissinger's approach [56] and Ozawa [57- 60] approach.

The exothermal peak temperature,  $T_p$ , is shifted to higher temperatures with increasing heating rate. According to Kissinger's approach, the maximum reaction rate  $da/dt$  occurs at  $T_p$ , where  $d^2\alpha/dt^2 = 0$ , and the kinetic equation can be expressed as

$$\ln\left(\frac{\beta}{T_p^2}\right) = \ln\left(\frac{AR}{E_a}\right) - \frac{E_a}{RT_p} \quad (10)$$

Based on Kissinger's approach, a plot of  $\ln(\beta/T_p^2)$  vs.  $1/T_p$  gives the values of the pre-exponential factor  $A$  and activation energy  $E_a$  (where  $\beta$  represents the heating rate in K/s). Figure 22 shows the plot of  $\ln(\beta/T_p^2)$  vs.  $1/T_p$ .

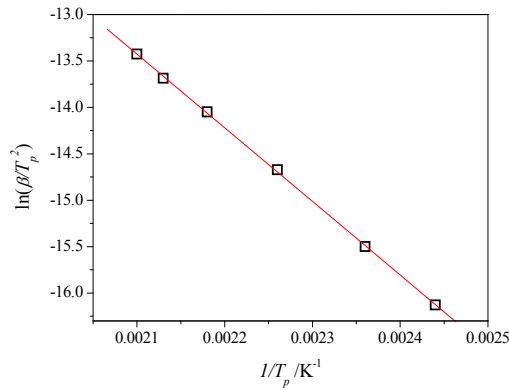


**Figure 22. Plots based on Kissinger's approaches.**

Ozawa approach gives a simple relationship between the activation energy, the heating rate and isoconversion temperature:

$$\log \beta = -\frac{0.4567 E_a}{RT_i} + A' \quad (11)$$

where for each degree of conversion,  $A'$  is a constant that can be expressed as

$$A' = \log \left[ \frac{AE_a}{g(\alpha)R} \right] - 2.315 \quad (12)$$

and  $g(\alpha)$  is a function of the dependence of conversion (60). Similarly, a plot of  $\log \beta$  vs.  $1/T_i$  at each degree of conversion gives a slope proportional to the corresponding activation energy  $E_a$  and an intercept as pre-exponential factor  $A'$  (Figure 23). Therefore, the relationship of activation energy and conversion can be measured through whole reaction. The activation energy decreases with the increase of conversion, after reaching a minimum value at around 30% conversion, it shows an increase, finally decreases again at high conversions (>70%). The decrease of activation energy at beginning is due to the autocatalytic effect of curing process and increase of activation energy is contributed by the forming of cross-linked network which makes the unreacted monomer hard to diffuse. The decrease of activation energy at high conversions is still in question. At high conversions, the reaction is no longer following the autocatalytic kinetics and more complex mechanisms involve the cure process, such as diffusion control. The measured activation energy may not correspond to a real cure process and give large uncertainties. The  $A'$  shows a similar trend as  $E_a$  with conversion in Figure 23. This is due to the

kinetic compensation effect [61], which suggests that the value of  $\ln A'$  varies linearly with  $E_a$ . Both Kissinger's and Ozawa's plots show very good linear relationship between parameters based on the experimental data. The calculated results based on Kissinger's approach are listed in Table 3. Ozawa approach gives an average value of 61.2 kJ/mol, which is slightly higher than activation energy obtained from isothermal curing method.

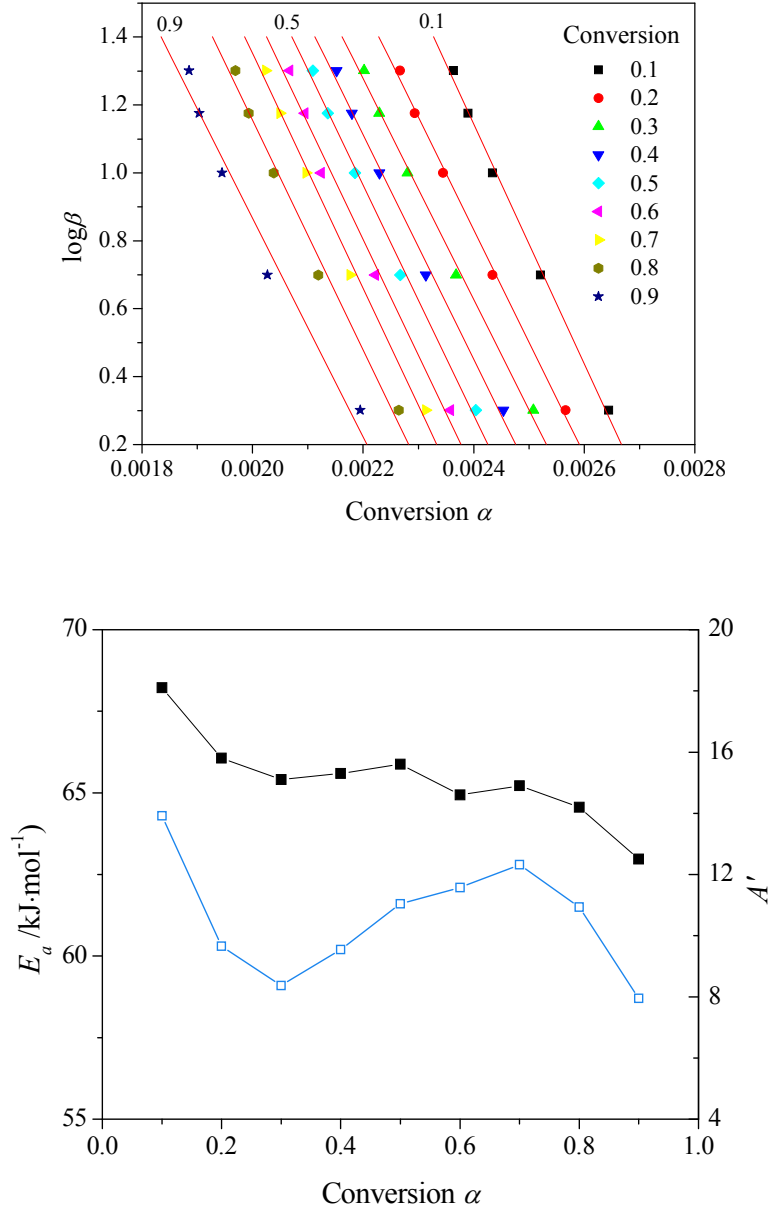


**Figure 23. Isoconversional analysis: Ozawa approach.**

Another isoconversional approach is the Friedman analysis (61):

$$\ln\left(\frac{d\alpha}{dt}\right) = \ln f(\alpha)A - \frac{E_a}{RT} \quad (13)$$

where,  $f(\alpha)$  is a function of the dependence of conversion. Similar to Ozawa's approach, the activation energy and  $\ln f(\alpha)A$  can be calculated from the slope and intercept of a  $\ln d\alpha/dt$  vs.  $1/T$  plot (Figure 24). Friedman analysis shows that activation energy has the similar changing trend as the Ozawa's analysis but shifts to lower conversion stage: the activation energy decreases first and then increases to a maximum value at 50% conversion with the increase of conversion, finally, decreases again at high conversion stages. Friedman analysis gives lower activation energy in average: 56.8 kJ/mol.

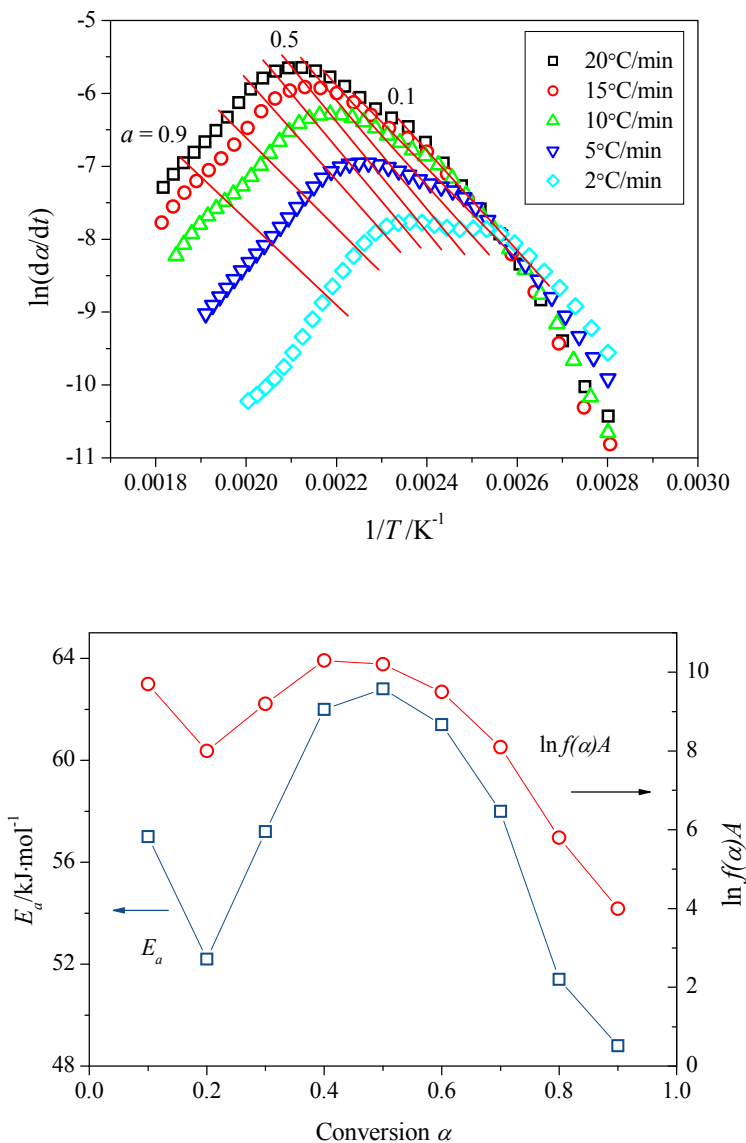


Figure 24. Isoconversional analysis: Friedman plot.

**Table 3. Cure kinetic parameters calculated from Kissinger and Flynn-Wall-Ozawa approach.**

Heating rate (°C/min)	$T_p$ (°C)	Kissinger	
		$E_a$ (kJ/mol)	$\ln A$
20	202.0	66.7±0.4	12.4±0.1
15	195.5		
10	185.6		
5	169.8		
2	150.3		

The activation energy  $E_a$  of BECy is lower than the 80 kJ/mol of the similar bisphenol A cyanate ester system and close to the reported value of 68.5 kJ/mol calculated from a WLF diffusion-controlled model in Ref. [62]. The lower activation energy  $E_a$  implies lower required cure temperatures to polymerize the resin, which is favorable for composite repair applications.

### ***Comparison to Benchmark Materials –Results***

*Volatile Organic Content*—The volatile content measured per the ASTM 1259-85 standard (where 1 g of a sample was held at 105 °C for ½ hour) was qualitatively similar to the concomitant TGA measurements (where about 20 mg of sample was held at 105 °C for ½ hour). Quantitative differences are likely due to differences in the mass and surface area for the different tests. We believe that the TGA measurements are more accurate due to the increased accuracy of the measurement system. The isothermal TGA results are shown in Table 4. The BECy has just 0.7% volatile content (as defined by the ASTM standard isotherm for 30 min) while the BGE diluted EPON and CA epoxies had volatile contents of 24.8% and 11.7% respectively. While the neat EPON 828 resin did have a lower volatile content than the neat BECy resin (0.4% vs. 0.7%), that system has a much higher viscosity and is not being considered as a suitable benchmark system unless it is diluted with the reactive diluent (BGE). The last two columns in Table 4 are the time (and corresponding temperature) when complete volatilization of the sample is complete (when the entire sample is gone). The BECy sample has the highest final temperature, possibly because thermal polymerization of the monomer occurs at the very high temperatures, precluding volatilization of the monomer.

**Table 4 Comparison of Volatile Content from TGA.**

	<b>TGA</b> <b>(105 °C for ½ h)</b>	<b>TGA</b> <b>(ramp until 100% wt. loss)</b>	
	Change in wt%	Time (min) at 0 wt. %	Temperature (°C) at 0 wt. %
BECy	0.7	36.2	741
EPON	0.4	28.4	584
CA	1.4	23.4	490
EPON/BGE	24.8	27.0	556
CA/BGE	11.7	26.5	545

The incorporation of BGE into the systems greatly increases the volatile content since BGE itself is so volatile. BGE was too fluid to test following the same ASTM standard, but in the TGA, there was a 100% wt loss. The TGA ramp tests showed again that the BECy decomposes at a much higher temperature than the benchmark systems with BGE. The incorporation of BGE seems to have different effects on the two benchmark systems. In the CA/BGE system, the temperature at 100% weight loss was increased from 489 to 545 C, whereas in the EPON/BGE system, the temperature at 100% weight loss was decreased from 584 to 556 C.

While these experiments indicate that the BECy is significantly less volatile than the diluted epoxy benchmark systems, additional testing is planned in the next few months to better quantify these VOC levels. We had planned to measure the chemical content of the TGA effluent using a residual gas analyzer (coupled TGA-RGA), but our RGA system could not be coupled with our TGA instrument. Instead we are in the process of contacting external test labs to make these measurements for us.

### ***Adhesive strength and repair system evaluation-Results***

*Lap Shear Testing*—Room temperature (RT) tests demonstrated the superiority of the bisphenol-E cyanate ester (BECy) system over the benchmark systems in maximum load and extension. Due to the desired application of BECy resin being the repair advanced PMC's used mainly for high temperature applications, the lap shear strength was tested at both room temperature and at 200 °C. At RT, the BECy system showed approximately a 98%, 48%, 138%, and 113% higher maximum load than the EPON, EPON/BGE, CA, and CA/BGE systems, respectively; and at 200 °C, showed an approximately 3000% and 2000% higher maximum load than the EPON/BGE and CA/BGE systems, respectively. The results of the lap shear experiments are quantified in Figure 25.



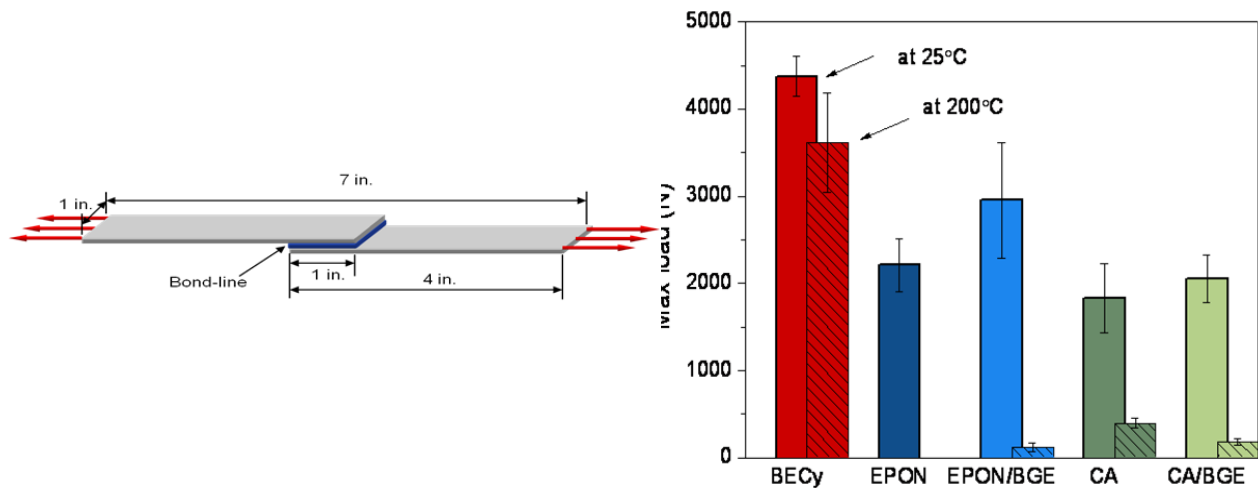


**Figure 25. Results of lap shear experiments on an aluminum substrate at room temperature and elevated temperature.**

The lap shear tests in Figure 25 were conducted on aluminum substrate, hence to correlate the observed bond strength on metallic substrate to the target application, the lap shear tests were repeated with PMC substrate. Bismaleimide/carbon fiber (BMI-cf) PMC that is widely used in advanced aircraft structural composites and high temperature applications was used as the substrate. BMI composite panels from carbon/BMI prepreg as per ASTM 5528-01 were manufactured at different dimensions depending on the specimen requirement.

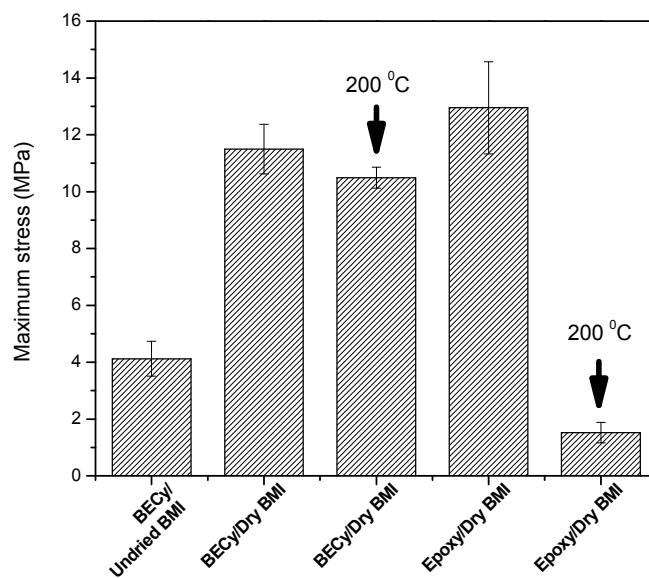


**Figure 26. Results of lap shear experiments on a BMI/carbon fiber substrate at room temperature and elevated temperature.**

Figure 26 compares the average lap shear strength measured for the BECy adhesive with the benchmark Epoxy resin on BMI-cf substrates at both room temperature and at 200 °C. While preparing the first batch of samples with BECy adhesive, an unusual occurrence was observed in the samples after curing the adhesive; the samples exhibited bubbles on the edges of the overlap area. Such bubbles suggest the formation of voids in the bond-line which ultimately reduced the mechanical performance of the adhesive.

To avoid such voids the influence of various factors, including surface preparation, cure schedule of the BECy resin, and desorption of volatile gases from the BMI-cf substrate was systematically investigated. Varying the surface preparation or cure schedule did not significantly reduce the occurrence of bubbles. In order to investigate the desorption of volatile gases from the BMI-cf substrate, TGA tests examining weight loss behavior with respect to temperature were conducted on post cured BMI resin (PC-BMI). As shown in Figure 27, a weight loss of 2% at ~250 °C was observed in the first temperature ramp, which was not observed in the second temperature ramp conducted immediately after the first ramp. After the second ramp, the sample was stored in the lab environment at room temperature for 5 days and then the same TGA experiment was conducted again on the same sample. Interestingly, the same TGA weight loss profiles were observed in both 1<sup>st</sup> and 2<sup>nd</sup> ramps after 5 days. Therefore, the TGA results suggest that post-cured BMI absorbed ca. 2 wt.-% moisture from the lab atmosphere. We hypothesize that the residual moisture in the BMI substrate is released at high temperature during the cure of the BECy, resulting in void formation and lower adhesive strengths

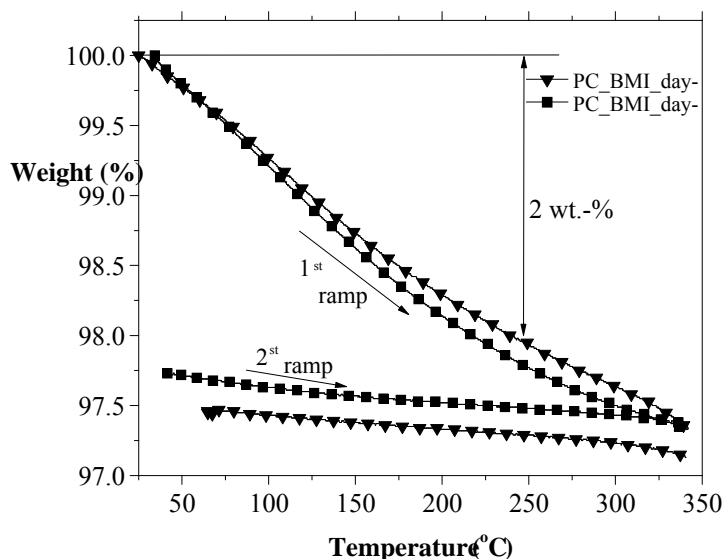
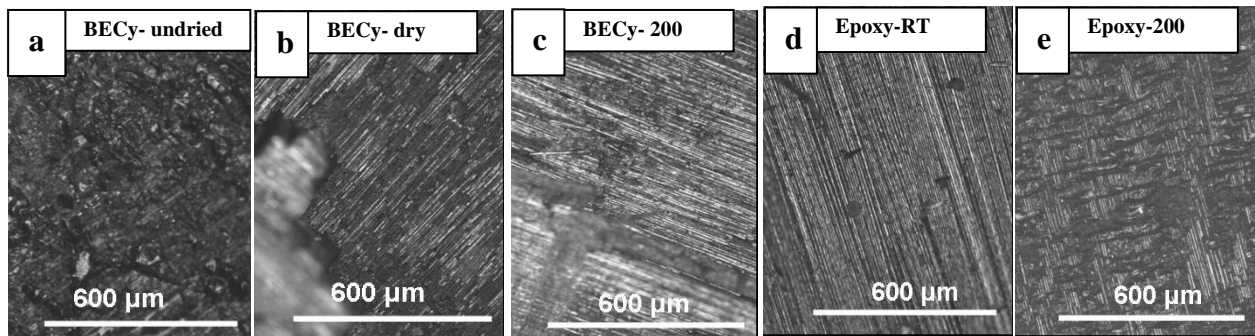


Figure 27. TGA of post-cured BMI illustrating the moisture desorption of 2 wt.-% at 250 °C.

A dramatic increase in the bond strength of BECy was achieved by drying the BMI-cf substrates for 24 hours in a vacuum oven at 100 °C before bonding. As shown in Figure 26, a threefold enhancement in the lap shear strength is observed in samples prepared with dried substrates (BMI-cf-dry) compared to the undried substrates (BMI-cf-wet). The bond strength of BECy at 200 °C on dried BMI-cf substrates was observed to be comparable to the bond strength at room temperature, which reveals that the adhesive strength of BECy is stable over a wide

temperature range. The lap shear strength of BECy was observed to be similar to the benchmark Epoxy (within the error limits) at room temperature, whereas it significantly outperformed the Epoxy at high temperature. This is mainly because the Epoxy has a glass transition temperature well below 200 °C [63].

Significant variation in the fracture mechanism at the adhesive bond was also observed by comparing microscopic images of post fractured surfaces with respect to the adhesive type, moisture content, and testing temperature. Figure 28 (a-e) shows the microscopic images of lap shear fracture surface of BECy and Epoxy resins. Figure 28a and 28b show the fracture surface of BECy on undried and dried BMI-cf substrate, while the lap shear fracture surface of BECy at 200 °C is shown in Figure 28c. The fracture surfaces of the Epoxy benchmark resin at room temperature and 200 °C are shown in Figure 28d and 28e. In a typical adhesive bonded lap shear joint, the joint can fail in three different ways: (1) cohesive failure, where failure occurs within the adhesive; (2) adhesive failure, where failure occurs at the adherent/adhesive interface; and (3) adherent failure, where failure occurs in the substrate or adherent. Cohesive failure appears to be the dominant mode for the BECy-wet samples, where traces of adhesive can be seen on the fracture surfaces. In contrast, after drying the substrate, the mode of fracture appears to be a mixed mode failure of both substrate and interface. In BECy-wet, the moisture content evolved while curing BMI-cf substrates results in the formation of voids in the bond line. These voids strongly reduce the adhesive strength of BECy. The micrographs of the BECy-wet in Figure 28a clearly demonstrates that the fracture took place within the adhesive without creating any fresh substrate surface that is commonly seen in case of adhesive or adherent failure. Whereas, in Figure 28b and 28c, the fracture surface of BECy-dry and BECy-200 shows freshly opened substrate fracture surface with high amount of broken carbon fiber from the substrate, which reveals the fact that the mode of fracture can be either adhesive or adherent failure. The fracture surface images of samples adhered with epoxy resins tested at room temperature (Epoxy-RT) appear to be similar to the fracture surface of BECy-dry, indicating similar fracture mechanisms in both systems. However, the fracture surface of the epoxy resin tested at elevated temperature (Epoxy-200) reveals a liquid like flow behavior in the adhesive, with traces of resin flowing in the shear direction between the BMI-cf substrates (Figure 28d). The flow behavior of epoxy is mainly due to its rubbery behavior at elevated temperatures due to its low glass transition temperature.



**Figure 28. Microscopic images of fracture surface of BMI-cf lap shear specimens demonstrating the various modes of failure under different testing conditions for a) BECy-undried and b) BECy-dry c)BECy-200 d) Epoxy-RT e) Epoxy-200.**

*Short beam shear bending (SBSB)*- SBSB is a common method for characterizing the interlaminar shear strength of fiber-reinforced composites [64,65]. Figure 29a shows representative short beam shear stress-strain curves, and Figure 29b plots the average maximum shear strengths (found from the peaks of the stress strain curves from 4-5 independently prepared SBSB specimens at each condition) for pristine BMI-cf SBSB specimens and BMI-cf SBSB samples that are repaired with BECy and Epoxy resins. The shear stress was calculated based on apparent interlaminar shear strength standard [46] (ASTM D 2344 standard) where the shear stress is given by equation 14.

$$\tau = 0.75 \frac{P}{A} \quad (14)$$

In the figures, the specimens repaired with BECy that are tested at room temperature and 200 °C are represented as BECy-RT and BECy-200 respectively and the specimens repaired with Epoxy and tested at 200 °C are labeled as Epoxy-200. Even though the SBSB test is mainly developed for screening the flexural strength of bulk PMCs and to study mixed mode delamination mechanisms, the objective of the present work is to investigate the influence of BECy repair on the interlaminar shear strength of BMI-cf. From Figure 29a, the stress-strain curves of SBSB tests can be distinguished into two regimes that are separated by a maximum peak in shear stress.

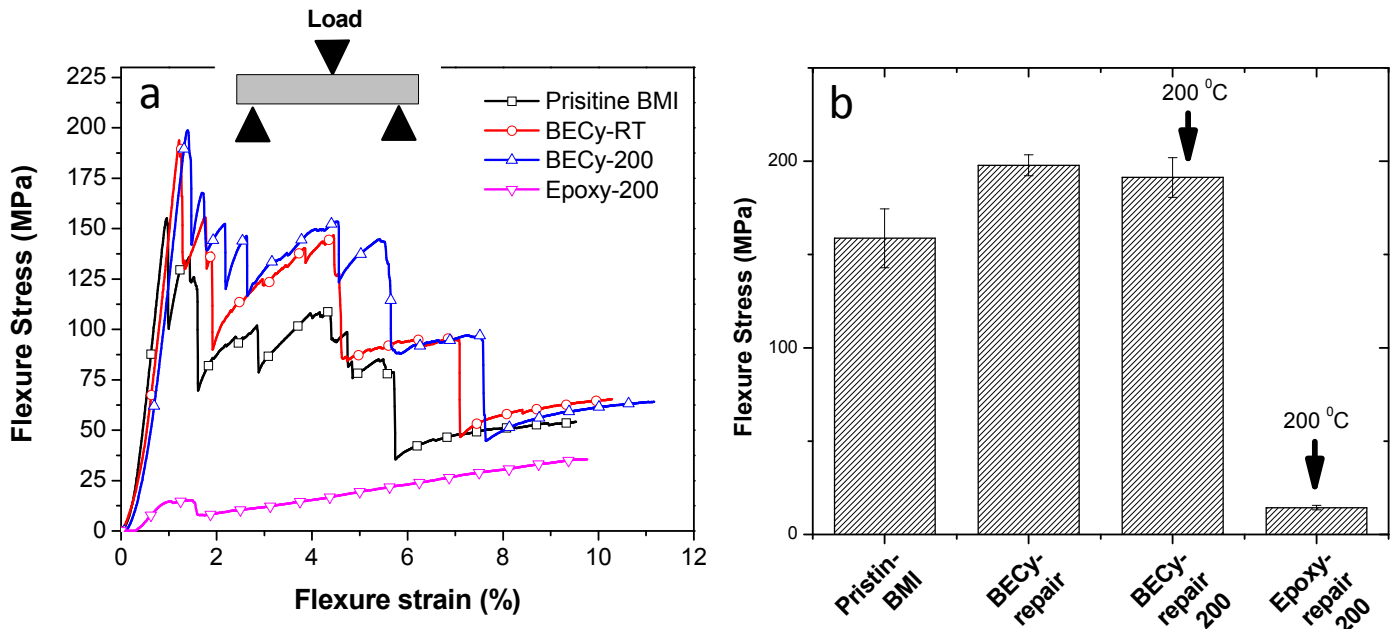


**Figure 29.** SBSB stress of BECy and Epoxy repaired specimens tested both at room temperature and 200 °C. (a) Stress-strain behavior of BMI-cf SBSB specimen (b) Average SBSB strength of investigated specimens.

In the linear regime i.e. in the pre-peak regime, the samples are expected to deform with fiber fragmentation in the central part of the beam followed by shear failure of the fiber matrix interface [64]. On the other hand the post-peak stress-strain behavior is attributed to the propagation of multiple cracks that are initiated at the center to the end of the beam.

In this regime a complete delamination process will take place in the sample with increase in the high flexural strains. We observed that an approximately 75 % drop in the maximum stress is required to delaminate the pristine BMI-cf SBSB sample into separate layers. A small amount of

BECy or Epoxy resin was used to manually rebind these layers to prepare repaired SBSB samples. The temperature of the delaminated BMI-cf SBSB sample layers was slightly raised above room temperature prior to repair, in order to provide better infiltration conditions for the BECy resin. This method of repair results in complete infiltration of the BECy resin between the laminated structures of the BMI-cf composite. The stress-strain curves in Figure 29a further illustrate the influence of repair resin and testing temperature on the flexural strength of the SBSB specimens. Since moisture content strongly effects the bonding effectiveness of BECy on BMI-cf substrates, the BMI-cf layers obtained after delamination were dried prior to the repair process. The maximum shear strength of pristine BMI-cf SBSB specimens increased from a virgin strength of ca. 150 MPa to a repaired strength of 200 MPa by repairing the delaminated plies with BECy. In addition, the strengths of the BECy repaired specimens tested at 200 °C were found to have similar strengths as samples tested at room temperature. This nearly 130 % repair efficiency indicates that damaged parts have the potential to be completely restored and with interlaminar shear strengths equal to or even exceeding those of the original structure.

The strength of SBSB specimens repaired with Epoxy was observed to be comparable to the strength of BECy when tested at room temperature (not included here). The high stress levels in BECy and Epoxy repaired specimens when compared to pristine samples can be attributed to high toughness of BECy and Epoxy when compared to BMI. However, Epoxy repaired specimens fail to show a significant shear stress-strain curve at high temperature (200 °C), the stress developed in the sample for complete delamination process is considerably low when compare to pristine and BECy repaired samples. The reason behind such low stress-strain behavior for Epoxy repaired system at 200 °C is due to the low glass transition temperature of the resin as observed in the lap shear tests. The stress-strain behavior of a completely delaminated sample was also tested and the stress-strain curves appear to be similar like Epoxy-200 (not shown here).

*DCB testing* - DCB testing is a widely used method for measuring the fracture toughness of adhesives and interlaminar toughness in PMC's [66- 69]. It is used to determine the critical Mode I (opening mode) strain-energy release rate ( $G_{IC}$ ) for a delaminated PMC under controlled displacement loading. In the present work, the DCB test is used to study the fracture toughness of BECy resin repair BMI-cf PMC. Figure 30a shows a typical load-displacement curve for a DCB test performed on a pristine BMI-cf specimen. The load is observed to increase linearly up to 60 N followed by an onset of non-linearity in the curve. The transition from linear to non-linear behavior is due to the initiation of crack growth from the Teflon film insert, followed by stick-slip crack growth behavior. In the DCB test the crack propagation behavior that starts after the onset of non-linearity has been characterized by three distinct natures [70,71], continuous or stable crack propagation, stick-slip or the unstable crack propagation and a hybrid behavior of both continuous and stick-slip crack propagations.

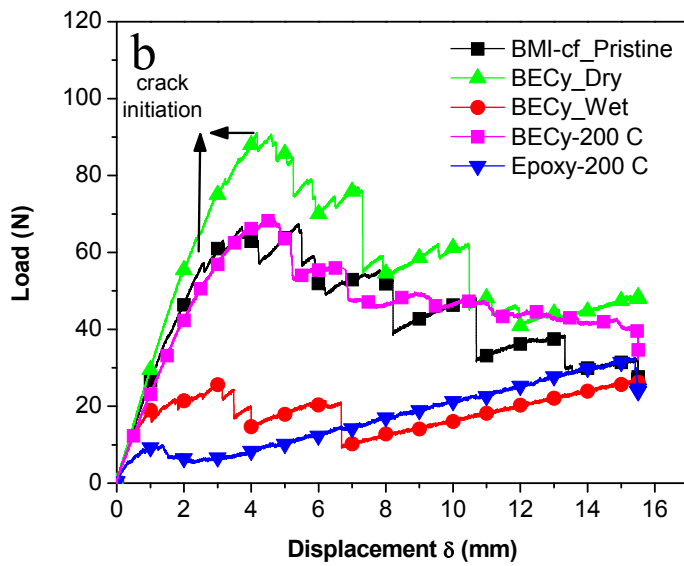
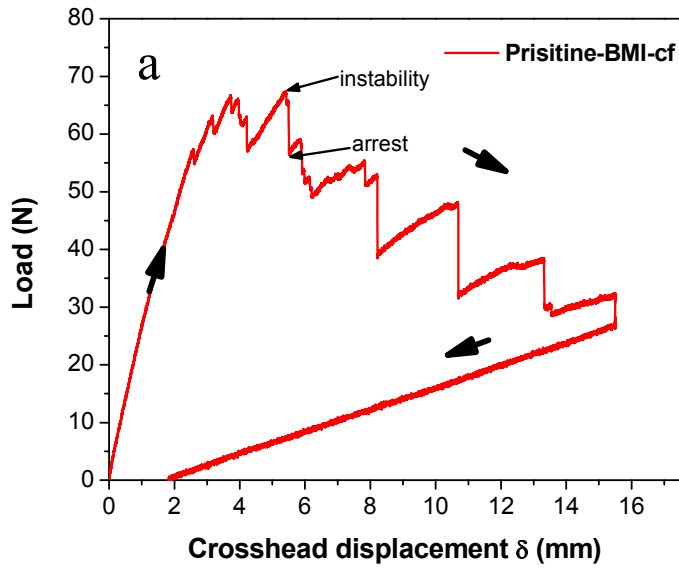


**Figure 30. (a) Typical load-displacement curve of a DCB specimen for BMI pristine sample. (b) DCB load-displacement curve for pristine specimen compared with the DCB specimens repaired with BECy and Epoxy.**

The load-displacement curve in Figure 30a can be correlated to stick-slip type crack propagation where the crack extension displacement increases due to crack initiation followed by crack arrest until it reaches a critical load for the next propagation step. The DCB load-displacement curves of pristine BMI-cf with BECy and Epoxy as crack filling resin in the DCB specimens is shown in Figure 30b. It can be observed that the DCB specimen repaired with BECy outperformed the pristine BMI-cf DCB specimen with a 50 % enhancement in the crack initiation load. It also displayed a high crosshead displacement for crack initiation. In addition to that, the overall load-displacement curve was observed to be well above the pristine specimen.

The DCB tests conducted with Epoxy resin showed a similar enhancement in the fracture strength (not shown in figure). Similar to lap shear and SBSB tests, the DCB tests were also conducted at high temperature (200 °C). In Figure 30b the load displacement curves of DCB tests with BECy and Epoxy resins tested at high temperature are represented as BECy-200 and Epoxy-200 respectively. Even though the load-displacement behavior of both these DCB specimens is similar at room temperature, a strong difference in their high temperature response can be seen in Figure 30b. BECy-200 shows higher load-displacement behavior than the pristine specimen, whereas Epoxy-200 repaired specimens are observed to be inferior to the pristine sample, clearly revealing the ability of BECy to provide enhanced bond strength while bonding the delaminated plies in BMI-cf PMCs during repair process. Figure 30a also illustrates the influence of moisture content in BMI-cf DCB specimens on the fracture strength. The fracture load for crack initiation and propagation for BECy on un-dried BMI-cf (BECy-wet) substrate was observed to be well below the fracture load for the pristine sample. The bubbling effect due to desorption of moisture content was again observed in un-dried DCB specimens that was observed previously in lap shear specimens.

*Crack resistance curves (R-curves)*- The crack resistance curves (R-curves) are constructed by synchronizing the load-displacement curves from DCB test with the crack extension images. R-curves in Figure 31 are constructed based on the modified beam theory (MTB) that is briefly described in the experimental section. Taking the average of crack resistance values for 4 to 6 specimens plots the R-curves shown in Figure 31. Except for BECy-wet and Epoxy-200, the R-curves of all the investigated specimens appear to have a similar curve profile for strain energy release rate ( $G_{IC}$ ) vs. crack extension. In the initial stage, i.e. at smaller crack extensions, the  $G_{IC}$  is strongly increases followed by a plateau like behavior. The strong increase in the  $G_{IC}$  value is mainly due to the fiber bridging between the crack plies near the crack initiation and development of damage zone around the crack tip [70]. The plateau region in the R-curves corresponds to the crack propagation through the specimen after crack initiation. Interestingly, it can be observed that the R-curve behavior of BECy-dry shows a high crack resistance when compared to the other DCB specimens at any given crack extension displacement. The high R-curve values for BECy-dry can be directly related to the capability of BECy to develop a strong interlaminar bond in the DCB specimens.

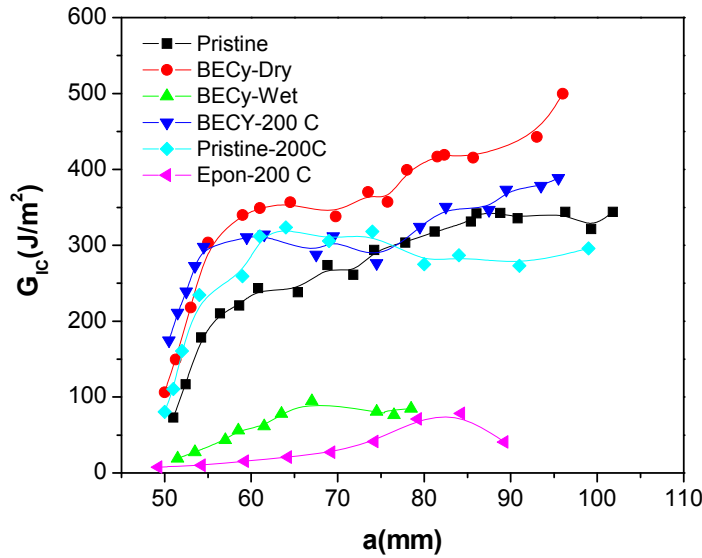


**Figure 31. R-curves for composites repaired with BECy and Epoxy resins tested at room temperature and 200 °C.**

The R-curves for BECy-dry specimen is increasing nominally with the crack propagation, which is not observed in other investigated samples including pristine BMI-cf specimen. The increasing trend in the R-curve values can be attributed to the increase in the fiber bridging process till the end of crack propagation. The high crack resistance even in the plateau region in BECy-dry could be due to the formation of stronger interfacial bond-line for fracturing the samples. In the crack initiation stage the R –curves of Pristine-200 DCB specimens tested at 200 °C shows high toughness than pristine DCB specimen tested at room temperature. The R-curve of Pristine-200 specimen show higher crack toughness than pristine sample at room temperature. However, the crack toughness of BECy-200 DCBspecimen is slightly below the R-curve of BECy-dry. The nominal decrease in the crack toughness in BECy-200 DCB specimen inspite of high-test temperature is still unclear and the investigations to study the influence of temperature on BECy repaired DCB specimens are still in process. In general BECy resin shows high resistance towards crack initiation and propagation at room temperature and at 200 °C when compared to the R-curves of pristine DCB specimen. The R-curves of Epoxy-200 and BECy-wet specimens appeared to be well below the pristine specimen and the R-curves are decreasing after extension of crack to above 75mm. The negative gradient in the R-curves implies spontaneous fracturing of sample after crack initiation. The spontaneous fracturing of DCB specimen is attributed to a weak interlaminar strength in Epoxy-200 and BECy-wet samples. In order to further study the fiber-matrix interaction that governs the interlaminar fracture toughness with respect to the nature of adhesive, the fractography studies are carry out using micrographs from the fracture surface in DCB tests and discussed in the next section.

*Fracture surface analysis* - The post-fracture surfaces of the DCB specimens were studied from SEM investigations. The variation in the fracture surface morphology due to the influence of moisture content, nature of resin and testing temperature can be seen in Figure 32. All the fracture surface micrographs were taken from the center of the specimen close to the



crack imitation zone. The high magnification images taken from a particular area of interest are attached to the right hand side of their corresponding micrographs. The fractured surfaces of pristine, BECy-wet repair, BECy-dry repair and Epoxy-200 are shown in Figure 32 (a-d) respectively. In the SEM micrographs of pristine BMI-cf DCB specimen the fracture surface appear to show some sights of fiber bridging. In high magnification images, it can be observed that as a result of fiber bridging, carbon fibers appear to be pulled out of the substrate, leaving bunches of finely broken carbon fibers that were protruding from the substrate. On repairing the DCB specimens with BECy-dry, i.e. in dried substrates (Figure 32c), the fracture surface appears to be a combination of pure substrate failure and adhesive-substrate interface failure. Sights of BECy resin along with the fiber bridging traces can be observed in the SEM micrographs. During the repair process of DCB specimens, the broken carbon fibers observed on the pristine fracture surface are expected to reinforce back into the composite substrate by forming a strong bond between the BMI-cf substrate and BECy.

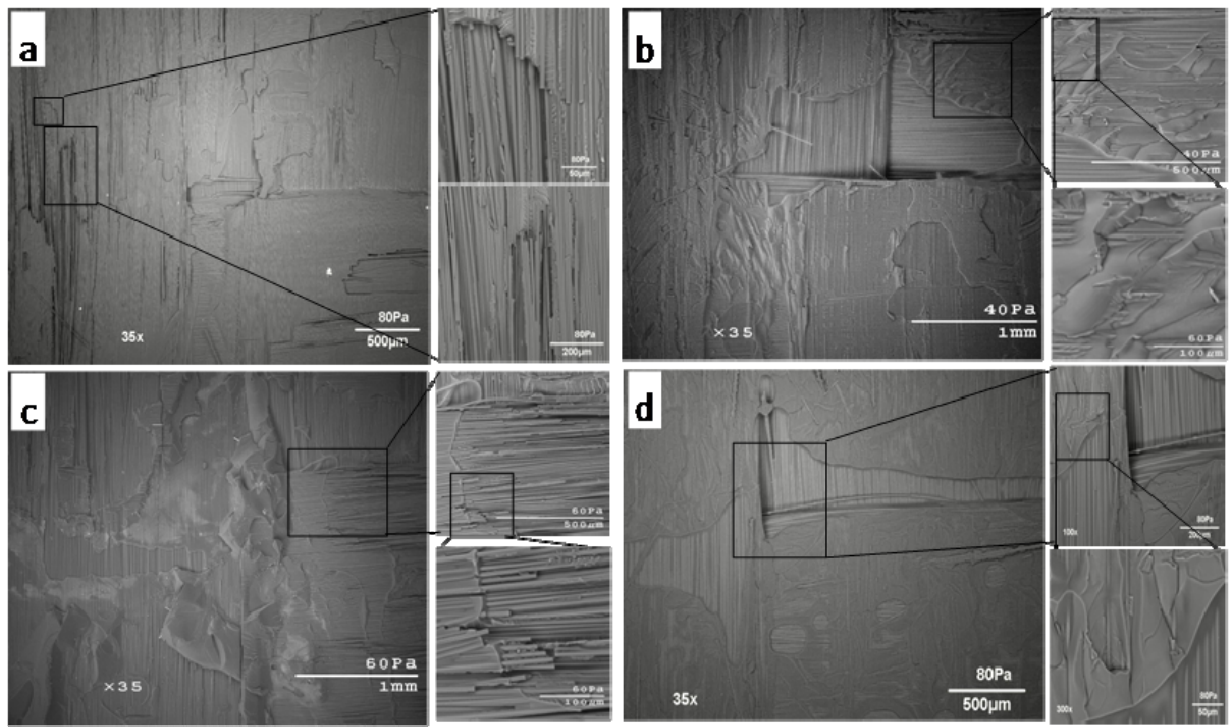


**Figure 32. SEM images of DCB fracture surfaces a) Pristine sample, b) Wet repaired sample, c) Dry repaired sample d) Epoxy repaired sample at 200 °C**

Such bond lines are expected to enhance the fracture resistance for BECy-dry repaired specimens. On the other hand BECy-wet and Epoxy-200 do not show any significant traces of fiber fragmentation on the fracture surface (Figure 32b and 32d). Instead, the SEM images appear to show more resin rich region. The absence of such fiber fragmentation sights is mainly due to poor interlaminar bond strength. The protruded carbon fibers that are pulled from the substrate during the delamination of pristine sample are expected to get reinforced into the substrate in both BECy-wet and Epoxy-200 while repairing the DCB specimen. However, as the crack resistance toughness of these specimens is consistently lower than pristine sample, fiber

pulling action cannot take place at such low stress levels. Therefore, the SEM investigation provides an interrelation between the efficiency of repair resin to the micromechanical behavior.

*Contact angle measurements-* The contact angle of BECy resin was measured on the BMI-cf substrate to determine the temperature with the best wettability for easy infiltration of BECy into the damaged PMC. The contact angle was measured between 30 - 130 °C with a 10 °C step increase in the temperature. In order to investigate the wettability of BECy on damaged surface of BMI-cf PMC, a 0.5 in x 0.5 in delaminated ply taken from BMI-cf PMC panel was taken as a substrate. Figure 33 illustrates the influence of temperature on the contact angle of BECy on a BMI-cf PMC substrate.

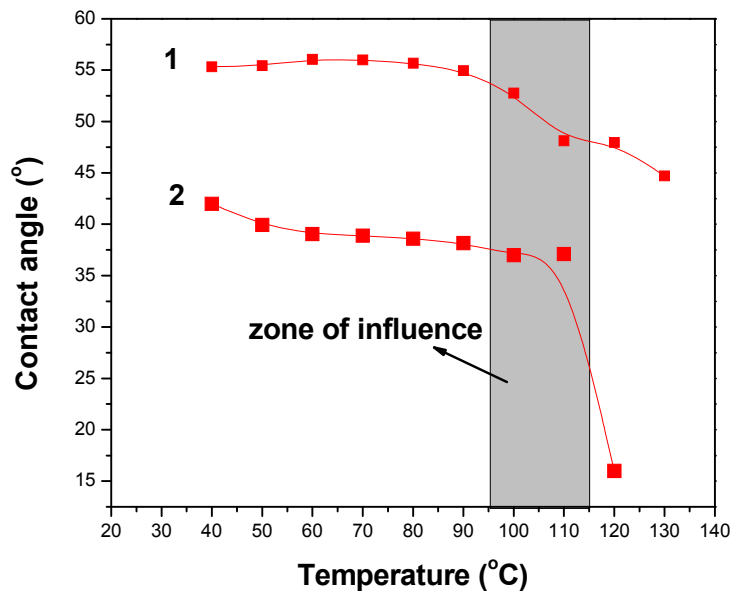


**Figure 33. Influence of temperature on the contact angle of BECy on BMI-cf substrate.**

The contact angle with respect to temperature was measured with two different BECy drop volumes. The variation in the contact angle between curve 1 and 2 in Figure 33 is due to that difference in the drop volume. The temperature for greatest wettability can be estimated from the significant drop in the contact angle above 95 °C. Therefore during the injection repair, the specimen temperature was maintained at 120 °C which is well above the influence temperature as indicated in Figure 33.

*C- Scan Images* - An air coupled ultrasonic imaging technique (C-Scan) with 120 kHz focused probes was used to create C-scan images of samples. This was used to illustrate the effective infiltration of the BECy repair system. The 4 in x 4 in pristine, damaged, and repaired hole plate shear (HPS) samples were scanned and the hole at the center was filled with putty to reduce air gaps which cause scattering in the scanned image. The pristine, delaminated, and repaired samples were scanned to exemplify the infiltration of the BECy resin under various repair conditions. The C-scan images of BMI-cf HPS specimens repaired at room temperature and 120 °C are shown in Figure 34. The delaminated C-scans confirmed the HPS method to be a

successful technique in introducing controlled and reproducible damage in the specimens. The infiltration of BECy into the damage zone was observed to be successful in the specimens repaired at 120 °C whereas only partial infiltration was observed for specimens repaired at room temperature.

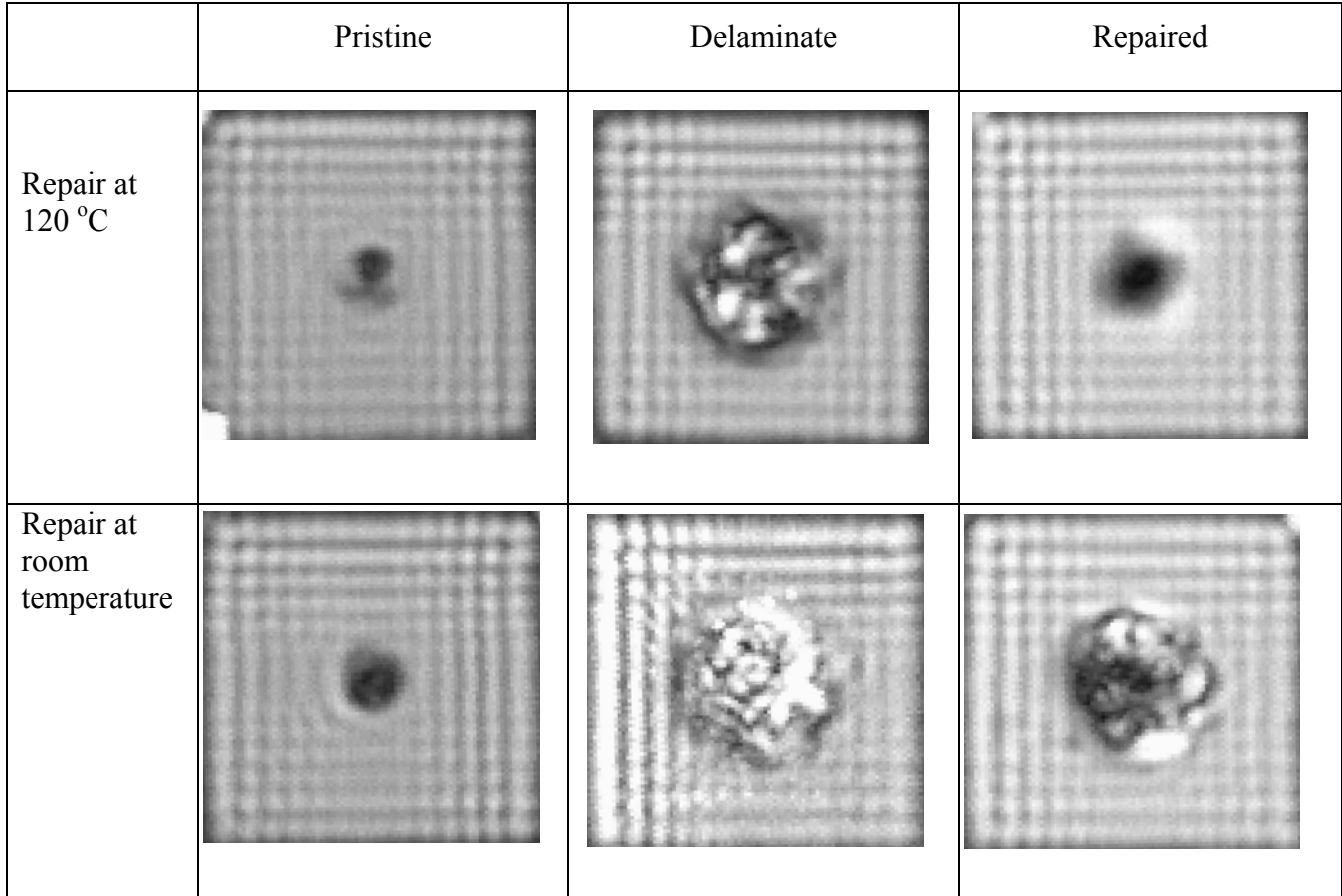


**Figure 34. C-scan images of BMI-cf HPS specimens repaired at room temperature and 120 °C**

*Florescent Dye Penetration (FDP) Testing* - For further verification of the infiltration of BECy resin a florescent Dye Penetration (FDP) Test was performed. The specimens were sectioned diagonally and examined via optical microscopy. The C-scan images of the pristine, delaminated and repaired specimens used for FDP test is shown in Figure 35. The cross section axis where the samples were cut is represented with the arrow line. The surface of the cross section was finely polished before taking the micrographs. An electron microscope was used to take pictures of the samples. For FDP test, the surface pictures were taken with the same electron microscope under ultraviolet (UV) light at 5x magnification causing the florescent dye to glow and clearly display the delaminations within the samples. This test visually showed the effectiveness of the infiltration of the BECy resin. The microscopic picture of one half of the cross section surface for pristine, delaminated and repaired specimens is shown in Figure 36. The presence of short cracks on the surface of pristine surface is due to the inherent cracks in the PMC formed as a result of air voids. In the delaminated specimen, traces of fine fragment cracks can be observed. Interestingly, the cracks occurred from the delamination and the inherent cracks

in the pristine specimen are completely absent in the repaired specimen. A successful infiltration of resin into the cracks was observed qualitatively from the FDP testing.

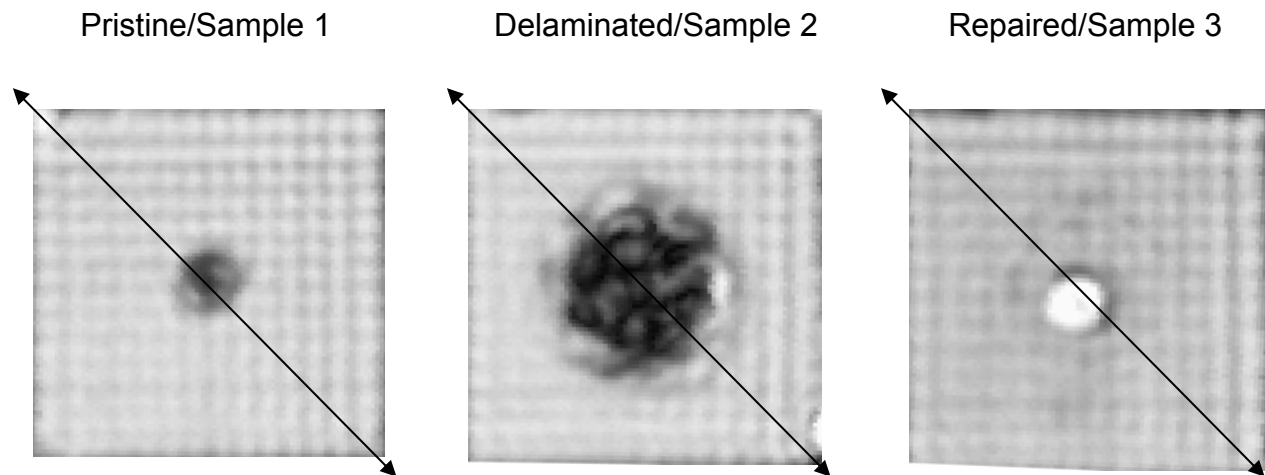


**Figure 35. C-scan images of specimens used for florescent dye Penetration (FDP) Test.**

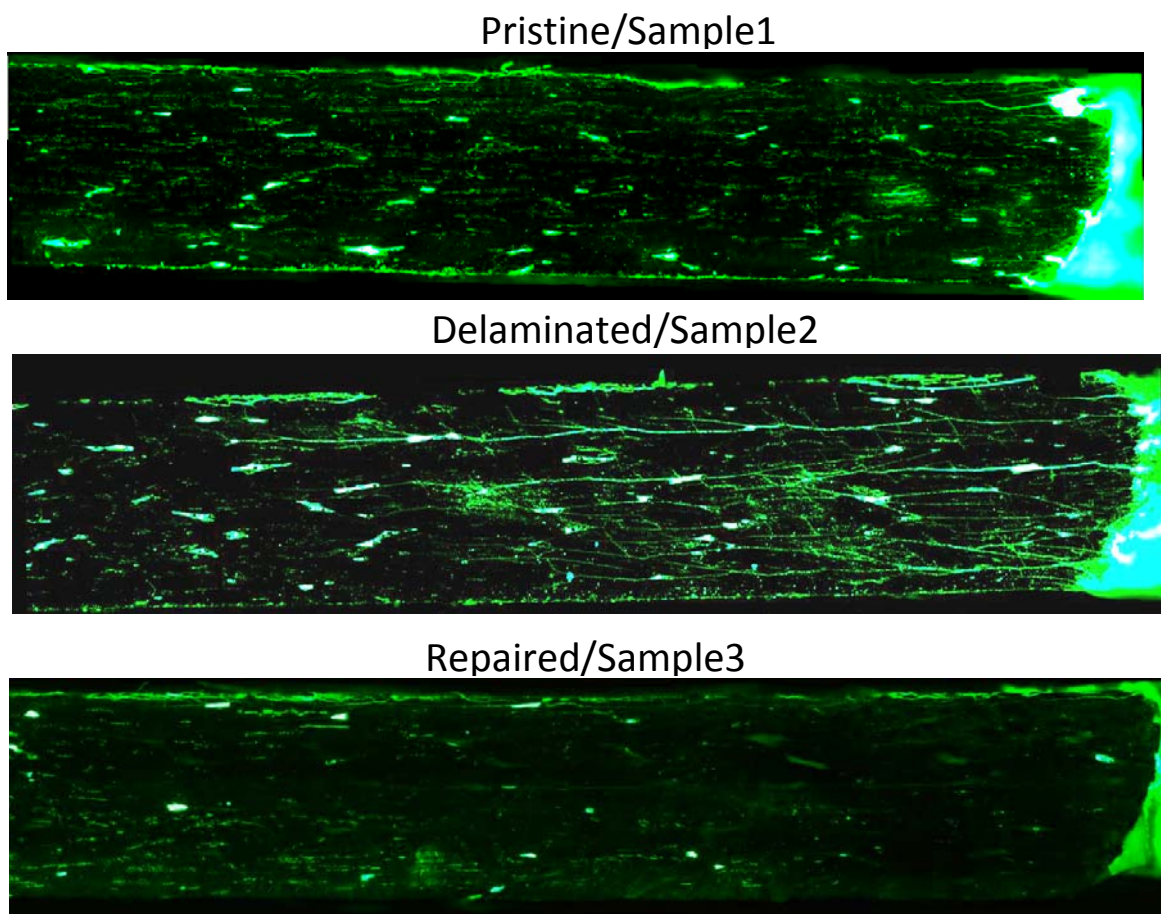


**Figure 36. Microscopic images of the transverse cross section view of BMI-cf specimens with traces of florescent dye Penetration (FDP) taken under ultraviolet.**

The FDP testing images were further used to quantify the effectiveness of the BECy infiltration. The crack paths in the pristine, delaminated and repaired samples were traced using Adobe Photoshop CS4 creating a skeleton of the cracks (Figure 37). These crack lengths were measured manually using a caliper. The total crack propagation per sample was determined and compared in Figure 38. The crack length measurements reveal the fact that, BECy is efficient in filling both the existing cracks in pristine specimen and delamination cracks from the damage specimen. While the C-scans and FCP tests confirm successful resin-infiltration into the microscopic cracks, the quality of the bond was evaluated by testing the mechanical strength of the HPS specimens. HPS test and compression after impact (CAI) tests were used to detect the strengths that are restored after repair.

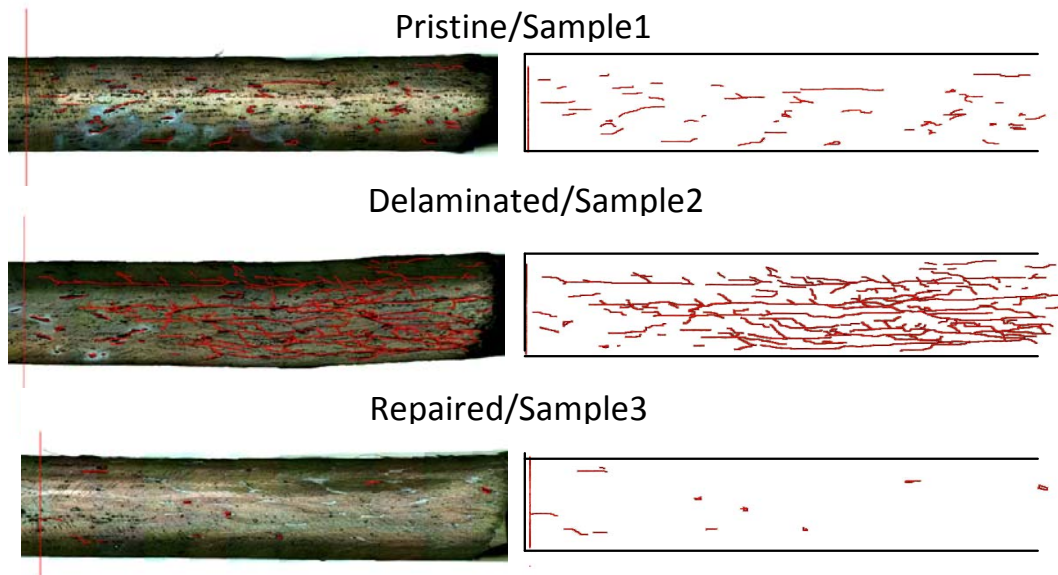


**Figure 37. Microscopic images of the transverse cross section view of BMI-cf specimens with traces of cracks on the left side and the skeleton of the crack lengths on the right side.**



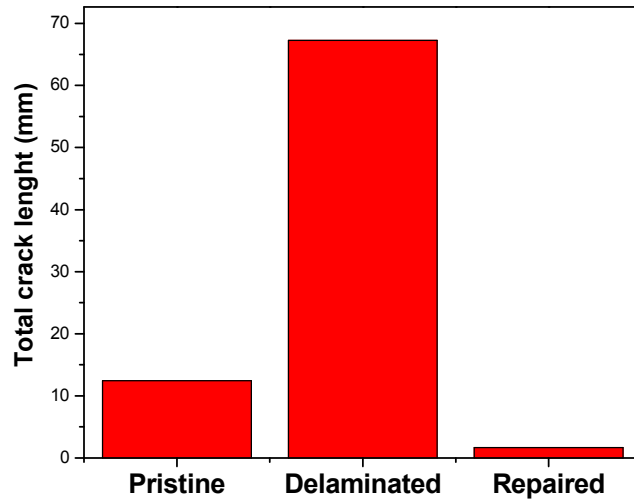


**Figure 38. Total crack length measured from the cross section surface of pristine, delaminated and repaired specimens.**

*HPS testing* - The load vs. compressive extension curves of pristine, delaminated and repaired specimens are shown in Figure 39. The load vs. compressive extension curves of pristine and repaired specimens demonstrate a peak load behavior followed by instabilities in the curves. The peak load behavior is due to the initiation of cracks in the specimen after reaching a critical load and the instability in the load values after crack initiation corresponds to the crack propagation. The average peak loads of investigated pristine and repaired specimens are summarized in Figure 40. The peak load for delaminated specimen is calculated by taking an average of load values exactly below the peaks of pristine specimen. The peak load and crack initiation extension are observed to be high in repaired specimens when compared to pristine specimens which reveals that, the load bearing capacity of BMI-cf PMC was enhanced after repairing with BECy. However, due to the absence of inter laminar bonding a peak load behavior can not be observed in delaminated specimens. The efficiency of repair was calculated via Equation 15,

where  $\sigma_{CAI}^{repair}$ ,  $\sigma_{CAI}^{delam}$ , and  $\sigma_{CAI}^{undamaged}$  are the peak loads of the repaired, delaminated, and pristine specimens, respectively. It can be observed that the repair was quite successful with 155% repair efficiency.

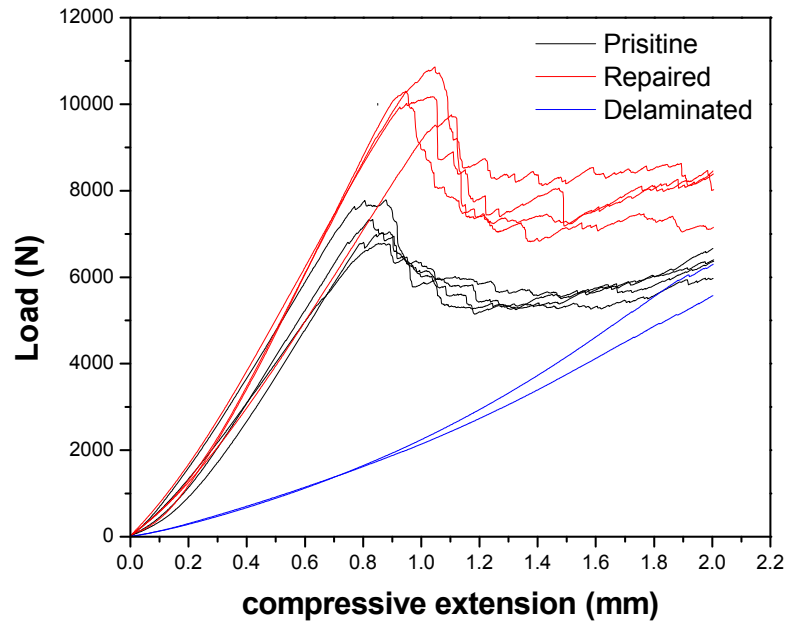


Figure 39. HPS testing on pristine, delaminated and repaired specimen.

$$E_{repair} = \frac{\sigma_{CAI}^{repair} - \sigma_{CAI}^{delam}}{\sigma_{CAI}^{undamaged} - \sigma_{CAI}^{delam}} \quad (15)$$

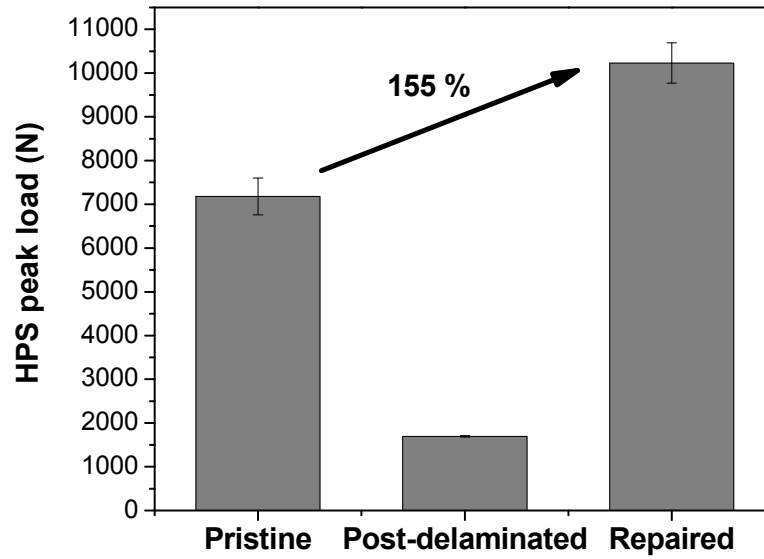
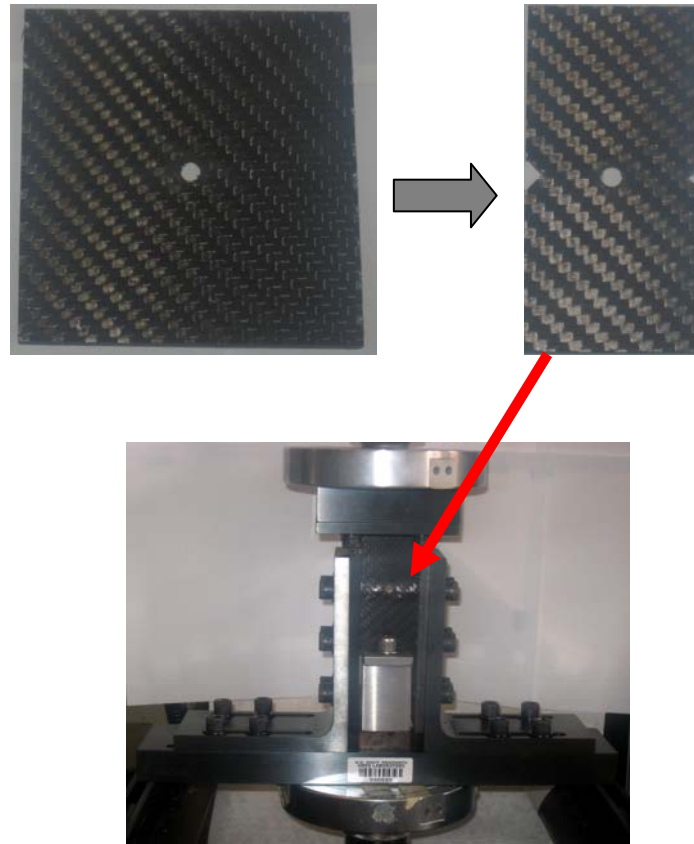


Figure 40. Maximum peak load of pristine, delaminated and repaired specimens in HPS testing.

*Compression after impact (CAI) testing* - CAI tests were conducted on pristine, delaminated and repaired specimens. The damage in the CAI specimens is created by using HPS method instead of impact load. As the delamination zone is constrained at the center in the HPS method, the geometry of the CAI specimens was altered to make the stress localized at the center. Hence, double-edge-notch (DENT) specimens were machined from the typical CAI samples.



**Figure 41. Experimental setup for CAI test with double-edge-notch (DENT) specimen.**

The DENT specimen along with the schema of CAI test is shown in Figure 41. The maximum stress required for fracturing the BMI-cf DENT specimen was recorded as a measure of strength of the specimen in in-plane direction. The CAI results of pristine, delaminated and repaired specimens are shown in Figure 42. A significant drop-off in the CAI stress can be observed in the delaminated specimens when compared to pristine specimens. However, in repaired specimens, the CAI strength was completely restored to the level of the pristine, undamaged composite, revealing 100 % repair efficiency.



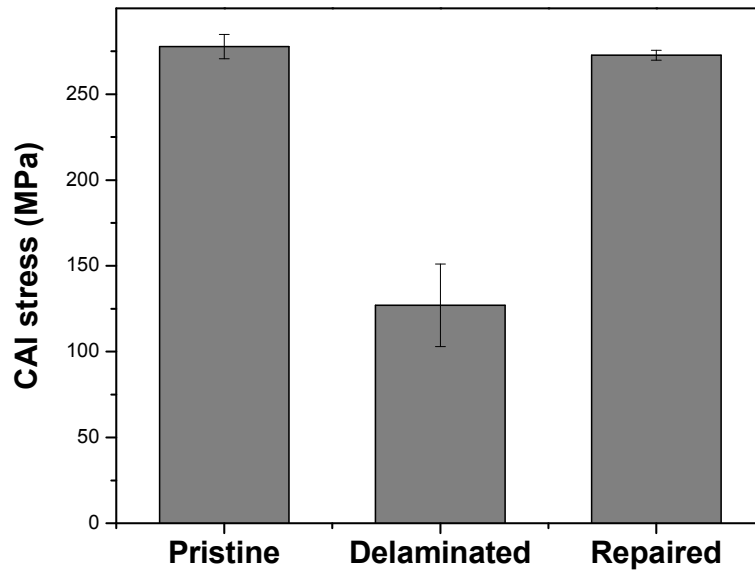


**Figure 42. CAI stress of pristine, delaminated and repaired specimens.**

*Repairing a structural BMI-cf PMC component-* A 254 x 254 mm BMI-cf PMC panel was fabricated which resembles the PMC component typically used in constructing complex structures in the aerospace industry. The composite panel was randomly damaged at different locations. The delamination areas were varied by increasing the extent of compressive extension in HPS method from 1 mm to 3 mm. The systematic increase in the delamination area was characterized qualitatively by air coupled through-transmission ultrasonic (C-scan) imaging. Figure 43a to Figure 43c illustrates the C-scan images of pristine, delaminated and repaired PMC panel. A systematic increase in the damage zone can be observed from the delaminated specimen. All three damage zones were repaired under similar processing conditions via vacuum based injection repair. The panel temperature was maintained at 120°C for most effective resin infiltration of the microscopic cracks. After repair the panel was rescanned for investigating the extent of resin infiltration in the delaminated zones. From Figure 43 c, a successful repair with complete resin infiltration can be observed.

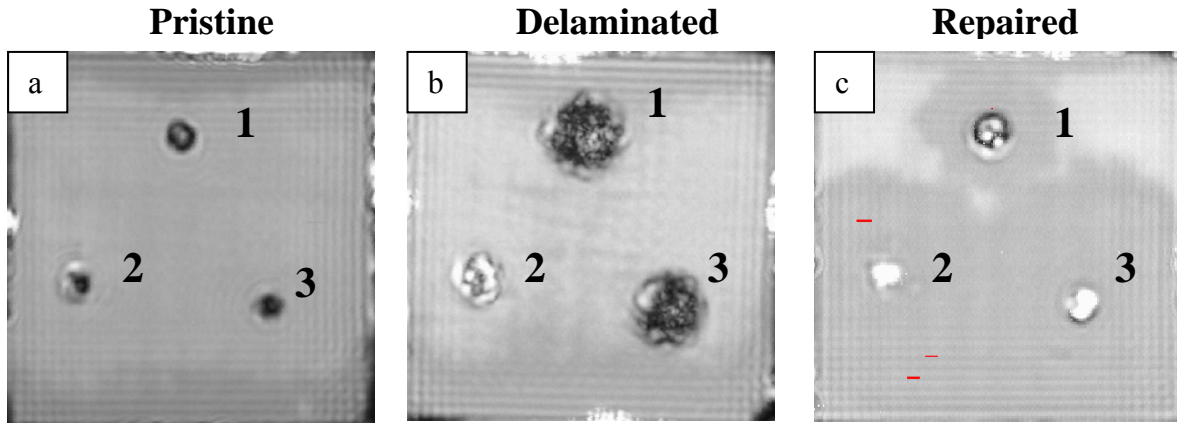


Figure 43. C-scan images of 10 in x 10 in BMI-cf PMC panel, a) Pristine, b) Delaminated, c) Repaired

The structural strength of the repaired panel was evaluated by conducting the HPS-after-HPS test on the repaired zones. Figure 44 depicts the results from HPS-after-HPS test is on the three repaired zones in comparison with the HPS test results of the pristine panel. The load vs. compressive extension curves obtained while delaminating the zones 1-3 are denoted as D1-D3 and the results from the repaired zones are named as R1-R3. By comparing D1 with R1, It can be confirmed that the repair was partially successful without complete recovery of the zone strength. However, zone-2 and 3 were observed to be successfully repaired (compare D2 with R2 and D3 with R3). More than 100 % recovery in the zone strength can be observed. The reason behind the partial recovery for the strength in zone-1 could be due to the influence of processing conditions. The repair of zones 1-3 were conducted on two different days, the environmental conditions could greatly affect the repair efficiency.

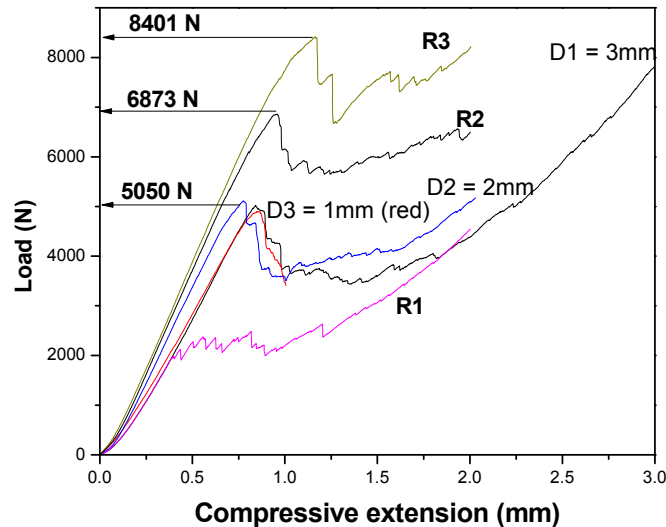


Figure 44. HPS test on the 254 x 254 mm BMI-cf PMC panel

## ***Cure Kinetics (nanoparticle filled BECy)- Results***

To compare the effects of alumina and silica nanoparticles, the samples were prepared at the same volume loadings since both the alumina and silica nanoparticles have same average particle size of 40 nm. The details of the composite compositions are listed in the table below:

**Table 5 Details of samples loading.**

Sample No.	Volume percent (%)	Alumina nanoparticles Weight percent (%)	Silica nanoparticles Weight percent (%)
1	0.16	0.5	0.3
2	0.7	2	1.2
3	1.6	5	3.0
4	3.2	10	5.8

The cure kinetics of uncured BECy/nanoparticle samples are evaluated from dynamic scanning experiments at multiple heating rates of 1, 2, 4 and 6°C/min. Figure 45 (a) shows the dynamic scanning curves of BECy/alumina nanoparticles, 10 wt.% sample. Compared to the catalyzed neat BECy sample, the peak of BECy/alumina nanoparticles is sharper and cover a narrower temperature region, which suggest the cure of uncatalyzed BECy/alumina follows different reaction mechanisms. To evaluate the effect of alumina nanoparticles, the dynamic scanning curves of BECy samples containing different loading of alumina are plotted in Figure 45(b). With increasing alumina nanoparticle loading, the peak position is shifted to lower temperatures: The BECy/alumina, 10 wt.% sample has a peak temperature of 187°C, which is 73°C lower than uncatalyzed neat BECy.

The BECy/alumina, 2 wt.% and 5 wt.% samples show two peaks on the dynamic scanning curves. Taking the peak temperatures separately and applying Kissinger's approach, the activation energy indicated by these peaks can be estimated. The analysis results are listed in Table 6. The 0.5 wt.% alumina/ BECy sample has one peak and an activation energy of 82.6 kJ/mol. Both peak temperature and activation energy are close to the values of the uncatalyzed neat BECy but slightly lower. The 2 wt.% and 5 wt.% samples show two peaks, therefore, there are two activation energies listed in the table:  $E_{a1}$  corresponds to the peak in the low temperature region (Peak 1) and  $E_{a2}$  corresponds to the peak in the high temperature region (Peak 2). The two separated activation energies indicate that different reaction mechanisms are involved during the dynamic scanning of uncatalyzed samples. As the loading of alumina nanoparticles increases from 2 wt.% to 5 wt.%, the peak height of Peak 2 decreases and Peak 1 increases, suggesting that the transition of reaction mechanism from one to another occurred due to the change of alumina nanoparticle loading. The 10 wt.% alumina/BECy sample shows only one peak with the same activation energy as the values estimated from Peak 1 of 2 wt.% to 5 wt.%.

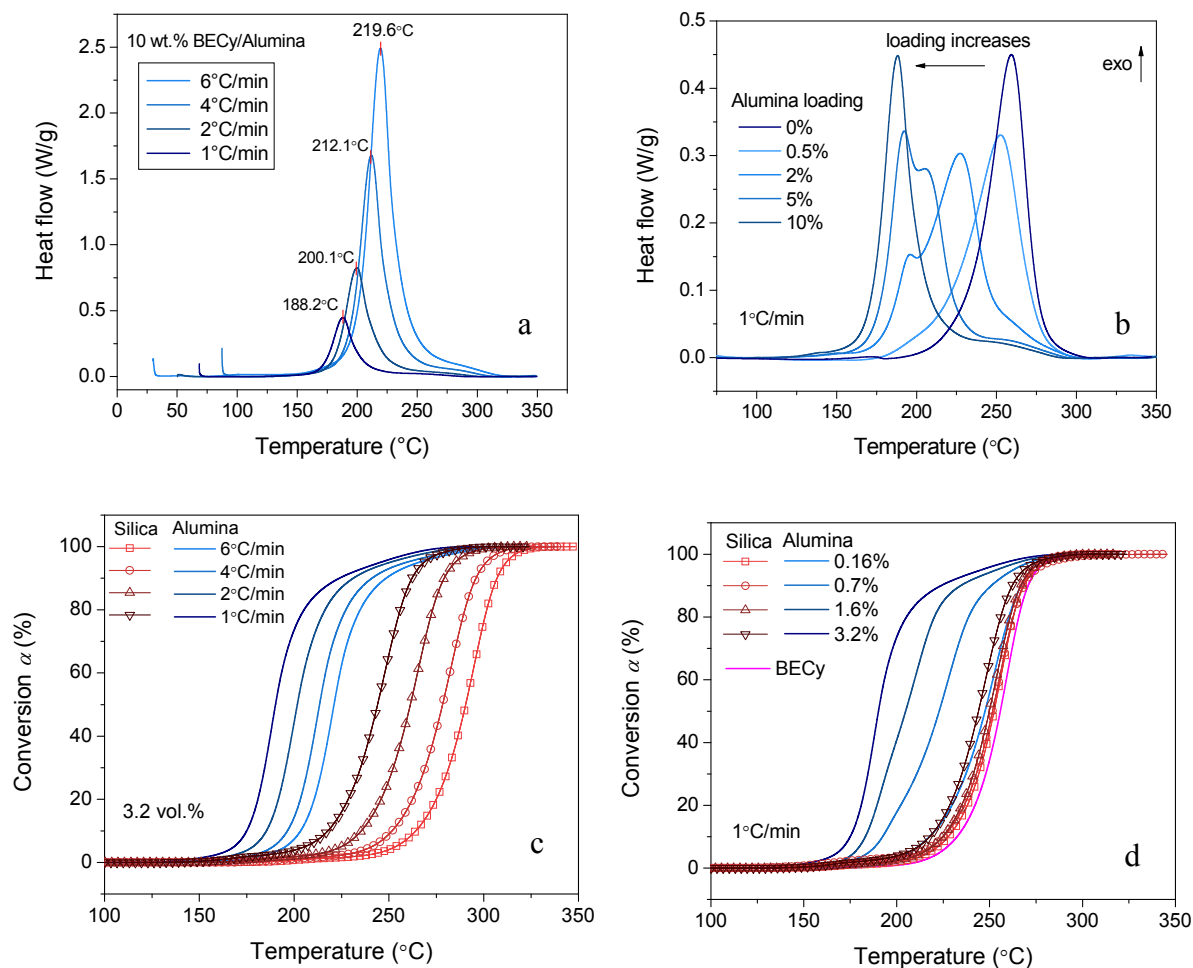


**Figure 45. Dynamic scanning of BECy contained nanoparticles: (a) dynamic scanning curves of BECy/alumina nanoparticles, 10wt.% sample; (b) Comparison of BECy/alumina nanoparticles sample with different loadings at 1°C/min; (c) the effects of alumina and silica nanoparticles on the cure of BECy, at same loading; (d) at same heating rate.**

**Table 6 Activation energy estimated from the separated peaks.**

Alumina loading (wt.%)	$E_{a1}$ (kJ/mol)	$E_{a2}$ (kJ/mol)
0		91.5
0.5		82.6
2	100.4	78.5
5	102.8	83.8
10	100.2	

The alumina nanoparticles affect the cure kinetics of BECy. The polymerization of BECy can be catalyzed by: (1) trace amount of phenol in monomer; (2) the surface hydroxyl group of alumina and physical absorbed water; or (3) Lewis acidity of  $\gamma$ -alumina. Since the amount of

phenol in BECy monomer does not change with the loading of alumina nanoparticles, the catalytic effect of alumina nanoparticles is likely contributed by the last two factors.

The silica nanoparticles with the same particle size as alumina nanoparticles contains similar levels of surface hydroxyl groups and physical absorbed water. Silica nanoparticles would have similar catalytic effects on the cure of BECy if factor (2) is the main reason for the catalysis. Uncatalyzed BECy/silica nanoparticle samples were prepared at the same volume loadings as the BECy/alumina nanoparticle samples, and then evaluated with DSC in dynamic temperature scans. The results are shown in Figure 45 (c) and (d). At the same loading (3.2 vol.%, 10 wt.% for alumina nanoparticles), the samples containing alumina nanoparticles start to polymerize at much lower temperatures than the ones containing silica nanoparticles. At the same heating rate, with increasing nanoparticle loading, the sample containing alumina nanoparticles reaches the same level of cure at a lower temperature: 0.16 vol.% sample at 247°C and 3.2 vol.% sample at 190°C reaches to the same monomer conversion of 50%. Compared to the BECy/alumina samples, the samples containing silica nanoparticles do not show these pronounced changes.

Therefore, the catalytic effect of alumina nanoparticles is believed to be mainly a result of the Lewis acidity of  $\gamma$ -alumina, which is a unique character of the alumina nanoparticles. The addition of alumina nanoparticles introduces different reaction mechanisms. Investigation of these catalytic effects of the alumina nanoparticles is in progress.

### ***Functionalization of alumina nanoparticles- Results***

The amount of immobilized silane on the surface of alumina nanoparticles was measured by TG (Figure 46) The mass loss below 250°C is due to the physical absorbed water. Above 250°C, the mass loss is mainly due to hydrolysis of surface hydroxide groups for bare alumina nanoparticles and decomposition of surface silanes for functionalized alumina nanoparticles. Dried alumina nanoparticles contain less physical absorbed water than as-received ones and show less mass loss (0.3%) below 250°C. Compare to the as-received alumina nanoparticles, GPS and APS functionalized alumina nanoparticles show less physical absorbed water and more total mass loss at 800°C. The increased mass loss corresponds to the amount of silane immobilized on the surface of the nanoparticles. Based on the graft density of 0.5 molecules per square nanometer, the estimated amount of immobilized GPS is around 0.8% of the total mass. The TG results show immobilized silane is more than 1% of the total mass for GPS and APS, indicating that the actual graft density of GPS and APS is higher than the assumed value, or the hydrolysis reaction occurred between the silane molecules rather than with the surface hydroxyl group because both GPS and APS silane contain three ethyloxyl, methyloxyl groups on each molecule, respectively. OS has only one chloride function group, which can hydrolyze with the surface hydroxyl group. At each immobilization site (-OH), only one OS molecule can be attached. The OS functionalized alumina nanoparticles show only 0.3% more mass loss than bare alumina particles, which is less than the expected value.

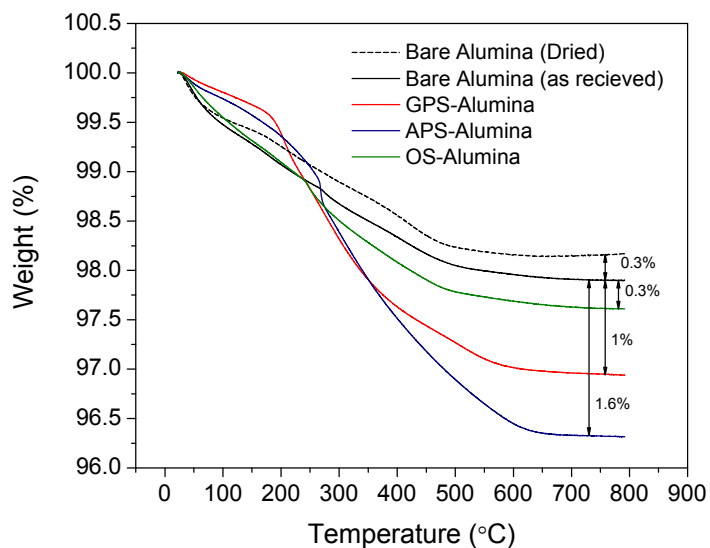


**Figure 46. TG results of functionalized alulmina nanoparticles.**

APS functionalized alumina nanoparticles are also characterized by FT-IR. The FT-IR spectrum is shown in Figure 47. The peak at  $2929\text{ cm}^{-1}$  is characteristic of the peak of  $\text{-NH}$  and suggests that the alumina nanoparticles are functionalized with APS successfully.

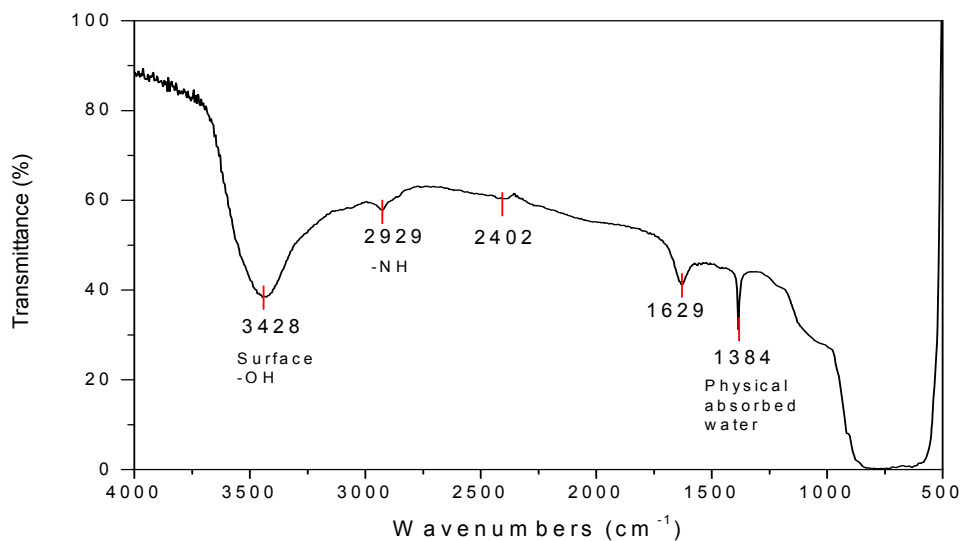


**Figure 47. FT-IR spectrum of APS functionalized alumina nanoparticles.**

A simple dispersion test was performed and is shown in Figure 48. The same amount of functionalized alumina nanoparticles and bare nanoparticles were dispersed in the solvents with

different polarities (Polarity of solvent: methylene chloride < THF < Methanol) and then allowed to settle for 5 hrs.

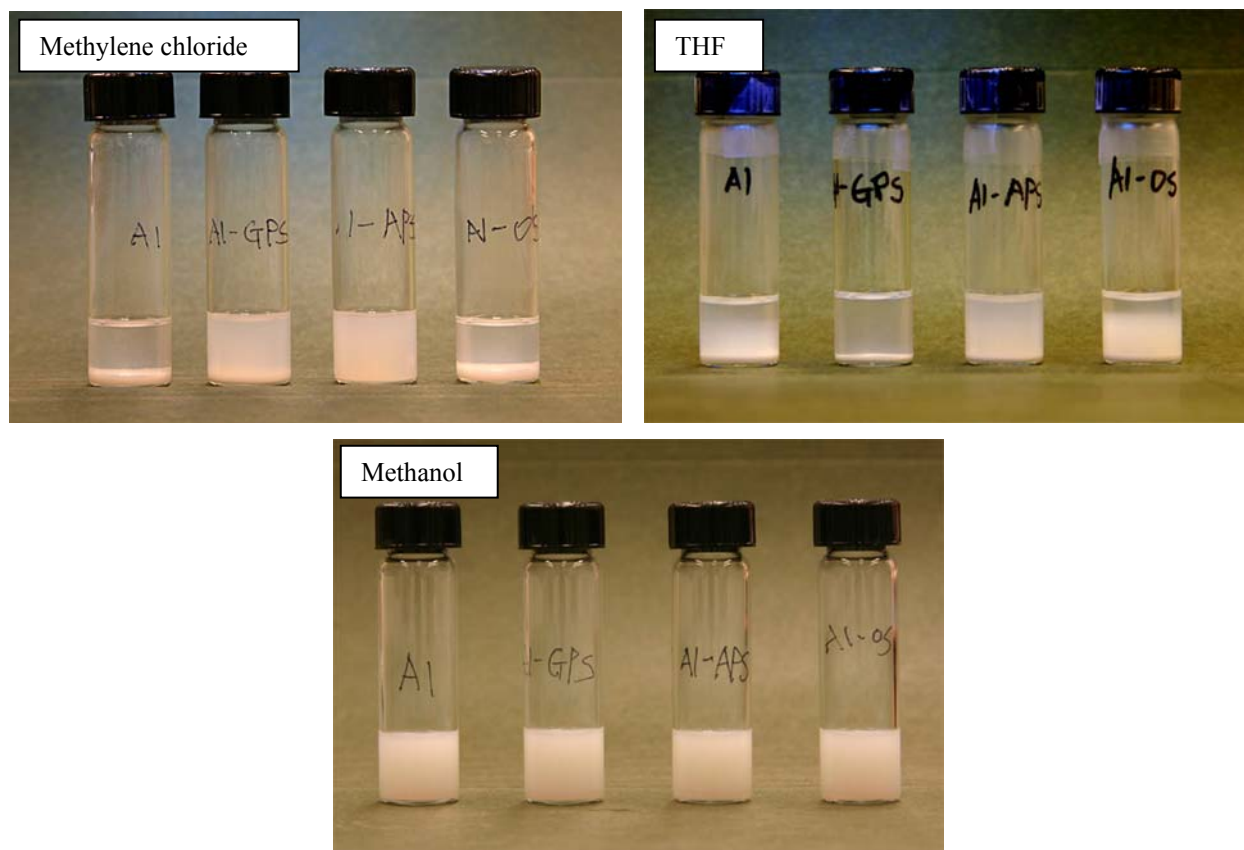


**Figure 48. Dispersion test in methylene chloride, THF, methanol.**

The surface hydroxyl groups of the alumina nanoparticles has very strong polarity, which make alumina nanoparticles easy to precipitate in non-polar methylene chloride, partially precipitate in THF and remain very stable in polar methanol even after 5 hrs. Alumina nanoparticles were successfully functionalized with GPS and APS, making the alumina nanoparticles' surface less polar. Therefore, GPS and APS functionalized nanoparticles dispersed better than bare alumina nanoparticles in methylene chloride and are easy to precipitate in THF. Both GPS and APS functionalized nanoparticles still contained a large amount of surface hydroxyl group, which has strong interaction with polar solvent and overcomes the effect of less polar surface silane groups, and are stable in methanol. OS functionalized alumina nanoparticles should be less polar than other the three kinds of nanoparticles and dispersed very well in methylene chloride. But in the dispersion test, OS functionalized alumina nanoparticles do not show a difference from bare alumina nanoparticles. The functionalization of alumina nanoparticles with OS was not successful, which confirms the TG results.

Other silanes, such as triethoxy(octyl)silane, are in consideration to replace OS. For GPS and APS, the experiment conditions will be optimized to increase the amount of surface functional groups. The further characterization of functionalized alumina nanoparticles is in progress.

## Rheology of nanoparticle/cyanate ester suspensions-Results

**Suspension rheology**—Figure 49 and Figure 50 show viscosity vs. shear rate data (0.1 to 100 s<sup>-1</sup>) for uncatalyzed BECy/silica suspensions at room temperature, for 12 and 40 nm particles, respectively. For the shear rate range from 0.1 to 10 s<sup>-1</sup>, all BECy/silica compositions show pseudo-plastic or “shear thinning” behavior, characteristic of an apparent decrease in viscosity with shear rate, while the neat BECy resin exhibits near Newtonian flow. Figure 51 and Figure 52 show the viscosity data on a log-normal scale for this range (0.1 to 10 s<sup>-1</sup>) only. The pseudo-plastic behavior is amplified with increasing silica content. Additionally, viscosity is higher and the shear thinning is most pronounced for the 12 nm silica, which have higher surface area.

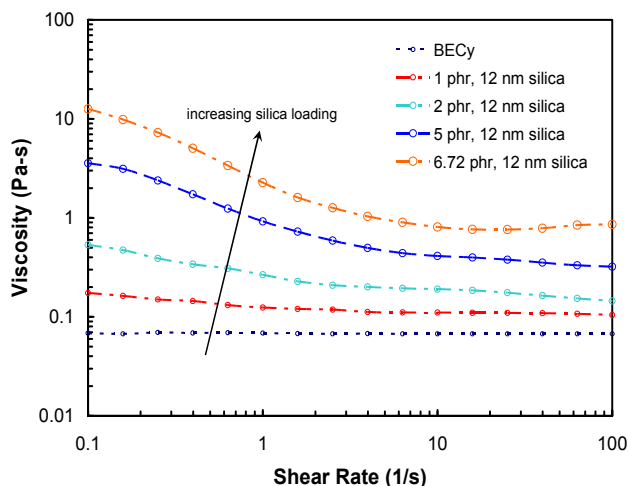


Figure 49. Viscosity vs. shear rate for 12 nm fumed silica suspensions (0.1 to 100 s<sup>-1</sup>).

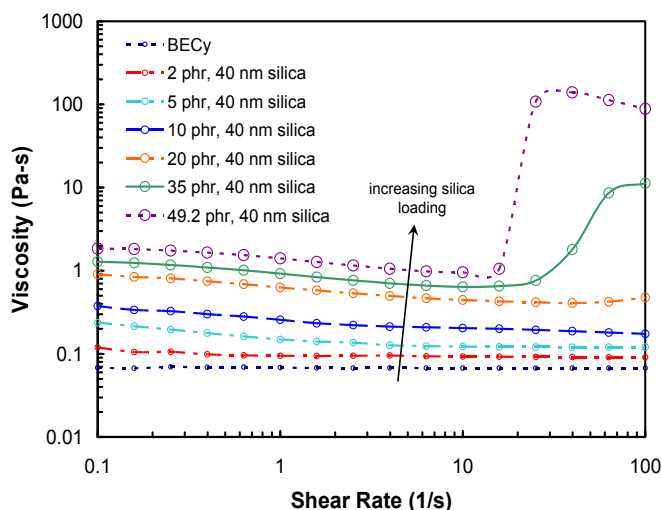


Figure 50 Viscosity vs. shear rate for 40 nm fumed silica suspensions (0.1 to 100 s<sup>-1</sup>).



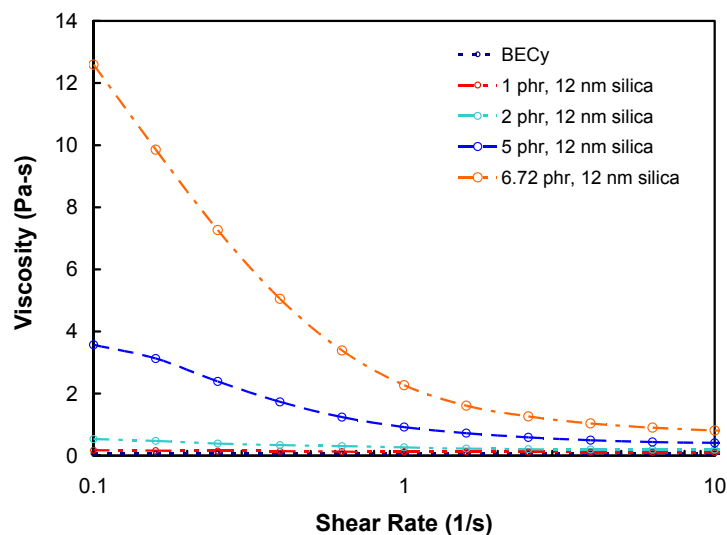


Figure 51. Viscosity vs. shear rate for 12 nm suspensions (log-normal,  $< 10 \text{ s}^{-1}$ ).

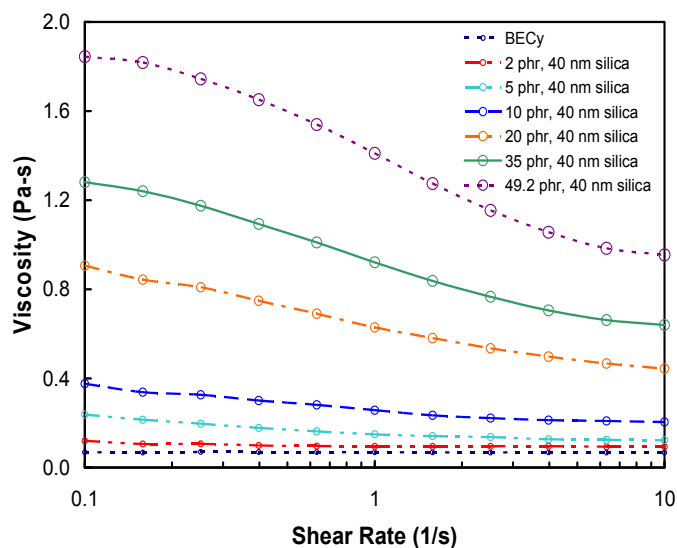
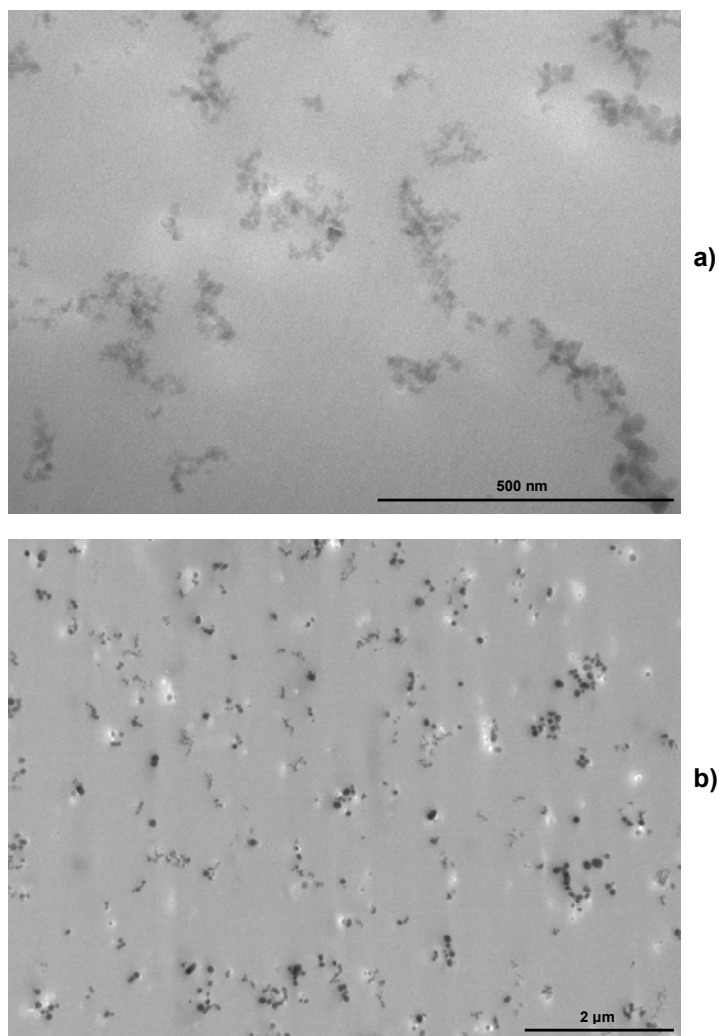


Figure 52. Viscosity vs. shear rate for 40 nm suspensions (log-normal,  $< 10 \text{ s}^{-1}$ ).

The primary mechanism for the pseudo-plastic or shear thinning nature of hydrophilic fumed silica suspensions is well-known, and is attributed to the formation of hydrogen bonds between hydroxyl groups of neighboring particles [72]. The hydrogen bonds form under low shear and are broken under high applied shear. The effect is most pronounced for weakly hydrogen-bonding liquids, which do not form as many bonds at the particle-liquid interface. This allows a complete network of hydrogen-bonds to be formed between particles, resulting in a gel. For strongly hydrogen-bonding liquids, a stable sol is formed because of the interference of the liquid in the formation of a complete network of hydrogen-bonds between particles [72]. The polar cyanate groups in the BECy monomer should have an affinity to the hydroxyl groups of the silica, which would disrupt the formation of a complete network between the silica particles. In fact, other work on cyanate ester nanocomposites has shown that hydrogen bonding can occur between the hydroxyl and cyanate groups of silica and cyanate esters, respectively.

Another factor may be at work in the rheological behavior of these suspensions: physical entanglement and agglomeration of fumed silica particles and aggregates. TEM analysis of cured nanocomposites showed that the 12 nm silica had a greater degree of agglomeration than the 40 nm silica. The agglomeration of the silica aggregates would create pockets of immobilized and/or trapped monomer, which raise the effective volume fraction of fumed silica [73]. Similar observations by Li and Akinc were noted for nano-alumina dispersions in water [74]. The larger tendency of the 12 nm silica to agglomerate would explain the higher viscosity of these suspensions compared to the 40 nm silica suspensions of the same volume fraction. This mechanism could also be responsible for shear thinning because the shearing of the suspensions would help to break up the agglomerates, decreasing the effective volume fraction and thus the viscosity of the suspension [73].

In the highest volume fractions of the 40 nm silica nanocomposites (49.2 phr or 20.7 vol% and 35 phr or 15.6 vol%), a shear thickening effect was observed above  $10 \text{ s}^{-1}$ , which raises the apparent viscosity of the suspensions by as much as two orders of magnitude (see Figure 50). There is also a very slight increase in viscosity above  $20 \text{ s}^{-1}$  in the highest volume fraction of the 12 nm silica (6.72 phr or 3.44 vol%), but the magnitude of this change is much less and may not be significant. According to the literature, there are two conditions that must be satisfied for shear thickening to occur in suspensions: 1) the volume fraction of the filler must be very high, and 2) the suspension must be “nonfloculated” (free of agglomeration) [75]. The shear thickening of a suspension is attributed to the formation of particle clusters that raise the effective volume fraction of the suspension [75], a mechanism that is brought about at a critical shear stress where particles that were kept apart at low stresses are driven together at high stresses [76]. For more polar liquids with fumed silica, the shear thickening mechanism is more pronounced because of hydrogen-bonding between the liquid and silica, which reduces agglomeration [75]. For fumed silica particles in BECy, 40 nm silica particles show a lower degree of agglomeration compared to the 12 nm (see Figure 53). This phenomenon may also be due in part to the fact that the aggregates of fumed silica would have a higher probability of entanglement at high shear than perfectly spherical particles of the same size. Raghavan and Khan reported shear thickening for 14 nm fumed silica suspensions in propylene glycol for loadings of only 3 to 10 wt%, but work by Bender and Wagner [77] and Lee and Wagner [78] on colloidal suspensions of spherical silica showed shear thickening only for compositions exceeding 50 vol%.



**Figure 53. Fumed silica (5 phr, 2.58 vol%) in polymerized BECy matrix, a) 12 nm silica, b) 40 nm silica.**

A standard way to compare levels of pseudoplasticity in fumed silica suspensions is to calculate the shear thinning index (STI) of the suspension by dividing the viscosity at a low shear rate by the viscosity at a high shear rate [73]. In Table 1, the STI's are tabulated for the 12 and 40 nm fumed silica suspensions, comparing the viscosities at 1 and 10  $\text{s}^{-1}$ .

The STI's for the 12 nm silica suspensions are higher than that of the 40 nm silica suspensions. In fact, the STI for 2 phr of 12 nm is about the same at 20 phr of 40 nm silica. It can be concluded that the 12 nm silica nanocomposites exhibit greater degrees of pseudoplasticity for equal volume fractions.

Further testing of the fumed silica suspensions showed thixotropic behavior. Thixotropy is a rheological term that literally means, "sensitive to touching" [79]. Thixotropy implies shear thinning (although shear thinning does not imply thixotropy). Unlike time-independent non-Newtonian behavior, however, thixotropy is a transient property, such that changes do not occur instantaneously but over time [79]. In our systems, we observed decreases in viscosity over time with applied shear, as well as increases in viscosity over time with little or no applied shear.

In general, the characterization of thixotropy is difficult due to the many factors that affect its behavior, such as 1) shear history, 2) dispersion state, 3) temperature, and 4) age of suspension [73]. Attempts were made to fully characterize the changes in thixotropy recovery with volume fraction and particle size using transient test methods, but the results were somewhat unpredictable due to the large number of factors that affect the thixotropic behavior of fumed silica suspensions. To qualitatively illustrate some of our observations, Figure 54 shows the results of thixotropy recovery tests on highly loaded BECy/silica suspensions. The suspensions were monitored with time for changes in viscosity and viscoelastic properties using periodic dynamic oscillation (0.1 Hz) at a very low stress (0.1 Pa), immediately following an initial pre-shear of  $100 \text{ s}^{-1}$  for one minute.

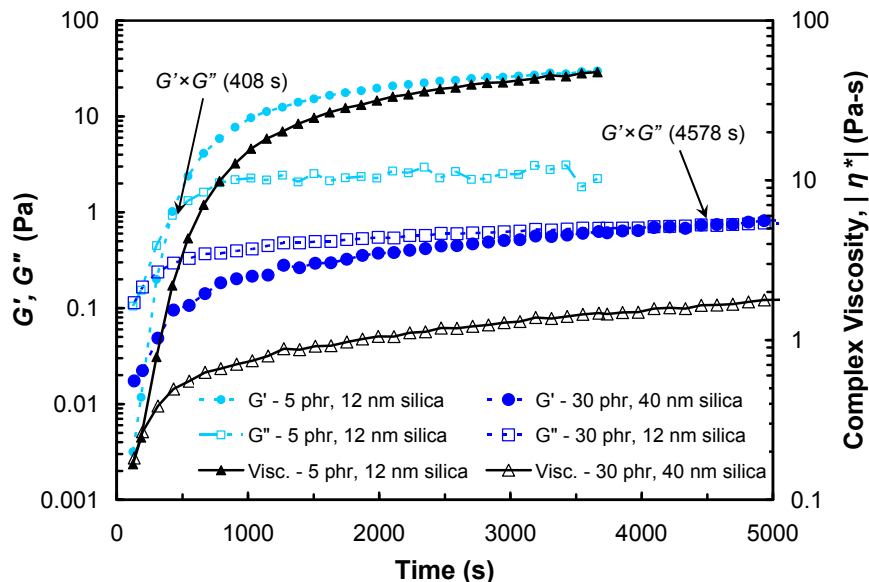


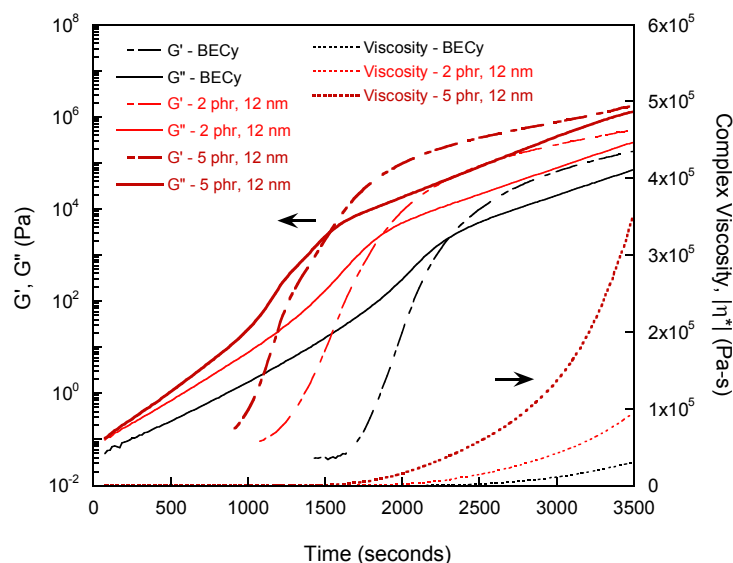
**Figure 54. Thixotropy recovery as a function of time (0.1 Pa, data taken at 2 min intervals).**

The shear storage modulus,  $G'$ , represents the elastic component of the response, the shear loss modulus,  $G''$ , represents the viscous component, and the viscosity is the dynamic viscosity (also called complex viscosity,  $|\eta^*|$ ). For the 12 nm sample at a loading of 5 phr (2.58 vol%), the complex viscosity increases quickly after the initial pre-shear, and  $G'$  is equal to  $G''$  at 408 s (or 6.8 min). The  $G' \times G''$  point is loosely defined as the gel point, indicating that a network has formed and the material's response is dominated by elastic behavior. The complex viscosity and elastic component continue to rise, and after one hour, the viscosity has reached about 48 Pa-s. For a much higher loading (30 phr or 13.7 vol%) of the 40 nm silica, the rise in complex viscosity is much less pronounced. After two hours, the viscosity increased only from about 0.17 Pa-s to 1.79 Pa-s. There is a weak crossover between  $G'$  and  $G''$ , indicating the presence of a gel, but it takes 76.3 minutes (4578 s) for this to occur. According to the literature on fumed silica in non-polar liquids, a suspension should gel within 30 to 120 seconds for the fumed silica to be completely effective as a rheology control agent (raise viscosity substantially, eliminate sag, and control settling) [39]. For the BECy/silica suspensions, the thixotropy recovery phenomenon is slower. This is due to hydrogen-bonding between the polar BECy monomer and fumed silica, which will lessen the thixotropic effect, as seen in other polar liquids [72]. However, since some concentrations of the suspensions eventually form gels, it is possible that some hydrogen-

bonding is occurring between the fumed silica aggregates, especially for the 12 nm silica, which has a faster gel time and greater level of thixotropy than the 40 nm silica in BECy monomer.

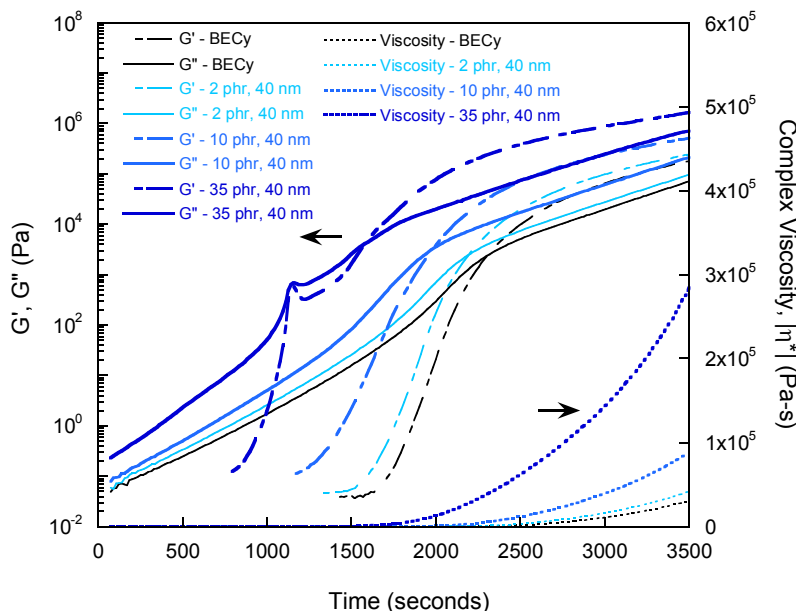
However, the thixotropy recovery may be due to formation of agglomerates, not hydrogen-bonding, or it may be a combination of the two. At rest, the dispersed silica will agglomerate over time, leading to immobilized monomer, which may contribute to recovery by raising the effective volume fraction, and thus viscosity. This is the primary mechanism for thixotropy in treated (hydrophobic) fumed silica, which does not hydrogen-bond [73], but may be appropriate in the present study because of the polar nature of the BECy monomer used. However, it is not possible to differentiate between these two mechanisms within the limited scope of the present study because of the complexity of the interactions between the particles, aggregates, agglomerates, and monomer.

**Rheokinetic evaluation**—Dynamic oscillatory rheology was used to monitor changes in the rheological properties of catalyzed cyanate ester nanocomposites during isothermal cure. Here, we refer to this as “rheokinetic evaluation,” but it can also be termed “chemorheology” [80]. Figure 55 shows dynamic mechanical properties of the catalyzed 12 nm fumed silica/BECy suspensions as they cure at an isotherm of 130 °C. The gelation point was taken at the point where  $G'$  is equal to  $G''$  ( $G' \times G''$  crossover), which is representative of the point where the prepolymer forms a crosslinked network [81,82] and the macroscopic response of the material is viscoelastic, dominated by an elastic behavior [80].



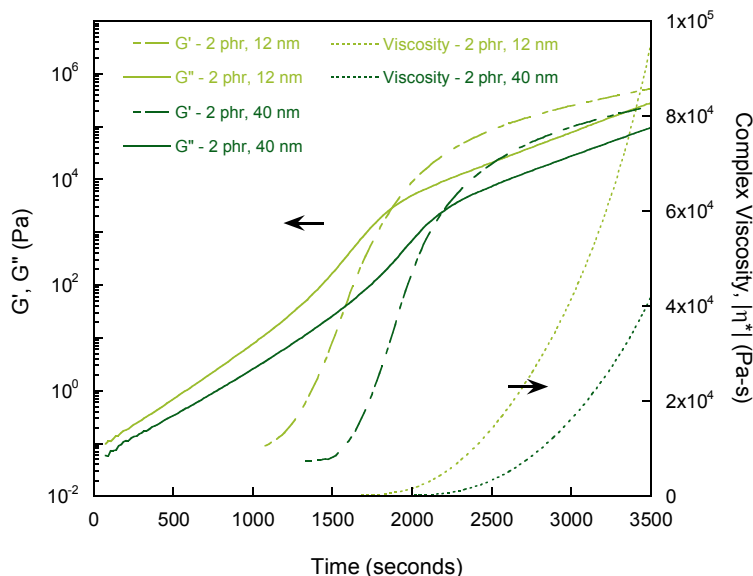
**Figure 55. Rheological properties of 12 nm fumed silica nanocomposites during cure at 130 °C.**

Figure 56 shows the rheokinetic evaluation of the 40 nm fumed silica nanocomposites at 130 °C. For both the 12 and 40 nm nanocomposites, the gel time is reduced with increasing silica content. This may be due to two factors: 1) side reactions between the hydroxyl functionality of the silica and the cyanate ester, and 2) the influence of the fumed silica on the rheological properties of the prepolymer suspensions. Both factors will reduce the gel time with increasing fumed silica loading, the former by increasing the reaction rate, and the latter by giving the material an increasingly elastic response.



**Figure 56. Rheological properties of 40 nm fumed silica nanocomposites during cure at 130 °C.**

There was an interesting feature in the  $G'$  and  $G''$  curves for the highly loaded (35 phr or 15.6 vol%) 40 nm fumed silica sample: a quick increase and subsequent decrease in both parameters around 1100 seconds. This is attributed to the shear thickening of highly loaded 40 nm fumed silica/BECy suspensions that was described above in the suspension rheology section. Overall, however, the 40 nm fumed silica nanocomposites exhibit a similar response to the 12 nm fumed silica nanocomposites, but the gel times are slightly longer, and the viscosity at gel is slightly lower. Figure 57 shows a comparison in the rheokinetics of 12 and 40 nm fumed silica samples at a loading of 2 phr (1.05 vol%).



**Figure 57. Rheokinetics comparison for 2 phr (1.05 vol%) 12 and 40 nm fumed silica nanocomposites.**

Table 2 compares gel time and properties at gel and 1000 seconds after gel. For a given volume fraction, the 12 nm silica gives a faster gel time, higher  $G'$  and  $|\eta^*|$  at gel, and higher  $G'$  and  $|\eta^*|$  1000 seconds after gel than the 40 nm silica. This may be due to changes in the reaction rate and/or rheological properties brought about by the silica.

### ***Thermal-mechanical properties of cured nanocomposites -Results***

*Storage modulus*—Representative curves for storage modulus ( $E'$ , the elastic component of the viscoelastic response) versus temperature for the 12 nm composites are shown in Figure 58. With an increase in volume fraction ( $\phi_f$ ), the magnitude of the storage modulus is increased in the glassy and rubbery regions, and all composites show the characteristic drop in modulus around the glass transition temperature,  $T_g$ , of the material. For the 40 nm fumed silica nanocomposites, representative storage modulus vs. temperature curves are shown in Figure 59.

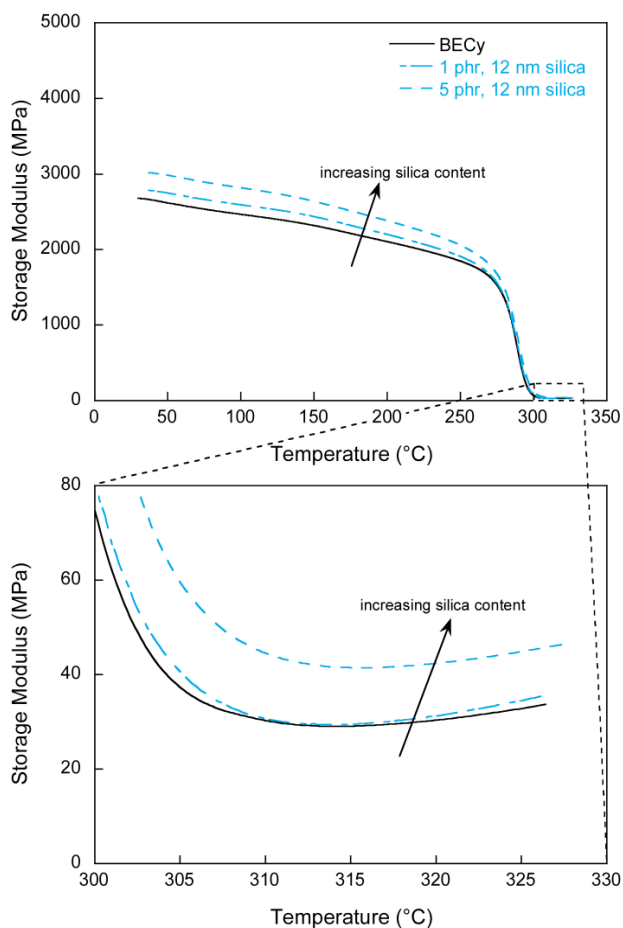


**Figure 58. Storage modulus ( $E'$ ) versus temperature for 12 nm fumed silica nanocomposites.**

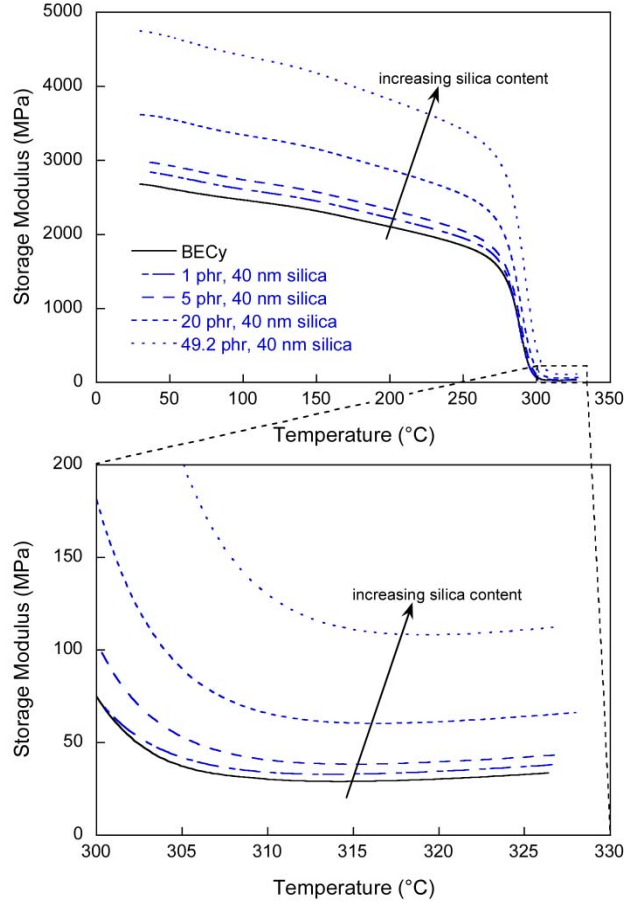


**Figure 59. Storage modulus ( $E'$ ) versus temperature for 40 nm fumed silica nanocomposites.**

For the 40 nm composites, there is also an increase in storage modulus with increased volume fraction of fumed silica. As expected, the largest increase in modulus for the 40 nm nanocomposites is for the sample at the highest loading (49.2 phr, 20.7 vol%), which represents an increase of approximately 75% over the unfilled system. The increase in storage modulus at 30 °C as a function of volume fraction for both sizes of fumed silica is shown in Figure 60, along with theoretical predictions. The isostress model (or Reuss average) assumes that the matrix and filler are stressed equally, giving the composite modulus,  $E_c$ , as

$$E_c = \left( \frac{\phi_f}{E_f} + \frac{\phi_m}{E_m} \right)^{-1} \quad (16)$$

where  $E_f$  is the modulus of the filler,  $E_m$  is the modulus of the matrix,  $\phi_f$  is the volume fraction of the filler, and  $\phi_m$  is the volume fraction of the matrix [83]. This model gives a theoretical lower bound for the composite modulus. The absolute upper bound would be given by an isostrain model, such as the rule of mixtures, where a constant strain is assumed in each of the phases. This is more suitable, however, for composites with unidirectional reinforcement and is not shown here. The predictions by the well-known Halpin-Tsai equations [84], which are explained elsewhere, are shown for the sake of comparison, with the assumption of a circular geometry factor. Possibly the most applicable model for particulate-reinforced composites is the Kerner



equation, which is analogous to an equivalent model by Hashin and Strikman [85]. Lewis and Nielsen gave the Kerner equation in a generalized form, where the ratio of the modulus of the composite to the modulus of the matrix is given by

$$\frac{E_c}{E_m} = \frac{1 + AB\phi_f}{1 - B\psi\phi_f} \quad (17)$$

where  $A$  is a constant related to the filler geometry and the Poisson's ratio of the matrix [85].

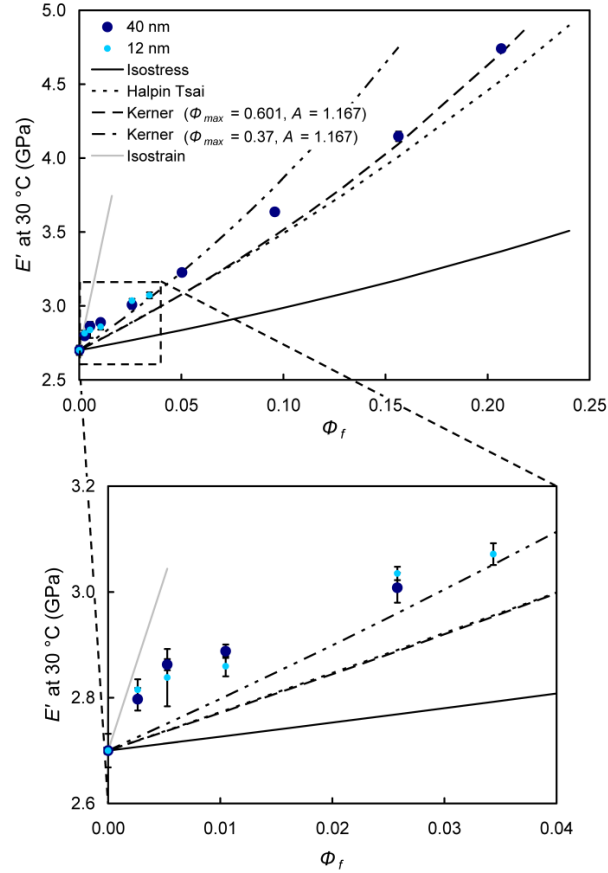


**Figure 60. Storage modulus at 30 °C vs. volume fraction of fumed silica.**

For the general case of spherical particles in a matrix,  $A$  is given by:  $A = (7-5\nu)/(8-10\nu)$ , where  $\nu$  is the Poisson's ratio of the matrix. However,  $A$  can be larger for different filler geometries, such as reinforcements with aspect ratios [85]. The constant,  $B$  is given by

$$B = \frac{E_f / E_m - 1}{E_f / E_m + A} \quad (18)$$

The limit of  $B$  is 1, where the modulus of the filler is much greater than the modulus of the matrix. The  $\psi$  term is dependent on the maximum packing fraction of the particles,  $\phi_{max}$ , and can be calculated using an equation by Lewis and Nielsen or McGee and McCullough with nearly identical results [42,85]. From McGee and McCullough,  $\psi$  is given as

$$\psi = 1 + \frac{\phi_m}{\phi_{\max}} [\phi_{\max} \phi_f + (1 - \phi_{\max}) \phi_m] \quad (19)$$

The maximum packing fraction,  $\phi_{\max}$ , is the ratio of the true volume of the filler to the apparent volume occupied by the filler, and has a maximum of 0.74 for hexagonal close packing spheres but decreases for agglomerated spheres to as low as 0.37 [85].

For all volume fractions, the isostress and Halpin-Tsai equations underestimate the composites' modulus at 30 °C. The best fit to the data is shown by the Kerner equation, where  $A$  is 1.167 (for matrix Poisson's ratio of 0.35), and either a  $\phi_{\max}$  of 0.601 (for random loose packing, non-agglomerated [85]) or 0.37 (random close packing, agglomerated). While the maximum packing factor of 0.601 gives good approximation at high loadings, 0.37 gives better fit at intermediate loadings. However, neither model will fit the data at low fractions, starting with the anomalous increase of approximately 4% in modulus for only 0.25% by volume of fumed silica. Interestingly, this result was very similar for both sizes of fumed silica, with a slightly larger increase in modulus realized for the 12 nm particles. In general, however, the packing factor of 0.601 gives the best fit to that data because it does not grossly overestimate the modulus at high volume fractions.

For the rubbery region, the increase in modulus with volume fraction is more pronounced. Figure 61 shows this relationship for the storage modulus taken at  $T_g + 30$  °C, where the  $T_g$  is defined for this purpose as the peak in the loss modulus,  $E''$  (the viscous component of the viscoelastic response). There is a general increasing trend in the composites' rubbery modulus for both sizes of fumed silica above  $\phi_f = 0.005$ , but anomalously there is a slight decrease in the rubbery storage modulus at the lowest volume fraction,  $\phi_f = 0.0025$ , where the marked increase was observed in the glassy region. This may not be significant, as the standard deviation for the rubbery modulus at these loadings actually includes the base value of the resin (See Figure 61). Also, due to the fact that these values are taken at 30 °C above  $T_g$ , there may be slight temperature effects due to the changes in  $T_g$  for each composition. Regardless, above 0.5 vol%, there is a marked improvement in rubbery modulus, such that the Halpin-Tsai equations greatly underestimate the increase in modulus. In order to provide a fit to the experimental data in the rubbery region, a  $\phi_{\max}$  of 0.37 (random close packing, agglomerated) must be adopted. All packing factors larger than this underestimate the increase in modulus. Furthermore, using  $A = 1.5$  (for rubber Poisson's ratio of 0.5) underestimates the modulus, such that a value for  $A$  of 4 is needed for the 40 nm composites, while an  $A$  of 10 is needed for the 12 nm particles. In general, the value for  $A$  will increase if the aspect ratio of the filler increases, and the same result is given for agglomerated fillers [85].

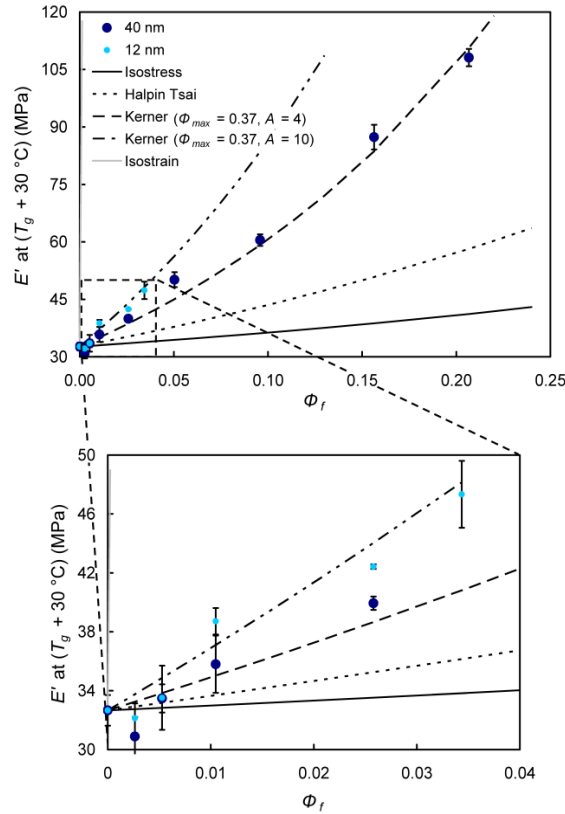


**Figure 61. Rubbery storage modulus (@  $T_g + 30$  °C) vs. volume fraction.**

The trend of a greater increase in modulus in the rubbery region than for the glassy region is not new; this has been observed by several researchers for both micron- and nano-sized filler composites [41,42]. Goyanes et al. [41] showed a similar result for quartz/epoxy composites, attributing this to the fact that, below  $T_g$ , the rigid polymer matrix can exert large forces on the agglomerates, causing some particle motion and slippage, and a decrease in modulus. For the rubbery state, however, the relaxation of the matrix allows the agglomerates to stay rigid and provide more reinforcement [41]. Vassileva and Friedrich [42] also showed this phenomenon for alumina nanoparticle/epoxy composites.

The storage modulus data suggests that there is a presence of agglomerates in the nanocomposites, which are more prevalent in the rubbery state, especially for the 12 nm particles. This is consistent with analysis of TEM micrographs for the composites, as shown in Figure 62(a) and Figure 62(b). It is obvious that the smaller fumed silica particles (12 nm) form much more dominant agglomerates (aggregates entangled together) than the 40 nm particles. For the 40 nm composite, there are aggregates and agglomerates of a small number of particles and some particles that exist alone, while for the 12 nm particles, nearly all particles exist as agglomerates of many particles. Although the total aggregate and agglomerate size is larger, the larger 40 nm particles behave more like dispersed spheres than the highly aggregated and agglomerated 12 nm particles. This explains the need for a higher  $A$  for the 12 nm particles in the rubbery region, since these agglomerates have a much more dominant effect above  $T_g$ .

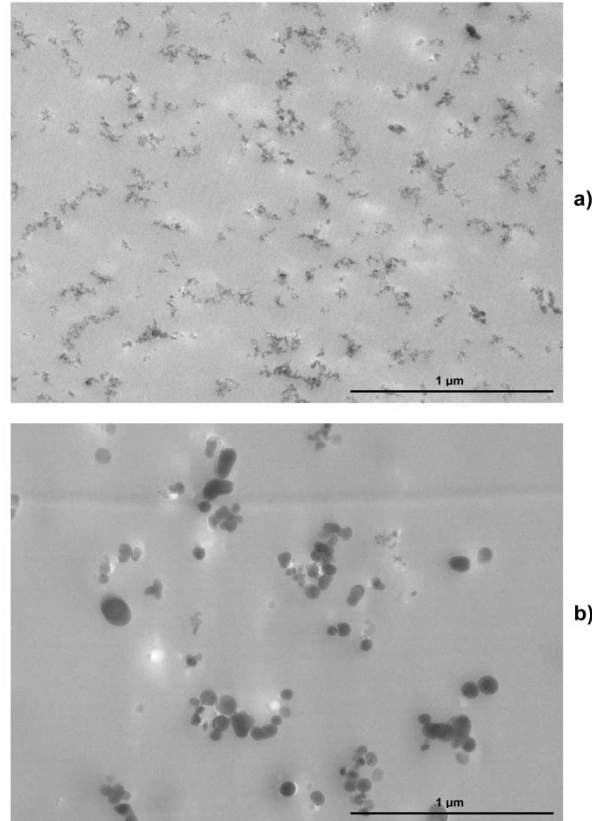


**Figure 62.** TEM micrographs of nanocomposites at a loading of 2.6 vol%, a) 12 nm silica, b) 40 nm silica.

*Tan delta*—Figure 63 shows tan delta ( $E''/E'$ , ratio of energy dissipated to energy stored per cycle) as a function of temperature for the 12 nm nanocomposites, and Figure 64 shows tan delta for the 40 nm nanocomposites.

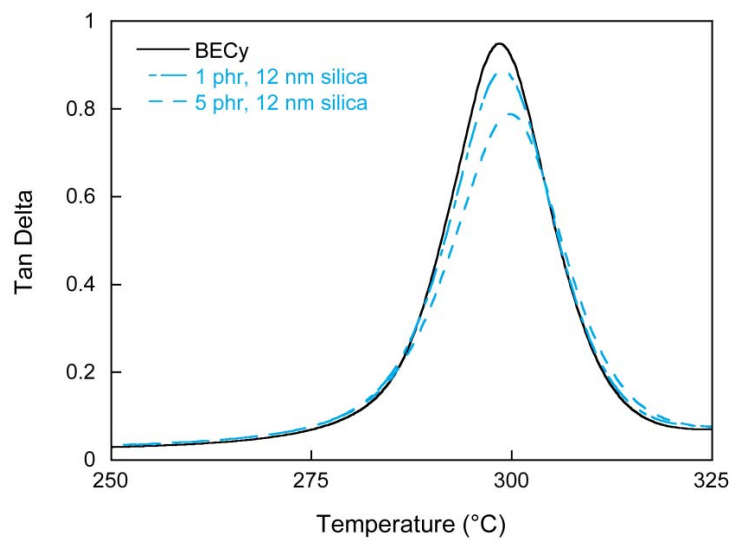


**Figure 63.** Tan delta (damping) as a function of temperature near the glass transition (12 nm silica).

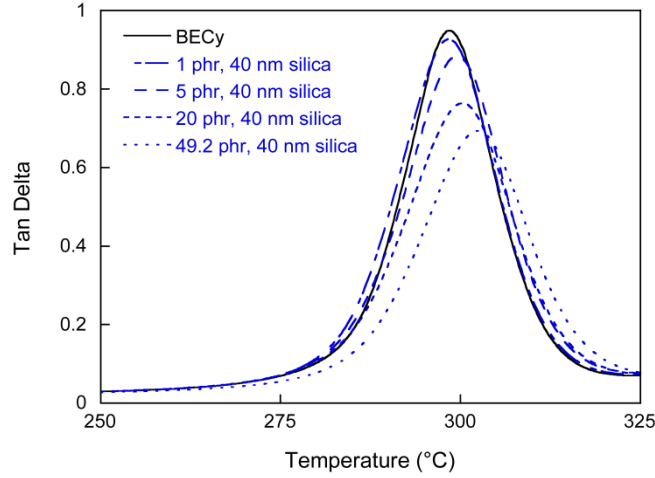


**Figure 64. Tan delta (damping) as a function of temperature near the glass transition (40 nm silica).**

While the peak position does not change drastically (indicating little change in  $T_g$ , which will be discussed later), the magnitude of the tan delta peak decreases with increasing filler content for both particle sizes. If the damping of the rigid filler is neglected, the decrease in damping as a result of replacing polymer with filler is given by

$$\tan \delta_c = \tan \delta_m (1 - \phi_f) \quad (20)$$

where  $\tan \delta_c$  is the damping of the composite and  $\tan \delta_m$  is the damping of the matrix [42,85]. However, the damping of the composite can decrease beyond the prediction of Equation 20 if there is a significant interaction between the filler and matrix, such that a correction parameter,  $P$ , is introduced [41,42], giving

$$\tan \delta_c = \tan \delta_m (1 - P\phi_f) \quad (21)$$

The effective interfacial thickness of the interphase between the polymer and particle,  $\Delta R$ , is related to  $P$  by

$$P = \left(1 + \frac{\Delta R}{R}\right)^3 \quad (22)$$

where  $R$  is the radius of the particles in question [41,42].

Using Equations 21 and 22, the interfacial thickness,  $\Delta R$ , was estimated through comparison of the data for each composite with the matrix, yielding estimates of the effective thickness, which are tabulated in Table 7.

**Table 7. Interphase thickness estimation from damping behavior for 12 and 40 nm silica nanocomposites.**

<b>phr (12 nm)</b>	<b><math>\phi_f</math></b>	<b><math>\Delta R</math> [nm]</b>
0.5	0.003	6.4
1	0.005	7.1
2	0.010	5.4
5	0.026	5.0
6.72	0.034	4.5
<b>Avg. <math>\Delta R</math> [nm] for 12 nm:</b>		<b>5.7</b>
<b>phr (40 nm)</b>	<b><math>\phi_f</math></b>	<b><math>\Delta R</math> [nm]</b>
0.5	0.003	12.3
1	0.005	4.0
2	0.010	13.2
5	0.026	7.3
10	0.050	5.6
20	0.096	4.9
35	0.156	2.7
49.2	0.207	1.6
<b>Avg. <math>\Delta R</math> [nm] for 40 nm:</b>		<b>6.4</b>

There is a general decreasing function of  $\Delta R$  with respect to volume fraction, possibly indicating that as volume fraction increases, particle agglomeration is increased, which decreases the available free surface area of the particles to interact with the cyanate ester matrix. For  $\phi_f = 0.005$  with the 40 nm composites,  $\Delta R$  is quite low compared to the surrounding data, but this result was rechecked and there is no apparent explanation for the presence of this outlier.

The presence of a strong interface between the cyanate ester matrix and the fumed silica particles is in agreement with the literature on cyanate ester composites. This is due to the abundant presence of hydroxyl groups on the silica particles' surface. In fact, it has been shown by Liang et al. that Polyhedral Oligomeric Silsesquioxane (POSS) with hydroxyl functionality form covalent bonds with cyanate esters via iminocarbonate groups [86]. Furthermore, hydrogen bonding can occur between the hydroxyl and cyanate groups of the silica and cyanate esters, respectively [86]. Cyanate esters have also been shown to form covalent bonds with substrate hydroxyl groups on other surfaces, such as glass and carbon fibers and metallic substrates [87]. The average  $\Delta R$  for the 40 nm composites is slightly greater than for the 12 nm composites, but there is a much larger change in  $\Delta R$  for the 40 nm composites. This may indicate that at low volume fractions, the 40 nm composites have many individual particles or small aggregates, which have a large amount of available surface area, but at large volume fractions, the 40 nm particles are highly agglomerated, decreasing the amount of available surface area. This is consistent with the observations made through TEM, as shown in Figure 62. For the 12 nm particles, agglomeration is pronounced at all volume fractions such that the decrease in  $\Delta R$  with volume fraction is not as substantial.

*Glass transition*—Figure 64 shows the glass transition temperatures for the 12 and 40 nm composites, calculated by three methods: 1) Onset of the drop in storage modulus, 2) Loss modulus peak, and 3) Tan delta peak.

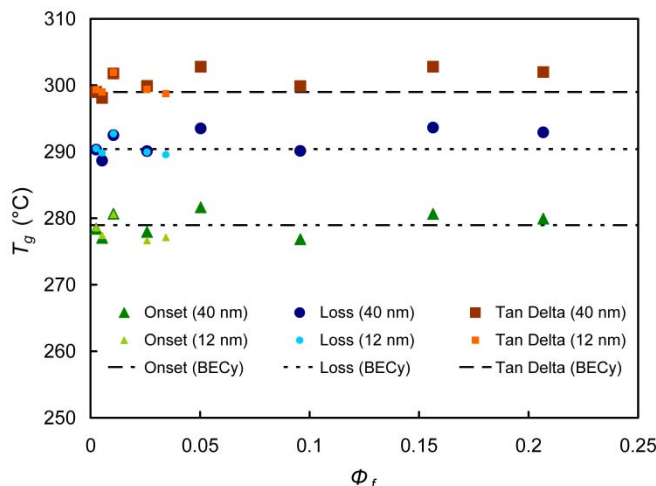


**Figure 65.**  $T_g$  versus volume fraction of fumed silica, with horizontal lines indicating the glass transition temperature of the neat BECy resin. Error bars are on same order as symbol size.

It is apparent that there are only very small changes ( $\pm < 4$  °C) in glass transition temperature for all volume fractions. While a discernable trend is not immediately obvious, it is interesting to note that the  $T_g$ 's for the 12 and 40 nm samples follow the same trend. This indicates sources of systematic error because the equal volume fraction samples were prepared side by side. While all efforts were made to limit the moisture exposure of the fumed silica between drying and incorporation into the cyanate ester monomer, the relative humidity of the laboratory varied from day to day, from as little as 19% RH to 60% RH. In fact, if only the samples prepared during conditions of less than 20% relative humidity are considered, as shown in Figure 66, the  $T_g$  increases at each volume fraction.

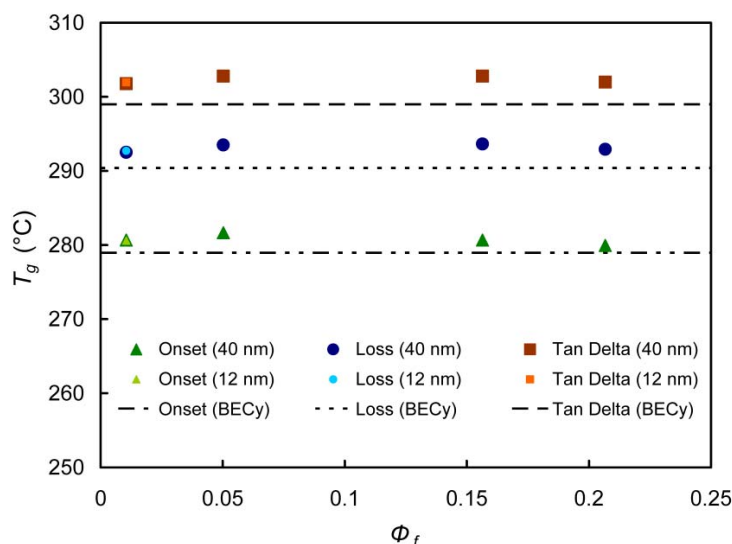


**Figure 66.**  $T_g$  versus volume fraction of fumed silica, with horizontal lines indicating the glass transition temperature of the neat BECy resin (Samples prepared in humid conditions were eliminated from this graph).

Our hypothesis was tested by making identical samples on different days. For example, the  $T_g$  in 2 phr samples (both 12 and 40 nm) decreased between 2 and 3 °C for a change between 19% and 49% RH. Furthermore, the decrease for the 12 nm samples was larger, which is consistent with the fact that the 12 nm particles have more surface area with which to absorb moisture. It should be noted, however, that other properties, such as modulus and damping, were not affected by the changes in humidity.

To ascertain more information on the effect of the silica nanoparticles on the glass transition temperature of the nanocomposites, a study on the effect of post cure temperature was conducted for a single volume fraction of both 12 and 40 nm particles. The results are shown in Figure 67.

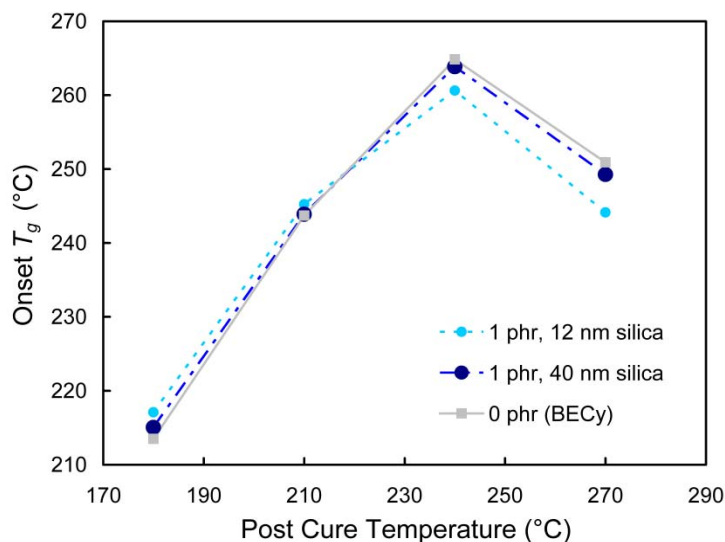


**Figure 67.  $T_g$  vs. post-cure temperature for 1 phr samples.**

These results clearly show that at low conversions, the  $T_g$  of the nanocomposites is higher, while at high conversions, the  $T_g$  is lower than the neat BECy resin. For the highest post-cure temperature, 270 °C, there is a reduction in  $T_g$  of all samples including the neat resin, which indicates that thermal degradation is occurring at these temperatures. There are three major factors that affect the glass transition temperature of these nanocomposites. First, the incorporation of the rigid fumed silica into the crosslinked network of cyanate ester serves to decrease segmental motion, which would serve to increase  $T_g$ . Second, the incorporation of the fumed silica into the polymer will decrease the overall cross-link density of the resin per unit volume, which would decrease  $T_g$ . Third, the fumed silica may add free volume because of disruption in packing of the cyanate ester resin segments, decreasing  $T_g$ . For low conversions, the incorporation of fumed silica into the polymer network gives a positive effect on  $T_g$  because there is an excess of unreacted cyanate groups that can link to the fumed silica and decrease large scale segmental motion. For high conversions, however, there is a negative effect on  $T_g$  because the increase in  $T_g$  due to the first factor is not enough to overcome the decrease in  $T_g$  due to a reduction in cross-link density and increase in free volume, as compared to the neat cyanate ester that nears complete conversion.



### ***Repair system evaluation with nano filled BECy***

The bond strength of nano filled BECy was evaluated initially by using lap shears testing. Different nano filled resins were prepared by adding 2 wt.-% of fumed silica (Si), alumina (Al), sol-gel silica and multi-walled carbon nanotubes (MWCNT) in BECy. The lap shear strength of all the resins was measured on BMI-cf and aluminum substrates.

Figure 68 illustrates the variation of lap shear strength of various nano resins on BMI-cf PMC and aluminum substrates. The lap shear strengths on the PMC substrate was observed to be similar for all the investigated resins, where as the lap shear strength of Al filled BECy was observed to be higher than other nano resins on the alumina substrate. By comparing the lap shear strength of all the nano resins, it was concluded that Al filled BECy was to be selected for studying the enhancement of repair efficiency with nano resin.

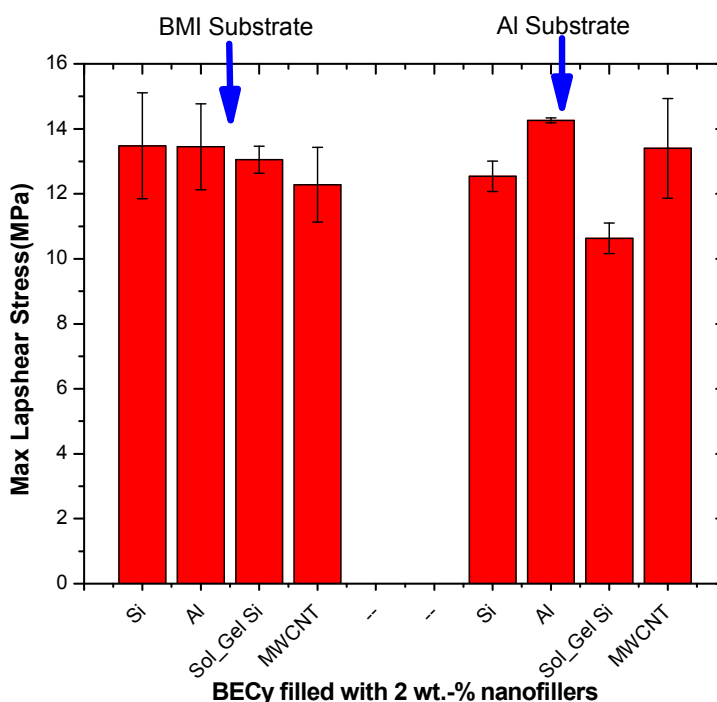


**Figure 68. Lap shear testing of nano resins on BMI-cf PMC and Aluminum substrate**

After determining the best nano resin with a high bond strength, the influence of the filler content in BECy was investigated. Al nano resin at 2.5 and 10 wt.% of Al in BECy were prepared and these resins were used for injection repair of delaminated HPS specimens. Figure 69 depicts the results from HPS-after-HPS test. It can be observed that Al filled nano resin had no significant affect on the effectiveness of repair or on composite strength of the sample after repair. The HPS specimens repaired with 2.5 wt% and 10 wt% alumina showed similar strength.

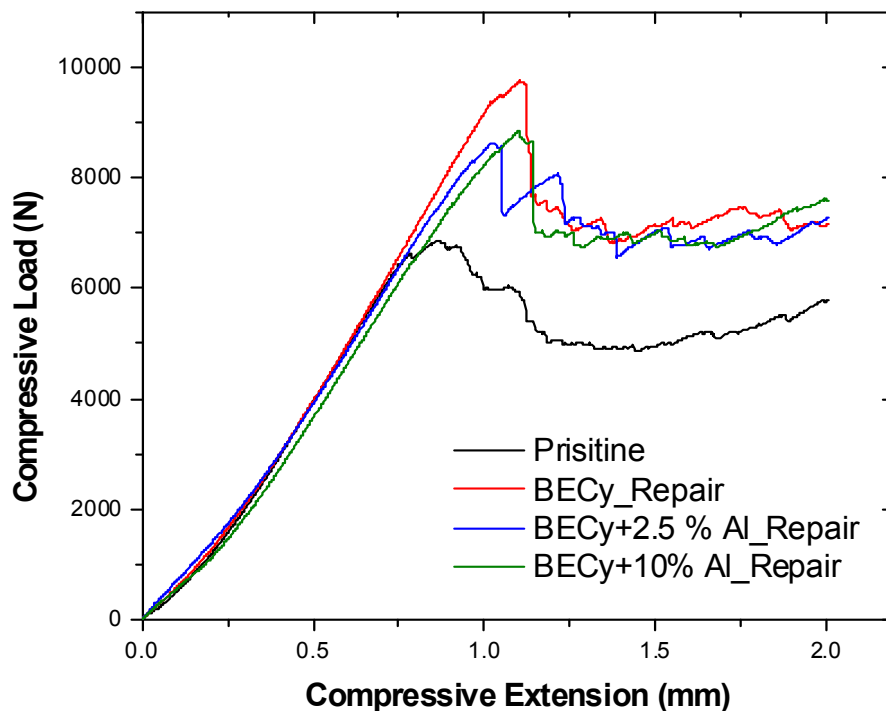


Figure 69. HPS testing of nano resin repaired specimens in comparison with pristine and BECy repair specimens

Further, it can be observed that samples repaired with pure BECy have the approximately the same maximum compressive peak loads as the samples repaired with 2.5 wt% and 10 wt% alumina nano particles (Figure 69). This confirms that the addition of alumina nano particles in BECy resin is not beneficial for the repair of high temperature composites.

## Conclusions and Implications for Future Research/Implementation

*Cure kinetics*— BECy monomer is cured via trimerization reaction, without volatile products, to form a high  $T_g$  amorphous network. We investigated the cure kinetics of BECy by differential scanning calorimetry (DSC). Both dynamic and isothermal experiments were carried out to obtain the kinetic parameters. An autocatalytic model was successfully used to model isothermal curing. The activation energy determined by autocatalytic modeling is 60.3 kJ/mol and the total reaction order is about 2.4. The empirical DiBenedetto equation was used to evaluate the relationship between  $T_g$  and conversion. The activation energy ( $E_a$ ) of BECy is calculated as 66.7 kJ/mol based on Kissinger. The isoconversional analysis shows the activation energy changes as reaction progress.

*Rheology of nano-suspensions*—A low viscosity bisphenol E cyanate ester (BECy) monomer was combined with fumed silica with average primary particle diameters of 12 and 40 nm to form high-temperature adhesives with processability at ambient temperatures. Rheological evaluation revealed that for silica loadings below 15 vol%, suspensions of both particle sizes exhibited shear thinning and thixotropic behavior. Samples with high silica loadings (>15 vol%) of 40 nm silica also showed intense shear thickening at shear rates above  $10\text{ s}^{-1}$ . Thixotropy was most pronounced for the 12 nm silica, but the formation of a gel was slow, indicating that the polar nature of the BECy monomer was responsible for disrupting hydrogen-bonds between silica particles. Rheokinetic evaluation of catalyzed samples showed that increasing silica content reduced gel time and increased gel viscosity, and this effect was most pronounced for the 12 nm silica.

*Adhesive strength and repair system evaluation*—Bisphenol E cyanate ester (BECy) was observed to be an effective resin for the repair of BMI-cf composite panels commonly used for high temperature applications. A mixed mode fracture of interface and substrate failure was observed in BECy bonded lap shear specimens. This failure was attributed to the formation of a strong interfacial bond between BECy and the BMI-cf substrate. In short beam shear bending tests, the low viscosity and high toughness of BECy at room temperature was observed to play a vital role in enhancing the structural strength of the specimen. The DCB tests clearly demonstrate the enhancement in interlaminar debonding strength as a result of BECy repair. The crack resistance curves that quantify the crack initiation and propagation behaviors in delaminated composite specimens reveal that BECy repaired composites have high resistance to crack initiation and propagation. From SEM analysis of the fracture surfaces, fiber bridging was observed for BECy repaired DCB specimens. The results from lap shear, SBSB and DCB tests reveals that 100 % repair efficiency can be accomplished by repairing the delaminated BMI-cf composites with BECy resin. Qualitative evaluation of repair efficiency from C-Scan images and florescence dye penetration tests reveal complete infiltration of BECy resin into the microscopic cracks in the delamination zone. Furthermore, a repair efficiency of 155 % in HPS after HPS test and 100 % in CAI test were observed.

*Adhesive strength and repair system evaluation with nano resin*—Different types of nano-reinforced resins were prepared by mixing alumina nanoparticles, silica nanoparticles, and multi walled carbon nanotubes in BECy. The adhesive bond strength screened by lap shear testing revealed that alumina filled BECy is best for injection repair. However, Al filled nano resin had no significant effect on the repair strength versus the neat BECy system.

*Thermal-mechanical properties of cured nanocomposites*— Fumed silica particles with average primary particle diameters of 12 and 40 nm were combined with a low viscosity bisphenol E cyanate ester resin to form composite materials with enhanced storage modulus and reduced damping behavior, as evidenced by dynamic mechanical analysis (DMA). The storage modulus increased with volume fraction of fumed silica in both the glassy and rubbery regions, but the increase was more pronounced in the rubbery region. The maximum increase in storage modulus in the glassy region was 75% for 20.7 vol% of 40 nm fumed silica, while the same composition showed a 231% increase in the rubbery storage modulus. Furthermore, decreases in damping behavior were used to estimate the effective polymer-particle interphase thickness. The

glass transition temperature of the nanocomposites was not changed significantly with increasing volume fraction.

## Literature Cited

- [1] Talrega R. Damage development in composites: mechanisms and modeling. *Journal of Strain Analysis for Engineering Design* 1989;24:215-222.
- [2] Bandyopadhyay S, Gellert EP, Silva VM, Underwood JH. Microscopic Aspects of Failure and Fracture in Cross-Ply Fibre Reinforced Composite Laminates. *Journal of Composite Materials*, 23: 1216-1231, 1989.
- [3] Talrega R. (ed.). *Damage Mechanics of Composite Materials*. New York: Elsevier Press, 1994.
- [4] Bascom WD, Bitner JL, Moulton RJ, Siebert AR. The interlaminar fracture of organic-matrix, woven reinforcement composites. *Composites*,11(1): 9-18, 1980
- [5] Gamstedt EK, Talrega R. Fatigue damage mechanisms in unidirectional carbon-fibre-reinforced plastics. *Journal of Material Science* 1999;34:2535-2546
- [6] Hollaway L. *Polymer Composites for Civil and Structural Engineering*, Blackie Academic and Professional, an imprint of Chapman and Hall, London, 1993
- [7] Hoke, M., *Repair Applications, Quality Control, and Inspection*, ASM Handbook-Composites, vol 21, Miracle, D, Donaldson, SL, eds., ASM International: 885, 2001.
- [8] Heslehurst RB. Challenges in the repair of composite structures—Part I. *SAMPE Journal* 1997;33(5):11-16.
- [9] Heslehurst RB. Challenges in the repair of composite structures—Part II. *SAMPE Journal* 1997;33(6):16-21
- [10] Liu D, Lee CY, Lu X. Repairability of impact-induced damage in SMC composites. *Journal of Composite Materials* 1993;27(13):1257-1270
- [11] Mahler M, Hahn HT. Repair methods for composite structures. In: Eighth Japan-U.S. Conference on Composite Materials, Baltimore, Md., Sept. 24-25, 1998, Proceedings (A99-19426 04-24), Lancaster, Pa., Technomic Publishing Co., Inc., p. 53-62.
- [12] Russell AJ, Bowers CP. Resin requirements for successful repair of delaminations. In: 36th International SAMPE Symposium, San Diego, Calif., April 15-18, 1991, p. 2279-2291.
- [13] Dehm S, Wurzel D. Fast in-situ repair of aircraft panel components. *Journal of Aircraft* 1989;26(5):476-481.
- [14] Heslehurst RB. Repair of delamination damage—A simplified approach. *International SAMPE Symposium and Exhibition* 1996;41(2):915-924.
- [15] Suchar-Buell KJ. Structural repair of composites. *Polymer and Polymer Composites* 1993;1(4):297-308.
- [16] Mehrkam, P. A. and Cochran, R., Liquid Dicyanate Ester Monomer Resin for Elevated Temperature Composite Repair Applications, *Proceedings of the American Society for Composites*, 1992, p 12-21.
- [17] Mehrkam, P. A., and Cochran, R., Evaluation of Materials for Composite Repair Applications, *Journal of Thermoplastic Composite Materials*, 10(1): 51-60, 1997.
- [18] ASM Handbook, Composites, v. 21, on-line edition.
- [19] Hamerton, I., *Chemistry and Technology of Cyanate Ester Resins*, Blackie Academic and Professional, 1994.

- [20] Shimp, D. A., and Craig, Jr., W. M., New Liquid Dicyanate Monomer for Rapid Impregnation of Reinforcing Fibers, Proceedings of the 34th Annual International SAMPE Symposium, May 1989, p 1336-1346.
- [21] Meador, M. A., Recent Advances in the Development of High-Temperature Polymers, Annual Review of Materials Science, 28: 599-630, 1998.
- [22] Snow, A. W., The Synthesis, Manufacture, and Characterization of Cyanate Ester Monomers, in Chemistry and Technology of Cyanate Ester Resins (Hamerton, I.), Blackie Academic and Professional, 1994.
- [23] Shimp, D. A., Christenson, J. R., and Ising, S. J., Cyanate Esters – An Emerging Family of Versatile Composite Resins, Proceedings of the 34th Annual International SAMPE Symposium, May 1989, p 222-233.
- [24] Hillermeier, R., and Seferis, J., Environmental Effects on Thermoplastic and Elastomer Toughened Cyanate Ester Composite Systems, Journal of Applied Polymer Science, 77(3): 556-567, 2000.
- [25] Black, S., Are High-Temp Thermosets Ready to go Commercial?, High-Performance Composites, Nov. 2004.
- [26] Esslinger, J. R., and Fruchtnicht, O. C., Cyanate Ester Matrix Technology for Improved Thermal Performance of Filament Wound Missile Structures, SAMPE Journal, (40)6: 9-15, 2004.
- [27] Parfitt, G.D. Dispersion of Powders in Liquids with special reference to pigments, Third edition, Applied Science Publishers LTD 1981.
- [28] Hsiao, Kuang-Ting, Alms, Justin, and Advani, Suresh G. Nanotechnology, 14: 791-793, 2003.
- [29] Tyagi, S., Lee, J. Y., Buxton, G. A., and Balazs, A. C.. Macromolecules 2004, 37, 9160-9168.
- [30] Tari, G., Ferreira, M.F., and Fonseca, A.T., “Influence of Particle Size and Particle Size Distribution on Drying-Shrinkage Behavior of Alumina Slip Cast Bodies,” Ceramics International, 25(1990) 577-580.
- [31] Tari, G. Ferreira, M.F., Fonseca, A.T., and Lyckfeldt, O., “Influence of Particle Size Distribution on Colloidal Processing of Alumina,” J. European Ceramic Society, 18 (1998) 249-253.
- [32] Schneider, M, Claverie, J., Graillat, C., and McKenna, T.F., “High Solids Content Emulsions. I. A Study of the Influence of the Particle Size Distribution and Polymer Concentration on Viscosity,” J. Appl. Polym. Sci. 84, 1878-1896, 2002.
- [33] Zaman, A.A., Moudgil, B.M., “Rheology of Bidisperse Aqueous Silica Suspensions: A New Scaling Method for the Bidisperse Viscosity,” J. Rheol., 42(1) 21-39 (1998).
- [34] Zupancic, A., Lapasin, R., and Kristoffersson, A., “Influence of Particle Concentration on Rheological Properties of Aqueous  $\alpha$ -Al<sub>2</sub>O<sub>3</sub> Suspensions,” J. European Ceramic Society, 18 (1998) 476-477.
- [35] Tari, G., Ferreira, M.F., and Fonseca, A.T., “Influence of Particle Size and Particle Size Distribution on Drying-Shrinkage Behavior of Alumina Slip Cast Bodies,” Ceramics International, 25(1990) 577-580.

- [36] Tari, G. Ferreira, M.F., Fonseca, A.T., and Lyckfeldt, O., "Influence of Particle Size Distribution on Colloidal Processing of Alumina," *J. European Ceramic Society*, 18 (1998) 249-253.
- [37] Rand, B. and Fries, R., "Viscoelasticity of nano-alumina dispersions," pp. 165-72 in *Ceramic Transactions, Vol. 62, Science, Technology, and Commercialization of Powder Synthesis and Shape Forming*. Edited by J. J. Kingsley, C. H. Schilling, and J. Adair. American Ceramic Society, Westerville, OH, (1996).
- [38] AEROSIL® Product Technical Information. Frankfurt, Germany: Degussa, 2006.
- [39] CAB-O-SIL® M-5 Product Technical Data. Billerica, MA: Cabot Corp., 2000.
- [40] Iisaka K, Shibayama K. Effect of filler particle size on dynamic mechanical properties of poly(methyl methacrylate). *J Appl Polym Sci* 1978;22(5):1321-1330.
- [41] Goyanes SN, Konig PG, Marconi JD.. *J Appl Polym Sci* 2003;88(4):883-892.
- [42] Vassileva E, Friedrich K. Epoxy/alumina nanoparticle composites. I. Dynamic mechanical behavior. *J Appl Polym Sci* 2003;89(14):3774-3785.
- [43] AEROSIL® Product Technical Information. Frankfurt, Germany: Degussa, 2006.
- [44] CAB-O-SIL® M-5 Product Technical Data. Billerica, MA: Cabot Corporation, 2000.
- [45] ASTM D5868 – 01. Standard Test Method for Lap Shear Adhesion for Fiber Reinforced Plastic (FRP) Bonding. 2008.
- [46] ASTM D-2344, American society for testing and materials, West Conshohocken, PA, 2001.
- [47] ASTM D-5528-94. Annual Book of ASTM Standards, 1994.
- [48] Kessler MR, White SR. Composites: Part A: Applied Science and Manufacturing. 2001;32:683-699
- [49] Bader MG, Hamerton I, Hay JN, Kemp M, Winchester S.. Composites: Part A: Applied Science and Manufacturing. 2000;31:603-608
- [50] Williams JG. The fracture mechanics of delamination tests. *J Strain Anal* 1989;24:207–214.
- [51] Boey, F. Y., Qiang, W., *Polymer*, 41 (2000) 2081.
- [52] Nielsen, L. E. *J. Macromol. Sci. Rev. Macromol. Chem.*, C3 (1969) 69.
- [53] Kessler, M. R., White, S. R., *J. of Polym. Sci. Part A*, 40 (2002) 2373.
- [54] Prime, R. B., *Polym Eng. Sci.*, 13 (1973) 365.
- [55] Lu, M. C., *Polymer*, 35 (1994) 2822.
- [56] Kissinger, H. E., *Anal Chem.*, 29 (1957) 1702.
- [57] Flynn, J. H. and Wall, L. A., *Polym. Lett.*, 4 (1966) 232.
- [58] Ozawa, T. *Bull. Chem. Soc. Jpn*, 38 (1965) 1881.
- [59] Ozawa, T. *J. Them. Anal.*, 2 (1970) 301.
- [60] Salla, J. M. and Ramis, X., *Polym. Eng. Sci.*, 36 (1996) 835.
- [61] Pielichowski, K., Czub, P., J. Pielichowski, *Polymer*, 41 (2000) 4381.
- [62] Chen, Y. and Macosko, C. W., *J. of Appl. Polym. Sci.*, 62 (1996) 567.
- [63] Sottos NR. The Influence of the Fiber/Matrix Interface on Local Glass Transition Temperature. *Polymer Solutions, Blends, and Interfaces*. 1992;11:339-58.
- [64] Bai SL, Djafari V, Andréani M, Francois D. Composites Science and Technology. 1995;55:343-348
- [65] Jandro LA, Yi S, Vatsavaya MS, Medikonda S, Kier Z, Jayasinghe C, Rooy N, Vesselin NS, Mark JS. Composites Science and Technology 2010;70:1113-1119

- [66] Whitney JM, Browning CE, Hoogsteden W. *Journal of Reinforced Plastics and Composites*. 1982;1(4):297-313.
- [67] Ripling EJ, Mostovoy S, Patrick RL. ASTM STP 360, American Society of Testing and Materials, Philadelphia, PA, 1964:5-19.
- [68] Bascom WD, Bitner JL, Moulton RJ, Siebert AR. *Composites*. 1980;11(1):9-18.
- [69] Rao BN, Acharya AR. *Engineering Fracture Mechanics*. 1995;51(2):317-322.
- [70] Hwang W, Han KS. *Journal of composite materials*. 1982;23:396-430
- [71] Susan W. *Macromol materials and engineering*. 2004;289:447-456.
- [72] Raghavan S, Walls HJ, Khan SA. *Langmuir* 2000;16(21):7920-7930.
- [73] Wen J, Bryant D. *Adhes & Seal Ind* 1999;6(6):48-53.
- [74] Li C, Akinc M. *J Am Ceram Soc* 2005;88(6):1445-1454.
- [75] Raghavan SR, Khan SA. *J Colloid Interf Sci* 1997;185(1):57-67.
- [76] Smith WE, Zukoski CF. *J Rheol* 2004;48(6):1375-1388.
- [77] Bender J, Wagner NJ. *J Rheol* 1996;40(5):899-916.
- [78] Lee YS, Wagner NJ. *Rheol Acta* 2003;42(3):199-208.
- [79] Malkin AY, Isayev AI. *Rheology: Concepts, Methods, & Applications*. Toronto: ChemTech Publishing, 2006.
- [80] Yousefi A, Lafleur PG, Gauvin R. *Polym Composite* 1997;18(2):157-168.
- [81] Ganguli S, Dean D, et al. *Polymer* 2003;44(22):6901-6911.
- [82] Simon SL, Gillham JK. *J Appl Polym Sci* 1993;47(3):461-485.
- [83] Sperling LH. *Polymeric Multicomponent Materials: An Introduction*. New York: John Wiley & Sons, 1997.
- [84] Halpin JC. *Primer on Composite Materials Analysis*, 2nd ed. Lancaster, PA: Technomic Publishing Co., 1992.
- [85] Nielsen LE, Landel RF. *Mechanical Properties of Polymers and Composites*, 2nd ed. New York: Marcel Dekker, 1994.
- [86] Liang K, Li G, Toghiani H, Koo JH, Pittman, Jr. CU. *Chem Mater* 2006;18(2):301-312.
- [87] Hamerton I. *Chemistry and Technology of Cyanate Ester Resins*. London: Chapman and Hall, 1994.



## Appendix A: List of Technical Publications

### ***Peer Reviewed Journals***

1. X. Sheng, M. Akinc, M. R. Kessler: *Cure Kinetics of Thermosetting Bisphenol E Cyanate Ester*, **Journal of Thermal Analysis and Calorimetry**; 2008; 1, 77-85.
2. X. Sheng, M. Akinc, M. R. Kessler: *The Effects of Alumina Nanoparticles on the Cure Kinetics of Bisphenol E Cyanate Ester*, **Polymer Engineering and Science**; 2010; 50(6), 1075-1084
3. W. K. Goertzen, X. Sheng, M. Akinc, and M. R. Kessler: *Rheology and Curing Kinetics of Fumed Silica/Cyanate Ester Nanocomposites*, **Polymer Engineering and Science**; 2008; 48, 875-883.
4. W. K. Goertzen and M. R. Kessler: *Dynamic Mechanical Analysis of Fumed Silica/Cyanate Ester Nanocomposites*, **Composites Part A: Applied Science and Manufacturing**; 2008; 39, 761-768.
5. W. K. Goertzen and M. R. Kessler: *Thermal Expansion of Fumed Silica/Cyanate Ester Nanocomposites*, **Journal of Applied Polymer Science**; 2008; 109, 647-653.
6. W. K. Goertzen, M. R. Kessler: *Three-phase Cyanate Ester Composites with Fumed Silica and Negative-CTE Reinforcements*, **Journal of Thermal Analysis and Calorimetry**; 2008; 1, 87-93.
7. W. K. Goertzen and M. R. Kessler: *Thermal Expansion of Fumed Silica/Cyanate Ester Nanocomposites*, **Journal of Applied Polymer Science**; 2008; 109, 647-653.
8. X. Sheng, M. Akinc, M. R. Kessler: *Creep Behavior of Bisphenol E Cyanate Ester/Alumina Nanocomposites*, **Materials Science & Engineering. A, Structural Materials**; 2010; 527, 5892-5899
9. X. Sheng, M. Akinc, M. R. Kessler: *Rheology and Dynamic Mechanical Analysis of Bisphenol E Cyanate Ester/Alumina Nanocomposites*, **Polymer Engineering and Science**; 2010; 50(2), 302-311
10. K. A. Ament, M. R. Kessler, M. Akinc: *Cyanate Ester-Alumina Nanoparticle Suspensions: Effect of Alumina Concentration on Viscosity and Cure Behavior*, **Polymer Engineering and Science**; In Press, 2010.
11. M. Thunga, W. Lio, M. Akinc, M. R. Kessler, *Engineering the adhesive strength of Bisphenol E Cyanate Ester resin for injection repair of high glass transition temperature polymer matrix composites* **Composites Science and Technology**, 2011, 71, 239-245
12. M. Thunga, W. Lio, M. Akinc, M. R. Kessler, "Injection repair of advanced polymer matrix composites by using novel high glass transition Cyanate Ester resin", In preparation.

### ***Conference/Symposium Proceedings/ Published Technical Abstracts***

13. Xia Sheng, Mufit Akinc, Michael R. Kessler "Cure Kinetics of Thermosetting Bisphenol E Cyanate Ester" Proceedings of the North American Thermal Analysis Society Annual Conference (NATAS 2007). Aug. 26-29, 2007. East Lansing, MI. CD-ROM, Paper 19-441: p 1-11.
14. M. R. Kessler, M. Akinc, X. Sheng, W. K. Goertzen "Environmentally Benign Repair of Composites Using High Temperature Cyanate Ester Nanocomposites: Resin Development" The Partners in Environmental Technology Technical Symposium and Workshop

- (Sponsored by SERDP and ESTCP), December 4-6, 2007, Washington D.C. Poster Presentation.
15. Michael Kessler and Mufit Akinc “WP-1580: Environmentally Benign Repair of Composites Using High Temperature Cyanate Ester Nanocomposites” SERDP & ESTCP Joint Annual Winter In-Progress Review, Weapons Systems and Platforms, February 13, 2008. Washington, D.C. Invited.
  16. Michael R. Kessler, Mufit Akinc, Xia Sheng, Katherine Lawler, and Wilber Lio, “Toxicity of Cyanate Ester/Nanocomposite Resins for Composite Repair” White paper for the Strategic Environmental Research and Development Program (SERDP), April 2008, 1-18. Invited. (pdf)
  17. Michael R. Kessler, Wilber Lio, Xia Sheng, Mufit Akinc “High Temperature Cyanate Ester Adhesives Reinforced with Functionalized Nanoalumina” Proceedings of the SAMPE 2008 Fall Technical Conference, September 8-11, 2008, Memphis, TN. CD-ROM. Pages: 13.
  18. M. R. Kessler, M. Akinc, X. Sheng, Wilber Lio, Katherine Lawler “Environmentally Benign Repair of Composites Using High Temperature Cyanate Ester Nanocomposites: Nanofluid Processing and Characterization” The Partners in Environmental Technology Technical Symposium and Workshop (Sponsored by SERDP and ESTCP), December 2-4, 2008, Washington D.C. Poster Presentation.
  19. Michael Kessler, Mufit Akinc “High Temperature Resin Injection Repair for Composites” 9<sup>th</sup> Annual DoD Advanced Composite Maintainers Conference, June 9-11, 2009, Lake Buena Vista, FL,
  20. W. Lio, X. Sheng, K. Lawler, M. Akinc, M. R. Kessler “Effect of alumina nanoparticles on the properties of bisphenol E cyanate ester adhesive resin for composite repair” Proceedings of the 67th Annual Technical Conference for the Society of Plastics Engineers, June 22-24, 2009. Chicago, IL.
  21. M. R. Kessler, M. Akinc, X. Sheng, W. Lio, K. Lawler, M. Thunga, J. Henson “Environmentally Benign Repair of Composites Using High Temperature Cyanate Ester Nanocomposites: Repair System Evaluation” The Partners in Environmental Technology Technical Symposium and Workshop (Sponsored by SERDP and ESTCP), December 1-3, 2009, Washington D.C. Poster Presentation.
  22. Mahendra Thunga, Wilber Lio, Mufit Akinc, M. R. Kessler “Bisphenol E Cyanate Ester as a Novel Resin for Repairing High Temperature Advanced Aircraft Composites” Iowa Academy of Science 122nd Annual Meeting, April 16-17, 2010, Lamoni, IA.